Simulating Protostellar Evolution and Radiative Feedback in the Cluster Environment

Simulating Protostellar Evolution and Radiative Feedback in the Cluster Environment

By

Mikhail Klassen, B.Sc.

A Thesis

Submitted to the School of Graduate Studies

in Partial Fulfilment of the Requirements

for the Degree

Master of Science

McMaster University

©Copyright by Mikhail Klassen, August 2011

MASTER OF SCIENCE (2011) McMaster University

(Physics and Astronomy) Hamilton, Ontario

TITLE: Simulating Protostellar Evolution and Radiative Feedback in the Cluster Environment

AUTHOR: Mikhail Klassen, B.Sc. (Columbia University)

SUPERVISOR: Ralph E. Pudritz

NUMBER OF PAGES: xxi, 140

Abstract

Stars form in clusters amidst complex and coupled physical phenomena. Among the most important of these is radiative feedback, which heats the surrounding gas to suppress the formation of many low-mass stars. In simulations of star formation, pre-main-sequence modeling has often been neglected and stars are assumed to have the radii and luminosities of zero-age main sequence stars. We challenge this approach by developing and integrating a one-zone protostellar evolution model for FLASH and using it to regulate the radiation output of forming stars. The impact of accurate pre-main-sequence models is less ionizing radiation and less heating during the early stages of star formation. For stars modeled in isolation, the effect of protostellar modeling resulted in ultracompact HII regions that formed slower than in the ZAMS case, but also responded to transitions in the star itself. The HII region was seen to collapse and subsequently be rebuilt as the star underwent a swelling of its radius in response to changes in stellar structure and nuclear burning. This is an important effect that has been missed in previous simulations. It implies that observed variations in HII regions may signal changes in the stars themselves, if these variation can be disentangled from other environmental effects seen in the chaotic cluster environment.

Acknowledgements

This project has been two years in the making. During this time, I've received a great deal of assistance from many people that I would like to acknowledge here. I am indebted to my supervisor, Prof. Ralph Pudritz, for steering this project and providing perspective on this work as it fits within the greater context of astrophysics. I've also benefitted from helpful conversations with Prof. James Wadsley and from the committee support of Prof. Christine Wilson.

Much of the work, especially our later work, benefitted from the experience of Thomas Peters at ITA Heidelberg. In our collaboration, Thomas shared with us a very significant piece of code that represented a great deal of his PhD work—a sophisticated parallel raytracing algorithm for FLASH. It would have taken years for us to independently develop anything remotely equivalent. We shared with him our protostellar evolution code, which he helped test. Thomas also suggested a key test that led to important scientific results.

Our protostellar code follows closely a similar code developed by Mark Krumholz. Some technical subtleties not elaborated on in great detail in any published paper could have been significant technical hurdles in the development of our own code. We are very grateful to Mark for his generous, detailed explanations that helped me to overcome these hurdles.

I'm also grateful to Takashi Hosokawa for kindly choosing to share data with us. This allowed us to very easily compare the results from our code to other published results.

For many of the technical challenges, I am indebted to the excellent support staff that work tirelessly in the Physics & Astronomy department at McMaster University and as part of the SHARCNET support staff. In particular, these are: Hua Wu, the department systems administrator; Patrick Emond, visualization specialist; and Sergey Mashchenko, research scientist and SHARCNET support. I have also received continuous assistance from Dennis Duffin, Elizabeth Tasker, and Rory Woods with coding, visualization, and analysis.

And finally, I thank my family and wife for their love and encouragement. Directly, or indirectly, my parents have long encouraged an open and curious mind, and enabled me to pursue this career in science. My thesis is dedicated to them for their longsuffering and unconditional love. My wife, Sheila, has also made this work possible, through her encouragement and support—especially during the months it took to write this thesis. Hold tight, because now comes doctoral work.

Dedicated to my parents, Adolfo and Elly Klassen.

Table of Contents

List of Figures

List of Tables

Chapter 1

Introduction

Stars are the engines that drive much of the physics in the universe. They release the energy bound up in atomic and molecular hydrogen and synthesize almost every heavier element. Stellar life-cycles drive the evolution of galaxies. Stars are also the homes of planetary systems and determine their habitability. In these ways and many others, the study of stars and how they form lie at the center of much of modern astronomy and astrophysics.

The conversion of molecular gas into fully-formed stars is exceptionally complex, involving many diverse processes. These different processes are often linked to each other through feedback mechanisms that make isolating and understanding the contribution of each process a difficult task. Stars also rarely form in isolation, but instead are seen to be forming in clusters within molecular clouds. In the cluster environment, the formation of a sufficiently massive star can affect all the others through the energy it radiates back into cloud. Cold, dense gas is sensitive to small fluctuations in density that can lead to runaway gravitational collapse in a process called fragmentation. The presence of very massive, highly luminous stars can shut off any further star formation by suppressing fragmentation. Massive stars heat their environments, and so raise the threshold density needed for runaway gravitational collapse. This affects the kinds of stars that can form in a cluster. The distribution in birth-masses for stars is represented by the initial mass function (IMF). Different feedback processes in star formation, and radiation in particular, could be affecting the high-mass and low-mass ends of this distribution through the suppresion of fragmentation.

Figure 1.1: The star-forming region N11B inside the Large Magellanic Cloud (LMC), part of the constellation Dorado, as seen by the Hubble Space Telescope. It is located some 160,000 light-years away from us. It is part of the larger region known as N11, which is the second-largest star-forming region in the LMC, surpassed only by 30 Doradus. *Credit: NASA/ESA and the Hubble Heritage Team (AURA/STScI/HEIC).*

Massive stars, through their ultraviolet radiation, also form bubbles of ionized hydrogen within molecular clouds. These bubbles, known as HII regions, can expand to destroy their parent clouds. Observations of these show highly amorphous shapes driven presumably by stellar winds from these massive stars.

Stellar winds create cavities within clouds and famous examples include the Orion Nebula.

An HII region is capable of shutting off star formation by its destructive effects on the surrounding cloud. Detecting them through observations gives us information about the massive stars that created them. The formation of HII regions around massive stars could also spell the end for the molecular cloud as the size of these bubbles continues to grow, driven by radiation pressure and hot ionized gas, until they tear the cloud apart and shut off all further star formation within that cloud.

The complexity of star formation is not limited to just these phenomena. Investigations into the gas dynamics present in molecular clouds have shown the presence of supersonic turbulence. Turbulence is believed responsible for giving the initial mass function its broad characteristic features (Padoan & Nordlund, 2002; Mac Low & Klessen, 2004). It also creates within clouds visual features that are becoming clearer as the resolution of ground-based and space-based observatories improves: molecular clouds show shock waves, sheets, and filaments (Myers, 2009; Arzoumanian et al., 2011). These create concentrations of gas, form the collapsing cores, and set off star formation.

Magnetic field lines have been seen to thread along filaments (Fiege & Pudritz, 2000; Matthews et al., 2002; Goldsmith et al., 2008), which means they can be present where stars form, and by coupling to other physical processes influence the star forming process (Duffin & Pudritz, 2008; Commerçon et al., 2010).

Figure 1.2: This image, captured by the Hubble Space Telescope, depicts the region labeled N90 located in the Small Magellanic Cloud (SMC) The bright blue stars in the center of the cavity are newly-formed stars. These hot young stars have by their intense radiation created the cavity in which they reside, slowly eroding the surrounding surrounding cloud. *Credit: NASA, ESA and the Hubble Heritage Team (STScI/AURA)-ESA/Hubble Collaboration*

Owing to all this complexity, the use of numerical simulations in studying star formation has become as important as theoretical or observational investigations. The many coupled physical processes are usually nonlinear and time-dependent, and so require robust simulations on high-performance supercomputers that attempt to include as much of the relevant physics as possible. These simulations continue to become more sophisticated as technical hurdles are overcome with novel algorithms and increased computing power, and as more of relevant physics is included in simulations.

To understand the early lives of stars, accurate models of their pre-main-sequence evolution are needed. Such models are important when comparing theory to the observations of young stellar clusters (Baraffe et al., 1998), or in estimating the stellar ages in nearby clusters (Hillenbrand et al., 2008). Figure 1.3 shows how pre-main-sequence models can be used to fit observations from nearby star clusters to Herzsprung-Russell diagrams of luminosity versus temperature. The models are used to construct isochrones (lines of equal age) and thereby determine the ages of stars being studied.

The specific focus of this thesis is to accurately compute the evolution of a protostar—a young stellar object that has not yet begun burning hydrogen—and to combine this with a radiative transfer code that will allow us to study radiative feedback during massive star formation. In particular, we wish to compute their luminosity and the character of their radiation. The implementation of protostellar "tracks" allows one to compute the radiative feedback. We must be careful to have our model moderate the intensity of the radiation accurately, appropriate to the current evolutionary stage of the newly-formed

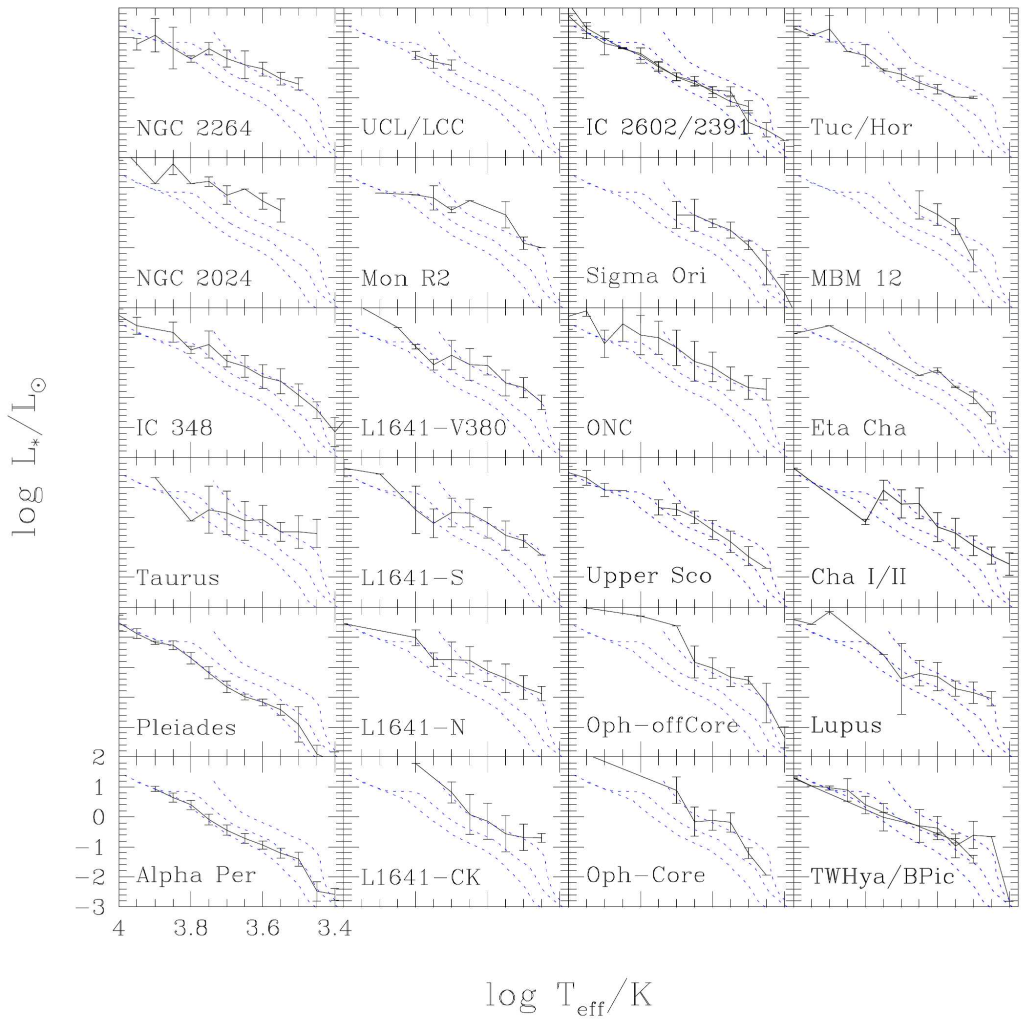

Figure 1.3: From Hillenbrand et al. (2008): Representations of young star cluster luminosity spreads. Median and 1-sigma luminosity as a function of effective temperature, shown for spectral types cooler than A0 (masses $< 3M_{\odot}$). Comparison of the empirical isochrones (solid lines) is made to the 1, 10, and 100 Myr constant age sequences from D'Antona & Mazzitelli (1997, 1998) (dotted lines).

star. As an initial estimate, the stars were assigned the temperature and luminosity of mature hydrogen-burning zero-age main sequence stars. But during the process where the protostar is evolving toward the main sequence, it goes through several evolutionary stages where its radius changes dramatically as new material is accreted onto its surface, and as changes in stellar structure take place beneath the surface. This evolutionary process, in turn, affects the surface temperature and radiative output of these stars. The process of accreting mass also adds its own luminosity to the energy output of young protostars.

We undertook to capture this complex process by following the evolution of a protostar in our simulations. Our approach is based on the one detailed in Offner et al. (2009). This allowed us to scale the radiative feedback of new stars by a self-consistent evolutionary model, rather than by prematurely assigning a stellar radius or luminosity based on values determined for adult stars. We then ran simulations of star formation in a cluster using this new protostellar model, coupled for the first time to a raytracing radiative feedback code. The results of these simulations are written in the form of a paper to be submitted for publication, constituting Chapter 4 of this thesis.

In this thesis, I discuss the use of a novel algorithm for handling radiative feedback in star formation simulations. The technique, called *hybrid-characteristics raytracing*, developed by Rijkhorst et al. (2006) and optimized for multiple sources in a parallel code by Peters et al. (2010a), is discussed in greater detail in Chapter 3. Its strength is in modeling the formation of HII regions from massive stars. The general morphologies of these simulated clouds have been supported by observations (Deharveng et al., 2010). The technique provides a way to model the heating and ionization of the gas surrounding a cluster of newly-formed stars. This effects the population dynamics—the numbers and kinds of stars formed—and their accretion histories, i.e. how quickly stars grow in size.

Chapters 2 and 3 that precede the paper respectively detail the theory and the numerics involved in this work, with Chapter 5 summarizing conclusions. The aim of all this work is to construct a more coherent and accurate picture of the star formation process, allowing for future investigations that include such other important factors as turbulence and magnetic fields. The formation process of massive stars in particular stands to be better understood by such work, as well as their influence on the initial mass function, which speaks to star formation in general everywhere in the galaxy.

Chapter 2

Theory

2.1 Star formation

Giant molecular clouds (GMCs) within galaxies are the observed birthplaces of stars, where the interplay of turbulence and gravity gives way to gas fragmenting into condensates which then collapse to form stars (Mac Low & Klessen, 2004; Zinnecker & Yorke, 2007). These molecular clouds are observed to be highly filamentary (Myers, 2009) and recent Herschel observations strongly confirm the high density gas in filaments as the sites of star formation (Hill et al., 2011; Arzoumanian et al., 2011). Turbulence is thought responsible for these filaments as well as the general morphology and kinematics of molecular clouds, and likely the broad features of the IMF itself (Padoan & Nordlund, 2002).

It's now understood that star formation involves a great deal more physics than initially considered in simple analytic models. Much of the recent progress has come from investigating the effects of turbulence on the star formation process. For a review, see e.g. McKee & Ostriker (2007). Repeated shocking of the gas from supersonic turbulence is a multiplicative process capable of producing a lognormal density PDF (Vázquez-Semadeni et al., 2006; Kevlahan & Pudritz, 2009). Padoan & Nordlund (2002) connect this process to the spectrum of stellar masses, the so-called initial mass function. There is a marked deviation from the lognormal shape at the high-mass end, where the IMF assumes a power-law form (Chabrier, 2003). Moreover, and counter-intuitively, the IMF appears to be universal (Kroupa, 2001, 2002), at least to within current observational limits.

At the scale of star clusters, radiative feedback becomes important, even from low-mass stars (Bate, 2009). Radiative feedback affects the star cluster by raising the gas temperature, thereby raising the Jeans mass, and halting further gas fragmentation (Krumholz et al., 2007a; Bate, 2009; Krumholz et al., 2010). It also affects the cluster through the formation of HII regions (Peters et al., 2010a), which can expand and destroy the cluster (Bally & Scoville, 1980; Matzner, 2002). The O and B stars from a star cluster may also deposit sufficient momentum into the gas via radiation pressure that the entire molecular cloud is destroyed (Harper-Clark & Murray, 2011). Alternatively, momentum-driven shocks may also trigger new star formation in a "collect and collapse" process (Anderson et al., 2010). Other sources of feedback from stars include outflows and outflow-driven turbulence, stellar winds, and supernovae, but these have not been considered for this thesis.

The role played by magnetic fields has long been discussed. Molecular clouds are observed to be highly magnetized, and magnetic fields may shape their overall dynamics and evolution (Heiles et al., 1993; McKee et al., 1993).

Magnetic fields have been proposed as a support mechanism against gravitational collapse (Myers & Goodman, 1988). When coupled with radiation, the combined feedback effects are strengthened, with magnetic fields providing large-scale support of low-density gas and radiation suppressing small-scale fragmentation (Price & Bate, 2009). Magnetic fields play a central role in the origin of protostellar outflows and jets (e.g. the review by Pudritz et al., 2007). Commerçon et al. (2010) showed that magnetic braking of rotating gas accelerates accretion and so amplifying the accretion luminosity.

2.2 Protostars and their evolution

Collapsing protostars have long been modeled using a polytropic equation of state (Larson, 1969),

$$P = K\rho^{1+\frac{1}{n}}, \tag{2.1}$$

in which the pressure P depends on the density ρ, with K a constant and n the polytropic index. Polytropes make for good first approximations to many astrophysical objects. A polytropic index of $n = 3$ is usually used to model main sequence stars, while $n = 1.5$ can describe stars with fully convective cores descending their Hayashi tracks or white dwarfs. An isothermal sphere has a polytropic index of $n = \infty$.

Polytropes are the solutions to the Lane-Emden equation, a non-dimensional form of the hydrostatic equation,

$$\frac{1}{\xi^2}\frac{d}{d\xi}\left(\xi^2\frac{d\theta}{d\xi}\right) + \theta^n = 0 \tag{2.2}$$

where ξ is the dimensionless radius

$$\xi = r\left(\frac{4\pi G\rho_c^2}{(n+1)P_c}\right)^{1/2} \tag{2.3}$$

and θ is given by Equation (2.9).

We arrive at the Lane-Emden equation when we begin with the equation for hydrostatic equilibrium and Poisson's equation for the gravitational potential Θ, and close them with the polytropic equation of state. In spherical coordinates,

$$\frac{1}{\rho}\frac{dP}{dr} = -\frac{d\Phi}{dr} \tag{2.4}$$

$$\nabla^2\Phi = \frac{1}{r^2}\frac{d}{dr}\left(r^2\frac{d\Phi_g}{dr}\right) = 4\pi G\rho \tag{2.5}$$

$$P = K\rho^{1+\frac{1}{n}} \tag{2.6}$$

Substituting (2.6) into (2.4), we get

$$\frac{1}{\rho}\frac{d\rho^{1+\frac{1}{n}}}{dr} = -\frac{d}{dr}\frac{\Phi}{K} \tag{2.7}$$

If we then assume that solutions are of the form $\rho = \rho_c\theta^n$, we may write

$$\frac{1}{\rho_c\theta^n}\frac{d(\rho_c^{1+\frac{1}{n}}\theta^{n+1})}{dr} = \frac{d}{dr}\left(-\frac{\Phi}{K}\right), \tag{2.8}$$

where we have dropped the subscript g from the gravitational potential Φ. Integrating with respect to r, we can express θ as

$$\theta = \frac{-\Phi}{(n+1)K\rho_c^{1/n}} \tag{2.9}$$

or instead write the gravitational potential Φ in terms of the other variables,

$$\Phi = -(n+1)K\rho_c^{1/n}\theta. \tag{2.10}$$

Substituting this expression for Φ into Poission's equation (2.5), we have

$$\frac{1}{r^2}\frac{d}{dr}\left(r^2\frac{d\theta}{dr}\right) = -\frac{4\pi G\rho_c^2}{(n+1)K\rho_c^{1+\frac{1}{n}}}\,\theta^n \tag{2.11}$$

When we express this equation in terms of the dimensionless radius given by Equation (2.3), we arrive at the Lane-Emden equation:

$$\frac{1}{\xi^2}\frac{d}{d\xi}\left(\xi^2\frac{d\theta}{d\xi}\right) + \theta^n = 0 \tag{2.12}$$

This differential equation can be solved analytically only for certain values of n (e.g. Horedt (1986a)). In general, numerical methods must be used, such as a good fourth-order Runge-Kutta solver, integrating outwards from the center of the polytrope. The only constraints we set on the initial conditions are

$$\theta(0) = 1 \tag{2.13}$$

$$\left.\frac{d\theta(\xi)}{d\xi}\right|_{\xi=0} = 0 \tag{2.14}$$

The variable θ can be thought of as a density ratio since $\theta^n = \rho/\rho_c$. We iterate with our solver until the condition that $\theta = 0$, i.e. $\rho = 0$, is satisfied. We define the radius at which this occurs as ξ_1. Our numerical integrations leaves us with a few other useful variables besides ξ_1, which we retain:

$$D_n = \rho_c/\bar{\rho}$$
$$-\xi_1^2 \frac{d\theta}{d\xi}\bigg|_{\xi=\xi_1}$$

We checked our solver's solutions against some of those listed in the tables compiled by Horedt (1986b). Here, $\bar{\rho}$ is the average density of our polytropic sphere.

At other radii, the density, pressure, and temperature are expressed

$$\theta = \theta(\xi) \tag{2.15}$$

$$\rho = \rho_c \theta^n \tag{2.16}$$

$$P = P_c \theta^{n+1} \tag{2.17}$$

$$T = T_c \theta \tag{2.18}$$

If we are going to build a one-dimensional stellar model that will be an accurate first-order approximation to real protostars—a so-called one-zone model—we will need to relate the solutions to the Lane-Emden equation to real variables such stellar mass, radius, and luminosity. What we can expect to know from our simulations is the mass of the stars we are forming, and their accretion rates. From these, we need to solve for radius and luminosity.

We can begin to relate the stellar mass M_* to Lane-Emden equation by the expression

$$M_* = 4\pi \int_0^{r_o} \rho r^2 dr = 4\pi\rho_c \left(\frac{(n+1)P_c}{4\pi G\rho_c^2}\right)^{3/2} \int_0^{\xi_1} \theta^n \xi^2 d\xi \tag{2.19}$$

having only substituted the dimensionless radius. The integral can be solved by substituting in the Lane-Emden equation (2.12) for θ^n. It solves to $-\xi_1^2 \frac{d\theta}{d\xi}\Big|_{\xi=\xi_1}$. So we have

$$M_* = 4\pi\rho_c^{\frac{3-n}{2n}} \left(\frac{(n+1)K}{4\pi G}\right)^{3/2} \left(-\xi^2 \frac{d\theta}{d\xi}\right)\Big|_{\xi=\xi_1} \tag{2.20}$$

We now express the density contrast:

$$\begin{aligned} D_n &\equiv \frac{\rho_c}{\bar{\rho}} \\ &= \rho_c \frac{4\pi R^3}{3M} \\ &= \frac{4\pi}{3}\rho_c \alpha^3 \xi_1^3 \left[-4\pi\alpha^3\rho_c\xi_1^2 \left(\frac{d\theta}{d\xi}\right)_{\xi_1}\right]^{-1} \\ &= -\left[\frac{3}{\xi_1}\left(\frac{d\theta}{d\xi}\right)_{\xi_1}\right]^{-1} \end{aligned} \tag{2.21}$$

This quantity makes the expression of other equantities a little tidier. The equation of state for a polytrope is $P = K\rho^{(n+1)/n}$. We can take the expression for the stellar mass, Equation (2.20), make the substitution

$$R_* = \alpha\,\xi_1 = \left[\frac{(n+1)K}{4\pi G \rho_c^{(n-1)/n}}\right]^{1/2} \xi_1, \tag{2.22}$$

solve for K, and the substitute back into the equation of state. This leaves us with an expression for pressure, which at the center of the star takes the value

$$
\begin{aligned}
P_c &= (4\pi)^{1/3} \left[\frac{3^{(6-2n)/(3n)}}{n+1} \, \xi_1^{-(2n+6)/(3n)} \, \left(\frac{d\theta}{d\xi} \right)_{\xi_1}^{(6-4n)/(3n)} \right] G M^{2/3} \rho_c^{4/3} \\
&= (4\pi)^{1/3} B_n G M^{2/3} \rho_c^{4/3}
\end{aligned}
\tag{2.23}
$$

where we have defined

$$
\alpha = \left[\frac{(n+1)K}{4\pi G \rho_c^{(n-1)/n}} \right]^{1/2} . \tag{2.24}
$$

and

$$
B_n = \frac{3^{(6-2n)/(3n)}}{n+1} \, \xi_1^{-(2n+6)/(3n)} \, \left(\frac{d\theta}{d\xi} \right)_{\xi_1}^{(6-4n)/(3n)} \tag{2.25}
$$

We are left with a succinct expression for the central pressure in Equation (2.23). It will turn out that the function B_n plays an important role in the implementation of stellar evolution that we turn to now.

It would have been very convenient to use Equation (2.20) for the stellar mass to solve for the stellar radius at every time. The trouble is that there are still too many unknowns: the coefficient K and the central density ρ_c. Without other equations to close these variables, this equation does not prove to be terribly useful. We cannot in general arrive at a stellar radius R_* purely from a knowledge of mass M_* and accretion rate $\dot{M}_*$ using only the computed solution to the Lane-Emden equation.

What we *can* do is repeatedly solve the Lane-Emden equations for a set of possible polytropic indices n. For each polytropic index, we can store the specific parameters related to that model—D_n, B_n, ξ_1, etc.—in a table. These are independent of stellar mass. For individual cases, we can then appeal to this precomputed table to solve for the other unknowns. This is the approach that we take, but it does not lead to a solution of the stellar radius. This would have implied that there is a unique radius for each protostar of a given mass, irrespective of environmental factors such as the accretion rate. In reality, the stellar radius depends on the *history* of the protostar: its growth over time, which is sensitive to the mass accretion rate.

One-zone models are built up on considerations of enegy conservation, and *evolve* a stellar radius and stellar luminosity starting from some initial values. Where the solutions to the Lane-Emden equation become immensely useful is in estimating the internal structure of stars, i.e. ratio of internal energies, or alternatively the ratio of gas and radiation pressures.

In the approach employed by Nakano et al. (2000), the zero point of internal energy of the protostar is taken to be the gas of the parental cloud, composed of molecular hydrogen and elemental helium. For a protostar of mass M and radius R, the total energy of a protostar is then expressed by

$$E = -\frac{\beta}{2} a_g \frac{GM^2}{R} + \Psi_I \frac{M}{m_H} - f_D \Psi_D \frac{M}{m_H}. \tag{2.26}$$

β is the ratio of gas pressure to the total pressure (gas + radiation), $\beta = P_{\rm gas}/(P_{\rm gas} + P_{\rm rad})$. Alternatively, it can be expressed in terms of total thermal energy, $\beta = 2U_{\rm gas}/(2U_{\rm gas} + U_{\rm rad})$. a_g is the coefficient for the gravitational binding energy, $a_g = 3/(5-n)$ for polytropes with $n < 5$ (Chandrasekhar, 1939).

The first term on the right side of the equation gives the total gravitational, thermal, and radiant energy. The gravitational binding energy of a polytrope is $U_g = \frac{3}{5-n} GM^2/R$. From the virial theorem, the thermal energy term should be $U_{\rm gas} = -\frac{1}{2}U_g$, but considerations of radiation pressure introduce the factor β which is approximately 1 for all but the most luminous stars, so that

$$U_{\rm gas+rad} = \frac{3}{5-n}\left(\frac{\beta}{2} - 1\right)\frac{GM^2}{R}. \tag{2.27}$$

The second term in Eqn (2.26) is the total energy consumed through the dissociation and ionization of the gas accreted, with m_H the mean molecular weight of hydrogen and Ψ_I the energy per amu—approximately 17eV. The last term on the right-hand side is the energy released by deuterium fusion, with f_D the fraction of deuterium already burned and Ψ_D the energy released by this fusion per amu—approximately 100eV. Nakano et al. (2000) neglect magnetic and rotational energies. Observed young stellar objects (YSOs), they claim, are seen to be rotating at a rate far slowed than their breakup velocity.

Conservation of energy demands that

$$\frac{dE}{dt} = -L - \frac{GM\dot{M}}{R}(1 - f_k) \tag{2.28}$$

where f_k is the ratio of the kinetic energy per unit mass to the depth of the gravitational potential at the protostellar surface. Alternatively, it can be defined (Offner et al., 2009) as “the fraction of the kinetic energy of the infalling material that is radiated away in the inner accretion disk before it reaches the stellar surface.”

Assuming constant accretion, $M = \dot{M}t$, and equations (2.26) and (2.28), Nakano et al. (2000) derive the change in the protostellar radius:

$$\frac{d\log R}{d\log M} = 2 - \frac{2}{a_g\beta}(1 - f_k) + \frac{d\log\beta}{d\log M} - \frac{2R}{a_g\beta G M \dot{M}}(L + L_I - L_D), \quad (2.29)$$

where

$$L_I = \frac{d}{dt}\left(\Psi_I \frac{M}{m_H}\right) = \Psi_I \frac{\dot{M}}{m_H} \approx 2.5 \times 10^3 \, L_\odot \frac{\dot{M}}{10^{-2} M_\odot \mathrm{yr}^{-1}}, \quad (2.30)$$

$$L_D = \frac{d}{dt}\left(f_D \, \Psi_D \frac{M}{m_H}\right) \quad (2.31)$$

Equation (2.29) was discretized in Offner et al. (2009) in building their one-zone model—the same model we're employing. This model we built into the FLASH astrophysics code and paired with a radiative feedback code. It is described in detail in Chapter 3. This is the first time that a pre-main-sequence model has been paired with a raytracing-based radiative feedback code, and it has allowed us to study questions of HII region formation and ionizing feedback.

Deuterium burning is a tricky thing to keep track of in an evolving protostar. A threshold core temperature for fusion is necessary, so any luminosity that the star may have prior to reaching this threshold temperature comes from Kelvin-Helmholtz contraction and accretion. Deuterium fusion can begin around $T_c \approx 1.5 \times 10^6$K and as long as there is any deuterium left, core burning acts as a thermostat keeping the temperature at 1.5×10^6 K. Following

Chandrasekhar (1939), Nakano et al. (2000) describe the central temperature for a polytropic star by

$$T_c = \beta_c a_T \frac{\mu m_H}{k} \frac{GM}{R}, \tag{2.32}$$

where μ is the mean molecular weight, β_c is the ratio of gas pressure to total pressure at the center of the polytrope, and a_T is a coefficient of order unity whose values can be found in Chandrasekhar (1939) for various polytropes. Assuming that $dT_c/dM = 0$, differentiating (2.32) with respect to mass M and substituting Equation (2.29) for $d \log R / d \log M$, we find the deuterium luminosity to be

$$L_D = L + L_I + \frac{GM\dot{M}}{R} \left\{ 1 - f_k - \frac{a_g \beta}{2} \left[1 + \frac{d \log(\beta/\beta_c)}{d \log M} \right] \right\}. \tag{2.33}$$

The discretized version of this equation can be found in Chapter 3. Once initial deuterium supplies are exhausted, core burning depends on the accretion of new fuel and the luminosity is assumed to be

$$L_D = \Psi_D \frac{\dot{M}}{m_H} \approx 1.5 \times 10^4 \ L_\odot \ \frac{\dot{M}}{10^{-2} M_\odot \mathrm{yr}^{-1}}, \tag{2.34}$$

assuming an abundance for deuterium of $D/H = 2.5 \times 10^{-5}$. At this stage the core temperature is no longer constant.

The intrinsic stellar luminosity is not as complex a quantity as the radius. Hayashi (1961) showed that no stable stellar configurations exist below a threshold effective temperature T_H. Hence, the luminosity can be described by

$$L_H = 4\pi R^2 \sigma T_H^4, \tag{2.35}$$

where σ is the Stefan-Boltzmann constant. We take $T_H = 3000$ K in agreement with Nakano et al. (2000) and Offner et al. (2009). Stars hotter than the Hayashi limit have their luminosities well described by main-sequence equivalent stars. For this reason Offner et al. (2009) set the intrinsic luminosity as

$$L_{\rm int} = \max(L_H, L_{\rm ms}) \tag{2.36}$$

Fitting formulas for the luminosities of main sequence stars exist (Tout et al., 1996) and we describe these in Chapter 3.

With expressions now for luminosity and the rate of change of stellar radius, we need to initialize these values. Palla & Stahler (1991, 1992) solve the equations of stellar structure for intermediate mass stars and consider how stars evolve as they burn up their deuterium reserves, as their stellar structure changes, and as they accrete new material at steady rates. This is more sophisticated than what we are doing, which does not involve solving the coupled differential equations of stellar structure, but solving for the 1-D evolution of the entire star under conditions of mass accretion. A one-zone model is intended to be a simplified prescription for the more subtle processes occuring beneath the stellar surface. Offner et al. (2009) used the Palla & Stahler (1991, 1992) results to empirically calibrate their one-zone model and initialize radius and polytropic index as

$$r = 2.5\ R_\odot \left(\frac{\dot{M}}{10^{-5}\ M_\odot\ {\rm yr}^{-1}} \right)^{0.2} \tag{2.37}$$

$$n = 5 - 3 \left[1.475 + 0.07\ \log_{10} \left(\frac{\dot{M}}{M_\odot\ {\rm yr}^{-1}} \right) \right]^{-1} \tag{2.38}$$

The one-zone model is initialized at some low mass (we choose $0.1M_\odot$), and the radius then evolved according to Equation (2.29). The choice of initialization mass is a little arbitrary, but should result in good fits to more detailed stellar structure calculations. We chose $0.1M_\odot$ because it resulted in greater numerical stability in our code (we could run with larger timesteps). Since we are more concerned with massive star formation rather than brown dwarfs, it was not crucial that we initialize at very low mass.

Equation (2.29) necessitates that we calculate a value for β in order to evolve the radius. β is defined as the ratio of gas pressure to total pressure (gas + radiation), or

$$\begin{aligned}
\beta(\xi) = \frac{P_g(\xi)}{P_g(\xi)+P_r(\xi)} &= \frac{\rho(\xi)k_BT(\xi)/\mu H}{\rho(\xi)k_BT(\xi)/\mu H + (1/3)\,aT^4(\xi)} \\
&= \frac{\rho_c\theta^n k_B T_c\theta/\mu H}{\rho_c\theta^n k_B T_c\theta/\mu H + (a/3)T_c^4\theta^4} \\
&= \frac{(\rho_c k_B T_c/\mu H)\,\theta^{n+1}}{(\rho_c k_B T_c/\mu H)\,\theta^{n+1} + (a/3)T_c^4\theta^4} \qquad (2.39)
\end{aligned}$$

For a (gas + radiation) fluid of total pressure P, we can find an implicit expression for β:

$$P = P_g + P_r = \rho kT/\mu m_H + 1/3aT^4$$

$$\beta = P_g/(P_g + P_r) = P_G/P$$

$$P_g = \beta P \qquad\qquad P_r = (1-\beta)P$$

$$
\begin{aligned}
P_r = \tfrac{1}{3}aT^4 &= \tfrac{1}{3}a\left(\frac{\mu m_H}{\rho k}\beta P\right)^4 \\
&= \frac{a\mu^4 m_H^4}{3k^4}\frac{P^4}{\rho^4}\beta^4 = (1-\beta)P
\end{aligned}
$$

Hence,

$$
\frac{a\mu^4 m_H^4}{3k^4}\frac{P^3}{\rho^4}\beta^4 + \beta - 1 = 0 \tag{2.40}
$$

The ratio P^3/ρ^4 can be expressed

$$
\begin{aligned}
\frac{P^3}{\rho^4} &= \frac{P_c^3}{\rho_c^4}\theta^{(3n+3)/4n} \\
&= 4\pi B_n^3 M^2 \theta^{(3n+3)/4n}
\end{aligned} \tag{2.41}
$$

We then substitute this back into Equation (2.40),

$$
\frac{a\mu^4 m_H^4}{3k^4}\left(4\pi B_n^3 M^2 \theta^{(3n+3)/4n}\right)\beta^4 + \beta - 1 = 0 \tag{2.42}
$$

If we have already computed a table of values for B_n (see Equation (2.25)) for stars of different polytropic index and mass, then the value of β can be solved for numerically.

Integrating the Lane-Emden equation again, this time solving for β at every radius ξ, we solve for the volume-averaged β:

$$
\begin{aligned}
\bar{\beta} &= \frac{1}{V}\int_0^{\xi_1} 4\pi\xi^2\beta(\xi)d\xi \\
&= \frac{3}{\xi_1^3}\int_0^{\xi_1} \beta(\xi)\xi^2 d\xi
\end{aligned} \tag{2.43}
$$

where $V = \frac{4}{3}\pi\xi_1^3$ is the volume of the star in dimensionless coordinates.

Knowing now how to solve for the volume-averaged β in a given polytropic star, we create a second table where we solve for β repeatedly in stars of different masses and polytropic index. In this table we also store the derivatives $d\log\beta/d\log M$ and $d\log(\beta/\beta_c)/d\log M$.

With these two precomputed tables and the one-zone model in hand, we have almost everything that we need. What remains is a discussion of how to configure the one-zone model to respond to important changes that occur in the star. Palla & Stahler (1991, 1992) and others have commented on the stage in the life of a protostar where deuterium burning has ceased in the core due to fuel exhaustion, but then begins in a shell. The formation of a radiative structure and the shell deuterium burning cause the radius of the star to swell very quickly. A one-zone model must be calibrated to the stellar structure calculations and the radius artificially increased when the conditions are right. To do this we must track the amount of deuterium and burn it up at a rate in accordance with the deuterium luminosity (Equation (2.33)). Once it is gone, any new deuterium to arrive via accretion is burned and its luminosity given by Equation (2.34). The swelling of the radius in a one-zone model needs to be calibrated, but one way (Offner et al., 2009) is to check the ratio of L_D to $L_{\rm ms}$. When L_D exceeds some threshold value (Offner et al. (2009) chose $L_D > 0.33L_{\rm ms}$), the radius is multiplied by a constant factor and the evolution continues until the final stage: arrival at the main sequence. The last artificial adjustment made to our one-zone model occurs when the radius has contracted to that of a zero-age main sequence star. The protostellar evolution is complete and the star's radius and luminosity are henceforth described by their ZAMS values.

In summary, one-zone models are attempts to fit 1-D models of the evolution of a star's radius and luminosity to more sophisticated stellar structure codes that take into account the more detailed physics of what happens beneath the surface of a star. Stellar structure codes have become very advanced. There exist now codes that handle the full 3-D structure of a star, its surface, and the accretion happening onto the surface of a forming star. They treat convection, radiation, and nuclear burning. A one-zone model tries to capture all the essential physics with a prescription for the radius and luminosity that matches the stellar structure results as closely as possible.

Hosokawa & Omukai (2009) did such simulations of stellar structure and have their own matching one-zone model. In this thesis, we have at times compared our fits to Hosokawa & Omukai (2009), but we have not calibrated our model to theirs. Future work will involve the retuning of our model to their stellar structure calculations. Offner et al. (2009) believed that the Hosokawa & Omukai (2009) results represented the most accurate work to date on these models.

2.3 The role of radiative feedback

2.3.1 Radiative transfer

In one dimension, the specific intensity or brightness of a ray of light I_ν at a particular frequency ν can be expressed

$$\frac{dI_\nu}{ds} = -\alpha_\nu I_\nu + j_\nu \tag{2.44}$$

where ds is a differential unit of ray length, α_ν is the absorption coefficient and has units of inverse length, and j_ν is the emission coefficient. The first term on the right-hand side of the equation respresents the intensity removed from the ray through absorption by the local medium, and the second term, which has units of energy per unit length per unit time per unit frequency, represents intensity added to the ray by emission from the local medium. We have expressed the radiative transfer equation in one dimension and ignored such things as scattering of rays into the beam, stimulated emission, etc.

In the case where there is emission only, the ray intensity, after some distance Δs becomes

$$I_\nu(s) = I_\nu(s_0) + \int_{s_0}^{s} j_\nu(s')ds'. \tag{2.45}$$

If there is absorption, but no new emission, the ray intensity becomes

$$I_\nu(s) = I_\nu(s_0) \exp\left[-\int_{s_0}^{s} \alpha_n(s')ds'\right]. \tag{2.46}$$

The optical depth of the gas is defined

$$\tau_\nu(s) = \int_{s_0}^{s} \alpha_\nu(s')ds'. \tag{2.47}$$

Gas is said to be *optically thick* or opaque if, along a typical ray through the medium, $\tau_\nu \gg 1$. Conversely, it is said to be *optically thin* or transparanet if $\tau_\nu \ll 1$. An optical depth of $\tau_\nu = 1$ corresponds to be the distance a typical photon of frequency ν can be travel before being absorbed, i.e. the mean free path of radiation at frequency ν.

In star formation, the gas in a region undergoing gravitational collapse is often optically thick. A star emitting radiation into this medium is having much of this starlight absorbed. The energy being absorbed heats the gas and is reemitted at lower frequency. The mixture of hydrogen gas and dust grains, out of which stars are born, has different opacities for different frequencies. The opacity is related to the absorptivity by the equation

$$\alpha_\nu = \rho\kappa_\nu, \tag{2.48}$$

where ρ is the mass density of the local medium and κ_ν has units of length squared per unit mass.

The frequency dependence of the opacity κ complicates treatments of radiative transfer. A "grey atmosphere" approximation is often used, where the frequency dependence is removed by using instead a frequency-averaged opacity. When the Planck function B_ν is used as the weighting function, it is called the Planck mean opacity:

$$\kappa_P = \frac{\int_0^\infty \kappa_\nu B_\nu(T)\, d\nu}{\int_0^\infty B_\nu(T)\, d\nu}, \tag{2.49}$$

where κ_ν is the frequency-dependent opacity, with contributions from dust, electron scattering, and free-free transitions.

Many schemes incorporating radiative transfer into numerical simulations employ this frequency-averaged opacity when computing the absorption of energy by gas (Krumholz et al., 2007a; Bate, 2009; Offner et al., 2009; Peters et al., 2010a). This approach tends to overestimate absorption at infrared frequencies, where the gas is more transparent to radiation, and underestimate absorption at UV frequencies, where in fact ionization of hydrogen gas can occur. Overcoming the technical and computational challenges associated with implementing a multi-frequency radiative transfer method into a star formation simulation is the topic of some current research (Whalen & Norman, 2008; Kuiper et al., 2010).

In the frequency-averaged, or "grey atmosphere" approximation, radiative transfer is primarily implemented in either the flux-limited diffusion approximation or using a raytracing scheme with a single opacity as defined above. Our particular implementation is described in Chapter 3.

2.3.2 Heating, Ionization, and Protostellar evolution

The reason that radiative feedback is important to star formation is related to the Jean's length

$$\lambda_J = \sqrt{\frac{\pi c_s^2}{G\rho}} \propto \left(\frac{T}{\rho}\right)^{1/2}, \tag{2.50}$$

where c_s is the sound speed. The Jeans length gives the critical size scale for a sphere to hydrostatically support itself against gravitational collapse. When gas is heated by radiation, the Jeans length increases so that perturbations in local gas density do not as easily trigger gravitational collapse. As has been shown by many simulations (Krumholz et al., 2007a; Offner et al., 2009; Price & Bate, 2009; Peters et al., 2010a), radiative feedback suppresses the fragmentation of the gas into many low-mass cores. This result has huge implications for initial mass function, for massive stars, and cluster evolution.

Despite a grey atmosphere approximation, it is still possible to estimate ionization rates by separately treating the component of the radiation field whose photons will have energies exceeding the hydrogen threshold for ionization. From Osterbrock (1989), the rate of photoionization is given by

$$A_p = \int_{\nu_0}^{\infty} \frac{4\pi j_\nu}{h\nu} a_0 \, d\nu \tag{2.51}$$

where j_ν is the local mean intensity of the radiation field. $a_0 = 6.3 \times 10^{-18}$ cm^2 is the cross-section for ionization in the frequency-independent grey atmosphere approximation and ν_0 is the threshold frequency for ionization.

Ionized gas can be seen using observations of radio continuum emission, or through observations of recombination lines. Regions of ionized gas known as

HII regions have been observed for a long time (Mezger & Henderson, 1967). Ultracompact HII regions are observed around massive stars of spectral classes O and B (Wood & Churchwell, 1989).

Some radiative feedback codes, such as the one we have implemented for our simulations and described in Chapter 3, can model the ionization of hydrogen gas by stellar sources, allowing for comparison with observations and the ability to study the impact of heating and ionization on the star-forming cluster environment. Any successful model of radiative feedback will need to model its sources correctly. Stars are not born on the main sequence, but begin their lives as gravitationally bound cores accreting material. The luminosities and effective temperatures of these protostars will differ from stars on the main sequence. For this reason, a protostellar model such as the one we describe in Sections 2.2 and 3.3 is necessary as a way of setting and controlling the intensity of the radiation field. How we implement both the protostellar model and radiative feedback in our astrophysics code is the subject of Chapter 3.

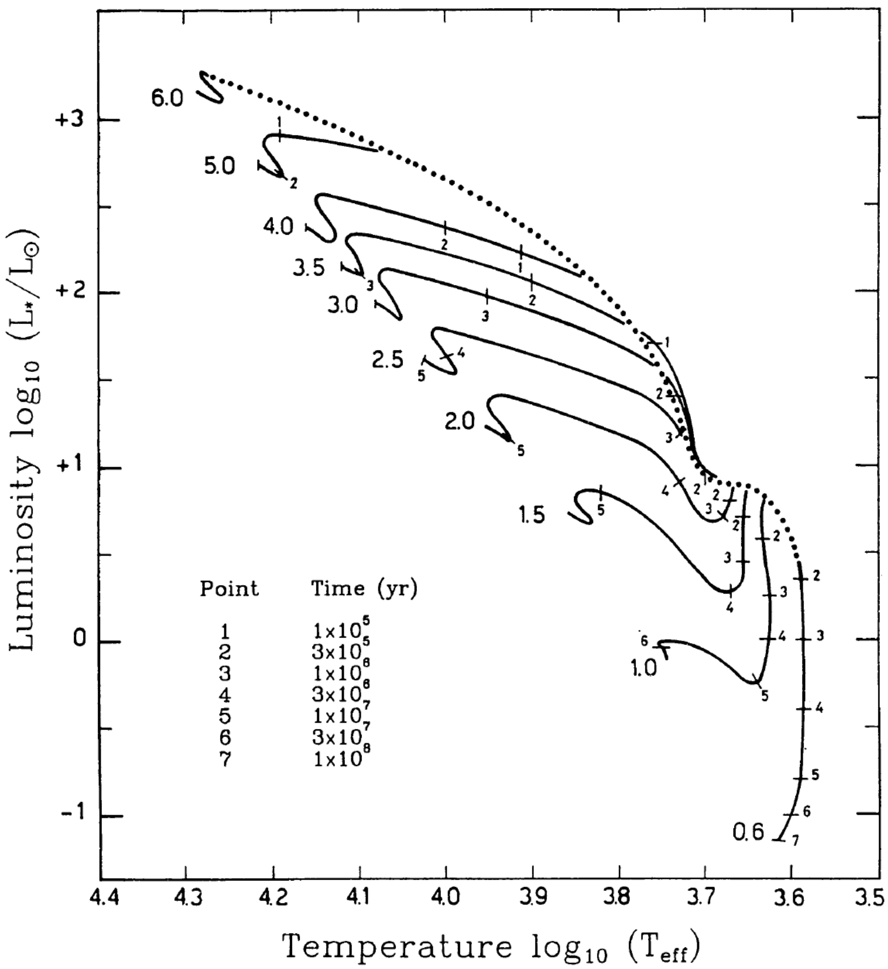

Figure 2.1: Pre-main-sequence evolutionar tracks as computed by Palla & Stahler (1993), shown as an H-R diagram. Also includes tracks for $M_* = 0.6M_\odot$ and $M_* = 1.0M_\odot$ from Parigi (1992). Tracks have their masses labeled. Each star begins its life at the birthline (dotted), where deuterium burning is initiated, then evolving toward and eventually reaching a spot on the main sequence.

Chapter 3

Numerics

3.1 The FLASH code

FLASH (Fryxell et al., 2000; Dubey et al., 2008) is a modular, adaptive, grid-based physics simulation framework. It is designed to handle compressible fluid dynamics, solving the hydrodynamics equations on an adaptive Eulerian mesh running in parallel across many processors (Olson et al., 1999). The principle of adaptive mesh refinement, or AMR, (Berger & Colella, 1989) is to selectively increase the resolution in regions of the grid where it is needed, but retain low resolution where the dynamics at play do not call for further enhancement, thus making huge gains in both memory efficiency and computational speed.

FLASH has been used for a wide range of astrophysics simulations, including the modelling of collapse and accretion within molecular clouds (Federrath et al., 2010), the formation of star clusters (Pudritz, 2004; Peters et al., 2010a), jets and outflows (Banerjee & Pudritz, 2006, 2007; Zanni et al., 2007), protostellar disks (Banerjee et al., 2004), turbulence (Federrath et al., 2010;

Girichidis et al., 2011), supernova explosions (Dubey et al., 2008), ambipolar diffusion in the magnetized gas around a forming star (Duffin & Pudritz, 2008), AGN feedback (Gaspari et al., 2011), and even the evolution of galaxy clusters (Ricker et al., 2001). The code has been rigorously tested against laboratory experiments (Calder et al., 2002), and against other codes (Dimonte et al., 2004; Heitmann et al., 2005; Agertz et al., 2007; Tasker et al., 2008; Kitsionas et al., 2009).

We use FLASH in its version 2.5, making use of its hydrodynamic and gravity solvers solvers, molecular and dust heating and cooling, and additional modifications to include a radiative transfer code and Lagrangian sink particles as developed and tested by Dr. Pudritz's research group and collaborators at McMaster University and Universität Heidelberg. We run simulations on the parallel supercomputers of the SHARCNET consortium.

3.2 Sink particles

In simulations designed to treat the runaway collapse of dense regions of self-gravitating gas in a molecular cloud, we run into a fundamental numerical problem. We want to follow the collapse of each of these regions, which promise to form stars, yet also follow the global evolution of the molecular cloud and star cluster. The mesh can be continuously refined so as to spatially resolve collapsing regions in order to satisfy the Truelove criterion (Truelove et al., 1997). This states that in order to avoid spurious numerical fragmentation resulting from the discretization of the grid, the Jeans length $\lambda_J = \sqrt{15 k_B T / (4\pi G \mu \rho)}$ must be resolved by at least 4 grid cells, where k_B is the Boltzmann constant,

μ is the mean molecular weight, and ρ is the gas density. If the gas is collapsing to ever higher density, an AMR code will reach some limit set either by memory constraints or a maximal refinement cap. In practice, the Jeans length must be resolved by at least 4 cells to avoid artificial fragmentation (Truelove et al., 1997).

There is another major problem with following collapse in an AMR code, which is that the dynamical time—or freefall time $t_{\rm ff} = \sqrt{3\pi/(32G\rho)}$—decreases with increasing density ρ, which requires that the simulation timestep size be shortened if the gas density increases as it does in a collapsing region. The implication is that following a collapse can grind a simulation to a halt. In a cluster simulation, with potentially many stars, the formation of the first star could be a showstopper for the entire simulation.

To remedy this dire computational situation, sink particles were invented (Bate et al., 1995). These particles are introduced into a gasdynamical simulation wherever it is concluded that a star is forming and they effectively cut out the high-density gas. Sink particles are fully Lagrangian, meaning that they move independently of the grid. They were initially used in smoothed-particle hydrodynamics simulations by Bate et al. (1995), then later introduced into Eulerian grid codes by Krumholz et al. (2004). Our sink particles are based on Federrath et al. (2010), which include a rigorous set of creation criteria so that spurious sink particles are not generated by transient overdensities (e.g. in a shock wave).

The set of sink particle creation criteria are summarized in Federrath et al. (2011) and are reiterated here:

For successful sink creation the gas exceeding the density threshold must also

1. be converging (along each cardinal direction individually),
2. have a central gravitational potential minimum,
3. be Jeans-unstable (including magnetic pressure),
4. be bound (including magnetic energy),
5. be on the highest level of the AMR (i.e., Jeans length resolved),
6. not be within accretion radius of existing sinks (then accretion checks apply).

We use the Federrath et al. (2010) sink particles in our simulations, with a few modifications. Our sink particles have had additional properties added to them to properly incorporate to a protostellar evolution code we wrote for FLASH. These additional properties are recorded for each sink particle present in our simulation and they are:

1. protostellar stage (0-6, with 6 corresponding to a main sequence star)
2. intrinsic luminosity
3. polytropic index
4. mass of gas from which deuterium has yet to be fully burned
5. protostellar radius, also used as the accretion radius

3.3 Protostellar evolution

The FLASH code is designed to handle fluids (gas) and particles separately. Particles in FLASH can be very simple—for example, serving as tracers in the gas, not interacting with the gas at all—to arbitrarily sophisticated objects. In writing the protostellar evolution module for FLASH, one needs to give particles a number of additional properties to track. Given the description of the code in Appendix B of Offner et al. (2009), sink particles would need to have at least the following properties added: intrinsic (stellar) luminosity, stellar radius, polytropic index, unburned deuterium mass, and evolutionary stage. These were added to a list of sink particle properties that already included mass, accretion rate, etc.

In the FLASH main driver, we add a stellar evolution step so that FLASH updates (in order):

1. Hydrodynamics (gas)
2. Radiation field
3. Particle locations
4. Sink particle creation/accretion/merging
5. Stellar evolution
6. Gravity

with some minor steps left out for clarity. When evolving the state of each of star, our code proceeds in the following order:

1. Communicate particle information between all processors
2. Initialize any particles now over threshold mass ($0.1 M_\odot$)
3. Update particle radius
4. Update particle luminosity
5. Update stellar evolutionary stage

6. Store all particle data and communicate between all processors

Our code differs from the one described in Offner et al. (2009) in few respects. We choose to initialize our stellar evolution code only after stars reach a mass of $0.1M_\odot$ (instead of their $0.01M_\odot$) because we found that this added to the numerical stability, but otherwise didn't adversely affect our code. For larger accretion rates or timesteps, initializing at very small masses such as $0.01M_\odot$ sometimes resulted in Δr that was larger than the current radius of the star itself. If $\Delta r/\Delta t$ was negative, a negative radius could result if the timestep was large enough. We would have had to enforce a smaller timestep for stability, or used other numerical tricks to get around this problem. Initializing at $0.1M_\odot$ instead of $0.01M_\odot$ (a choice also made by Hosokawa & Omukai (2009)) got around this problem. This also means that our code is unsuitable for studying brown dwarfs or very low mass stars.

Protostars are modeled as accreting polytropes with polytropic indices between 1.5 and 3.0 following Palla & Stahler (1991, 1992), which correspond to fully convective and radiative stellar structures respectively. The polytropic index of the star also changes throughout the simulation, adjusting with the evolving star.

The radius, polytropic index, and unburned deuterium mass are initialized as

$$r = 2.5\ R_\odot \left(\frac{\Delta m / \Delta t}{10^{-5}\ M_\odot\ \mathrm{yr}^{-1}} \right)^{0.2} \tag{3.1}$$

$$n = 5 - 3 \left[1.475 + 0.07\ \log_{10} \left(\frac{\Delta m / \Delta t}{M_\odot\ \mathrm{yr}^{-1}} \right) \right]^{-1} \tag{3.2}$$

$$m_d = m \tag{3.3}$$

where Δm is the mass accreted by the sink particle during a time Δt, and m_d is the unburned deuterium mass. These are fitting formulas calibrated to Palla & Stahler (1991, 1992). If the initial polytropic index n is outside the bounds of $n = 1.5$ or $n = 3.0$, it is capped at the appropriate extreme after intialization. The "unburned deuterium mass" m_d actually represents a mass of molecular gas from which deuterium has not yet been burned. Hence, it is set equal to the initial mass of the particle. This quantity is tracked and used as a flag for switching the evolutionary state of the particle.

The radius is updated via the equation

$$\begin{aligned} \Delta r = {} & 2\, \frac{\Delta m}{m} \left(1 - \frac{1 - f_k}{a_g} + \frac{1}{2} \frac{d \log \beta}{d \log m} \right) r \\ & - 2\, \frac{\Delta t}{a_g \beta} \left(\frac{r}{G m^2} \right) (L_{\mathrm{int}} + L_I - L_D)\, r \end{aligned} \tag{3.4}$$

which represents a discretized version of equation (8) in Nakano et al. (2000).

Here, a_g is the coefficient for the gravitational binding energy and is given by $a_g = 3/(5-n)$. f_k is the fraction of the kinetic energy of accreting material that is converted to radiation. Offner et al. (2009) select $f_k = 0.5$, which is the standard for an α-disk, β describes the ratio of gas pressure to total pressure (radiation + hydrostatic), $L_{\rm int}$ is the *intrinsic* or stellar luminosity, L_I is the "ionization luminosity" and describes the energy required to dissociate and ionize infalling molecular gas, and L_D is the energy from deuterium burning. The signs of these terms in (3.4) come from the fact that $L_{\rm int}$ and $L_{\rm I}$ represent energy losses from the total energy budget of the star, by radiation from the surface and consumed to dissociate and ionize material, respectively. L_D adds to the energy budget through deuterium fusion.

The derivation for the contraction of the star given in Nakano et al. (2000) is based on energy conservation, and in the equation above, the first term on the right-hand side of the equation captures the combined gravitational, thermal, and some of the radiation effects, while the second term captures radiative losses due to stellar luminosity, energy required to ionize incoming molecular gas (L_I), and energy supplied from the burning of deuterium (L_D).

The protostellar model for the sink particles in our simulation describes six distinct evolutionary stages summarized in Table 3.1. An accompanying schematic outlining the stages is shown in Figure 3.1.

The way that various quantities are computed sometimes depends on the evolutionary stage of the particle.

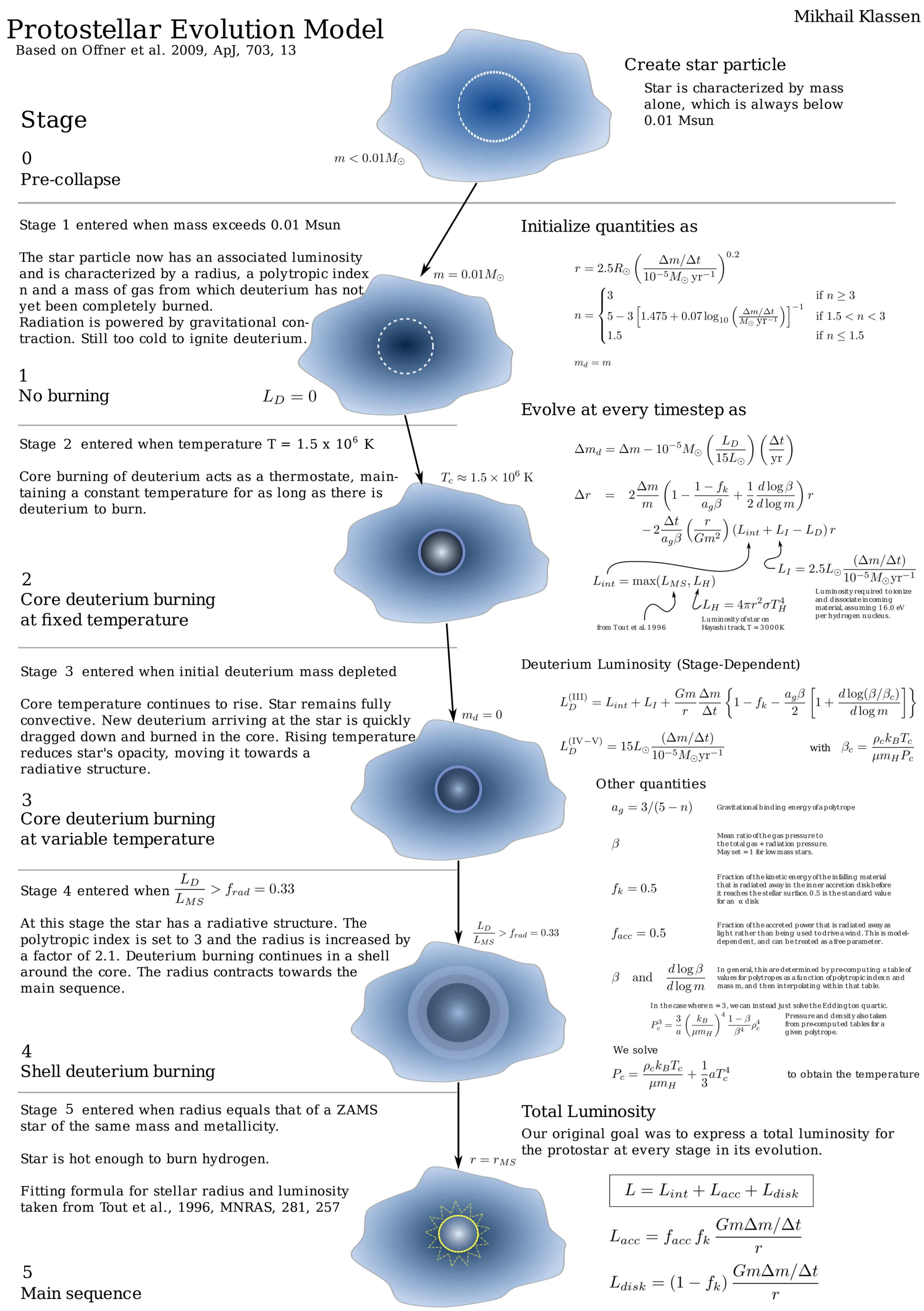

Figure 3.1: Schematic representation of the protostellar evolution model used in Offner et al. (2009) from which we adapted our code. They initialize their protostellar evolution at $0.01 M_\odot$. This schematic was designed during our early phases of code development as a guide.

Table 3.1: Description of the stellar evolutionary stages in the protostellar module

	Stage	Features
0	Pre-Collapse	Mass $m \lesssim 0.1\,M_\odot$ Cannot dissociate H_2 and cause second collapse to stellar densities.
1	No Burning	Object has collapsed to stellar densities. T_c still too cold to burn D. $T_c \lesssim 1.5 \times 10^6$ K Radiation comes purely from gravitational contraction. Star is imperfectly convective.
2	Core D burning at fixed T_c	Temperature reaches required $T_c \sim 10^6$ K to burn D. D burning acts as a thermostat keeping temperature constant. Star is fully convective.
3	Core D burning at variable T_c	D is exhausted. Core temperature now rising again. Star remains fully convective. Accreted D dragged down to core and burned. Rising core temperature reduces opacity. Convection in the stellar core eventually shuts down.
4	Shell D burning	Star core changes to a radiative structure. D burns in a shell around the core. Radius swells.
5	Main Sequence	Star has contracted enough for T_c to reach $\sim 10^7$ K Hydrogen ignites and star stabilizes onto the main sequence.

3.3.1 Calculating stellar luminosity

The intrinsic, or stellar, luminosity $L_{\rm int}$ is taken to be

$$L_{\rm int} = \max(L_{\rm ms}, L_{\rm H}), \tag{3.5}$$

i.e. either the luminosity of a main sequence star of equivalent mass, or the luminosity of a star on the Hayashi track (Hayashi, 1961, 1966), whichever is larger. The main sequence equivalent luminosity is computed using a fitting formula calculated by Tout et al. (1996). Their method of fitting involved the results of a modern version of the stellar evolution code of Eggleton (1971, 1972, 1973) described by Pols et al. (1995). The code was used to calculate the luminosity and radius of ZAMS stars. These were then fit using rational polynomials with a method following Eggleton et al. (1989). Initially, this was done for stars of solar metallicity $Z = 0.02$ and then extrapolated for other metallicities. They found their fitting functions to have errors generally less than 7.5% in luminosity and less than 5% for radius. In the case of solar metallicity, these errors were 3% and 1.2% respectively. The luminosity function is described below and the radius function in Section 3.3.6.

We take all our stars to be of solar metallicity:

$$L = \frac{\alpha M^{5.5} + \beta M^{11}}{\gamma + M^3 + \delta M^5 + \epsilon M^7 + \zeta M^8 + \eta M^{9.5}} \tag{3.6}$$

where the coefficients used for this equation were:

$$
\begin{aligned}
\alpha &= 0.39704170 & \epsilon &= 5.56357900 \\
\beta &= 8.52762600 & \zeta &= 0.78866060 \\
\gamma &= 0.00025546 & \eta &= 0.00586685 \\
\delta &= 5.43288900 & &
\end{aligned}
$$

The Hayashi luminosity is given by

$$L_{\mathrm{H}} = 4\pi\sigma r^2 T_{\mathrm{H}}^4 \tag{3.7}$$

with a surface temperature of $T_{\mathrm{H}} = 3000\mathrm{K}$.

3.3.2 Calculating the ionization luminosity

The energy consumption rate for the dissociation and ionization of infalling molecular hydrogen, assuming it takes 16.0 eV to ionize a hydrogen nuclear, is given by Offner et al. (2009) as

$$L_I = 2.5\,L_\odot \frac{\Delta m/\Delta t}{10^{-5}\,M_\odot\,\mathrm{yr}^{-1}} \tag{3.8}$$

3.3.3 Calculating the deuterium luminosity and deuterium mass

The energy production rate from the fusion of deuterium is stage-dependent. In Stage 0 or Stage 1, the "pre-collapse" and "no-burning" stages, the deuterium luminosity is zero. In Stage 2, the temperature of the core remains at a constant $T_c = 1.5 \times 10^6$ K. The deuterium luminosity during this stage is:

$$L_D = L_{\mathrm{int}} + L_I + \frac{Gm}{r}\frac{\Delta m}{\Delta t}\left\{1 - f_k - \frac{a_g\beta}{2}\left[1 + \frac{d\log(\beta/\beta_c)}{d\log m}\right]\right\}, \tag{3.9}$$

which is derived in Nakano et al. (2000). The quantity $\beta_c = \rho_c k_B T_c/(\mu m_H P_c)$ represents in the ratio of gas pressure to total pressure (gas + radiation) at the center of the polytrope. Deuterium fusion occurs at lower temperatures relative to hydrogen fusion. The unburned deuterium mass m_d is updated

$$\Delta m_d = \Delta m - 10^{-5} M_\odot \left(\frac{L_D}{15 L_\odot}\right)\left(\frac{\Delta t}{\mathrm{yr}}\right) \tag{3.10}$$

Once the star has burned all its initial deuterium, the core temperature of the protostar begins to rise. New deuterium arriving with the infalling material is dragged down and mixed by convection. It is burned as soon as it arrives in the core. The deuterium luminosity in this and all subsequent stages is

$$L_D = 15\, L_\odot \, \frac{\Delta m/\Delta t}{10^{-5} M_\odot/\mathrm{yr}^{-1}} \tag{3.11}$$

which is estimated by assuming that the D/H ratio is approximately 2.5×10^{-5} and the energy released from deuterium fusion is 100 eV per gram. This corresponds to Equation (15) in Nakano et al. (2000).

3.3.4 Calculating the total luminosity

The total luminosity of the sink particle is taken in Offner et al. (2009) to be the sum of the intrinsic, accretion, and disk luminosities, i.e. $L = L_{\mathrm{int}} + L_{\mathrm{acc}} + L_{\mathrm{disk}}$. The only one of these that is actually labour-intensive (computationally speaking) is L_{int}, since it depends on all the steps described up until now. The other components take the form of

$$L_{\mathrm{acc}} = f_{\mathrm{acc}} f_{\mathrm{k}} \, \frac{G m \Delta m/\Delta t}{r} \tag{3.12}$$

$$L_{\mathrm{disk}} = (1 - f_k) \, \frac{G m \Delta m/\Delta t}{r} \tag{3.13}$$

in Offner et al. (2009), where $f_k = 0.5$ is as defined earlier—the efficiency with which infalling material converts gravitational potential energy into radiation, and f_{acc} is defined as the fraction of accretion power converted to radiation instead of driving a wind. Offner et al. (2009) take $f_{\mathrm{acc}} = 0.5$.

The values of $L_{\rm acc}$ and $L_{\rm disk}$ can be computed as needed, so we only bother to save $L_{\rm int}$ with the particle data. In fact, rather than distinguishing between accretion onto the stellar surface and accretion onto the disk, and guessing at what the energy conversion efficiencies might be, we have only one expression for the total accretion luminosity,

$$L_{\rm acc} = \frac{Gm\Delta m/\Delta t}{r} \tag{3.14}$$

where r is the radius of the star as computed by our model. The difference between our approach to accretion luminosity and that of Offner et al. (2009) is factor of order unity.

3.3.5 Calculating β, $d\log\beta/d\log m$, and $d\log(\beta/\beta_c)/d\log m$

The value for β and its various derivatives features in a number of important equations needed to evolve the radius and luminosity of stars in our protostellar model. β represents the volume-averaged ratio of the hydrostatic (gas) pressure to the total pressure (gas + radiation) within the star. We model the stars as polytropes. For polytropes of index $n = 3$, the value for β can be obtained by solving the Eddington quartic:

$$P_c^3 = \frac{3}{a}\left(\frac{k_B}{\mu m_H}\right)^4 \frac{1-\beta}{\beta^4}\rho_c^4, \tag{3.15}$$

where P_c is the central pressure and ρ_c is the central density, $a = 4\sigma/c$ is the radiation constant, with σ being the Stefan-Boltzmann constant, μ is the

Table 3.2: List of `modeldata` variables

Variable	Defined as
`n`	Polytropic index
`xi`	ξ_0 Solution radius (dimensionless)
`zfin`	$\frac{d\theta}{dx}\vert_{\xi_0}$, the slope of θ at the solution radius
`Dn`	$D_n = \rho_c/\bar{\rho}$, a useful intermediate variable
`Bn`	$B_n = \frac{3^{(6-2n)/(3n)}}{n+1}\,\xi_0^{-(2n+6)/(3n)}\left(\frac{d\theta}{\xi}\right)_{\xi_0}^{(6-4n)/(3n)}$, a useful intermediate variable
`mx2dthetadx`	$-\xi^2 d(\theta)/d\xi$, a useful intermediate variable

mean molecular weight, m_H is the mass of the hydrogen nucleus, and k_B is Boltzmann's constant. See also Equation (2.40).

But even solving this equation is complicated by the fact that P_c and ρ_c must first be computed or looked up from a pre-computed table. Since our protostars can have polytropic indices other than $n = 3$, we need another way of obtaining the value for β and its derivatives.

For computational efficiency we resort to the use of precomputed tables and then interpolate within these tables. This is what Offner et al. (2009) claim to do as well, though they do not detail their methods. I developed a range of `FORTRAN` routines to generate two special lookup tables. The first, called `modeldata`, stores polytropic parameters for polytropes of different indices. We choose 100 linearly-spaced values of n between $n = 1.5$ and $n = 3.0$. For each of these we solve the Lane-Emden equation (2.2).

The Lane-Emden equation is solved using a fourth-order Runge-Kutta-Felhberg ODE solver. After each solution, we store the variables listed in Table 3.2.

The reasoning behind the use of these intermediate variables is detailed in the theory chapter, but for instance, the expression for the central density is simplified by B_n:

$$P_c = (4\pi)^{1/3} B_n G M^{2/3} \rho_c^{4/3} \tag{3.16}$$

The second lookup table, which we call `betatable`, stores the values for β, $d\log(\beta)/d\log(m)$, and $d\log(\beta/\beta_c)/d\log(m)$ as a function of n and m. We generate the second lookup table by stepping through the Lane-Emden equation using the same Runge-Kutta-Fehlberg method as before, but this time with the knowledge of the intermediate variables, such as B_n, allowing us to solve for the ratio of gas to total pressure (β) at each step and then computing a volume-averaged β at the end.

Finding β_c is trivial then, as it is just the value of β at the center of the polytrope. For polytropes of index $n = 3$, it can shown that β is constant through the volume.

To compute the derivatives with respect to mass, $d\log(\beta)/d\log(m)$ and $d\log(\beta/\beta_c)/d\log(m)$, we use the central difference method.

In generating `betatable`, we hold n constant while solving for these β-variables for potential polytropic masses ranging from about $0.005 M_\odot$ to about $400 M_\odot$. We solve at 50 logarithmically-spaced points between these extremes in mass. We repeat this process again for the next value of n until we reach $n = 3$. Doing it in this order—varying m before varying n—allows us to calculate the central differences on-the-fly and store them as we iterate through our parameter space.

Now that we have lookup tables for model parameters and β-values, we can solve for the equations listed above and in Offner et al. (2009) that evolve our protostar. When retrieving the appropriate value for β or related derivative, my code loads the `betatable` array and uses a bilinear interpolator to interpolate within the parameter space given the protostar's mass m and polytropic index n.

3.3.6 Updating the evolutionary stage

As soon as particular criteria are met, the protostar can advance to the next evolutionary stage, progressing from "Pre-Collapse" to "Main Sequence." Here we summarize the progression. In Table 3.3, we describe the conditions required to advance through the model stages.

Once our sink particles reach the threshold mass of $0.1M_\odot$, the model turns on and the we are at Stage 1 ("No Burning"). We evaluate the central temperature by numerically solving the equation,

$$P_c = \frac{\rho_c k_B T_c}{\mu m_H} + \frac{1}{3} a T_c^4, \tag{3.17}$$

using Brent's method—an efficient, bounded, root-finding algorithm. Solving for T_c is not difficult to do since ρ_c and P_c can be quickly calculated using values stored in `modeldata` for our current polytrope.

When the central temperature exceeds $T_c \geq 1.5 \times 10^6$K, we advance to Stage 2 ("Core burning at fixed T_c"). We set $n = 1.5$, corresponding to a fully convective stellar interior. We remain at this stage until the initial deuterium supply is depleted ($m_d \sim 0$), at which point we switch to Stage 3 ("Core burning at variable T_c"). Offner et al. (2009) then prescribe checking the condition $L_D/L_{\rm ms} > f_{\rm rad} = 0.33$, which is used as a signal for Stage 4 ("Shell deuterium burning"). The star is expected to have formed a radiative barrier, so they prescribe an increase in the radius by a factor of 2.1. After this, the radius slowly contracts and the core temperature increases until the star has contracted onto the main sequence, Stage 5. We check for this by comparing the model radius with the radius of an equivalent main-sequence star described by the Tout et al. (1996) fitting formula,

$$R = \frac{\theta M^{2.5} + \iota M^{6.5} + \kappa M^{11} + \lambda M^{19} + \mu M^{19.5}}{\nu + \xi M^2 + o M^{8.5} + M^{18.5} + \pi M^{19.5}} \tag{3.18}$$

with coefficients:

$$\begin{aligned} \theta &= 1.71535900 & \nu &= 0.01077422 \\ \iota &= 6.59778800 & \xi &= 3.08223400 \\ \kappa &= 10.0885500 & o &= 17.84778000 \\ \lambda &= 1.01249500 & \pi &= 0.00022582 \\ \mu &= 0.07490166 & & \end{aligned}$$

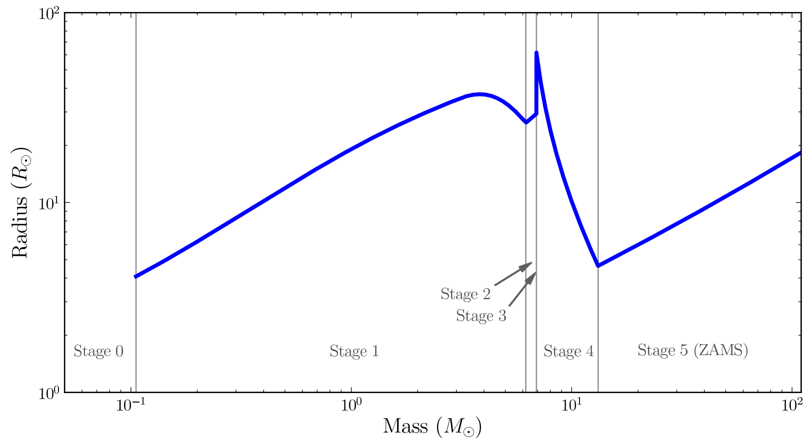

Figure 3.2: The mass-radius relation of a protostar accreting at $10^{-4} M_\odot$/yr. Each of the protostellar stages is marked in the diagram. Stage 3 is such a short-lived stage, that our model often passes through it to Stage 4 within a single timestep. Stage 0 represents an unformed protostar. At Stage 5, the star has joined the main sequence.

When we run the protostellar evolution model for a protostar accreting at a constant rate, we can see how the star transitions through various stages in Fig 3.2, which depicts the mass-radius relation. Vertical lines mark the transitions between stages in our model. Stage 0 represents the unformed protostar. In Stage 1, the protostar is purely a bound object without nuclear fusion of any kind taking place. Any intrinsic luminosity stems from gravitational contraction alone. As more material piles on, the radius swells up to a turnover point, where it begins to contract again. The core temperature rises during this stage, switching the protostar into Stage 2, where deuterium is burned in the core at a constant temperature. Stage 3 is brought about after the exhaustion of initial deuterium reserves and the core temperature is variable. In our simulations of protostellar evolution, the condition for advancement to Stage 4 was true at the same time as the condition for advancement to Stage 3, hence the sink particle spends no time in Stage 3. Transition to Stage 4 is marked by a spike in the radius of the protostar and indicates a transition to radiative stellar core. This is followed by a steady contraction of the protostar until the core becomes hot enough to begin fusing hydrogen, marking its arrival on the main sequence (Stage 5). The stages and the conditions for advancement are recapitulated in Table 3.3.

Table 3.3: Conditions for advancing protostellar evolution model

	Stage	Condition for advancement
0	Pre-Collapse	Mass $m > 0.1\,M_{\odot}$
1	No Burning	Core temperature $T_c \geq 1.5 \times 10^6$ K
2	Core D burning at fixed T_c	Unburned deuterium mass $m_d = 0$
3	Core D burning at variable T_c	Radiation fraction $L_D/L_{\rm ms} > f_{\rm rad} = 0.33$
4	Shell D burning	Radius $R = R_{\rm ms}$
5	Main Sequence	*N/A*

3.4 Raytracing routine

Implementing radiative transfer into hydrodynamics codes has constituted much of the recent work in star formation (Commerçon et al., 2010; Krumholz et al., 2007a,b; Kuiper et al., 2010; Whitehouse & Bate, 2004; Whitehouse et al., 2005) because of the recognized importance of radiation in limiting the fragmentation of the potentially star-forming gas and regulating the star formation rate. To this end we have implemented a radiative feedback code into FLASH which we used for all the simulations described in this thesis.

Radiative feedback codes are usually implemented on top of previously-existing hydrodynamic codes. The relevant equations were discussed in the theory chapter. There are two main approaches to doing this. One popular, though difficult, approach has been flux-limited diffusion (FLD), in which it is assumed that the radiation is tightly coupled to the gas such that they diffuse together, with the radiation behaving essentially like a fluid (Levermore & Pomraning, 1981; Turner & Stone, 2001). This is valid in regions of high gas density where the optical depth is high, i.e. the gas is extremely opaque to radiation. An interpolation is performed (the flux-limiter) for the transition region between optically thick (where the flux $\boldsymbol{F} \rightarrow -c/(3\kappa_R \rho)\nabla E$) and optically thin (where $\boldsymbol{F} \rightarrow cE\boldsymbol{n}$). See Krumholz et al. (2007a).

The other main approach to doing radiative feedback is using raytracing, a technique long used for accurately lighting graphics in 3D visualizations. When applied to a hydrodynamics simulation on an Eulerian grid, virtual "rays" are cast from sources and traced to every cell in the computational domain, allowing one to calculate the proper amount each cell is to receive accounting for any obscuration along the ray path. When combined with other routines for handling the heating, cooling, and ionization of the gas, this technique can be applied to study such problems as the evolution of planetary nebulae (Frank & Mellema, 1994), photoevaporation of cosmological minihaloes (Shapiro et al., 2004), photoevaporation of cometary knots (Lim & Mellema, 2003), the evolution of proplyds (Richling & Yorke, 2000), and now star formation in dense clumps (Peters et al., 2010a).

3.4.0.1 Hybrid characteristics

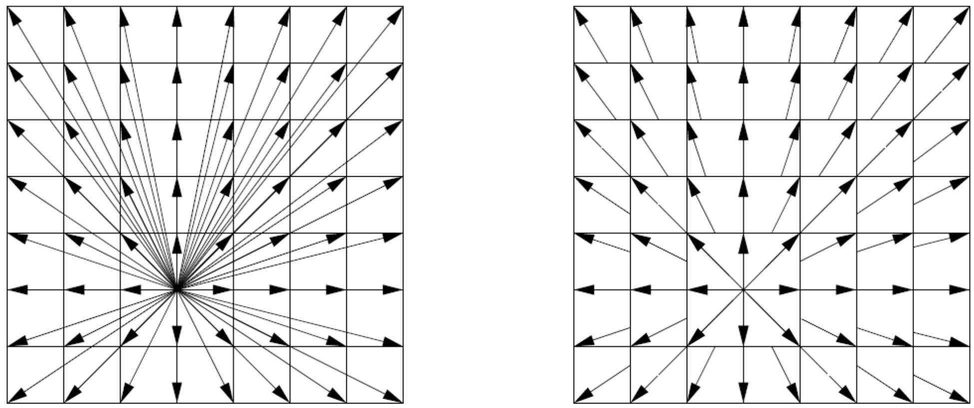

Figure 3.3: A comparison of long characteristics (left) vs short characteristics (right) raytracing as in Rijkhorst et al. (2006). In cells near the source (the star, or sink particle), the long characteristics method suffers from the inefficiency of having to pass many rays through approximately the same part of the cell, whereas the short characteristics approach is efficient but cannot be parallelized.

The task of computing raytracing is simplified when we ignore any emission along the ray and scattering. This is fair to assume if the sources of radiation (stars) dominate the environment. At any given location $\boldsymbol{r}$ in the domain, the specific intensity due to all the sources s in the simulation is

$$I(\boldsymbol{r}) = \sum_s I_s(0) \exp(-\tau_s(\boldsymbol{r} - \boldsymbol{r_s})) \tag{3.19}$$

and is dependent only on the optical depths $\tau_s(\boldsymbol{r} - \boldsymbol{r_s})$ to each of the sources:

$$\tau_s(\boldsymbol{r}) = a_0 N_s(\boldsymbol{r}), \tag{3.20}$$

where a_0 is the absorption cross section, and N is the column density at $\boldsymbol{r}$.

To calculate the specific intensity in any given cell, it's only a matter of adding up the column density contributions along a ray from a source to the destination cell, and then repeating this for all the sources in the simulation. In the "long characteristics" implementation, rays are drawn from the source to each individual cell. This approach is accurate and can be parallelized, but it suffers from an inherent inefficiency: in the cells closest to the source, many rays pass approximately through the same part of the cell, resulting in many redundant calculations of similar column density. It is computationally wasteful.

An alternative approach is called "short characteristics" and the two approaches are contrasted in Figure 3.3. Rather than preforming many redundant calculations, the column density is computed once for each cell along short rays that begin at the cell edge facing the source. To calculate the column density of the cell, the contributions from cells "upwind" towards the source must be known first. This imposes an order on the computations and makes the code inherently serial. The domain cannot be decomposed for multiple processors to work on subsections simultaneously.

Rijkhorst et al. (2006) accomplished a hybridization of these two approaches, combining the desirable qualities of each method: efficiency and parallelizability. Within FLASH, the domain is decomposed into "blocks" of cells. Each block is usually 8x8x8 cells plus guard cells along the edges. The total number of blocks is divided up between processors. "Hybrid characteristics"-based raytracing performs long-characteristic raytracing within each block but a short-characteristic approach is used by rays crossing between blocks.

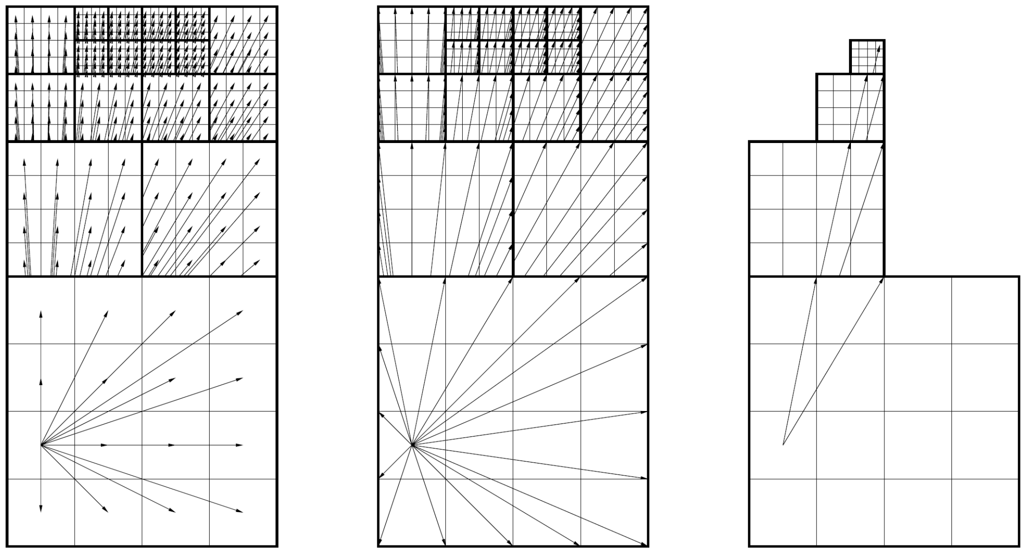

Figure 3.4: Summary of steps taken by the hybrid characteristics module from Rijkhorst et al. (2006). First (left) the column density contribution ΔN is computed along a long ray from source to the cell center. Next (center) the column density contributions to the cell corners along the block edges is computed. When the *total* column density up to a single cell is calculated (right), interpolation is used to properly sum the partial column densities ΔN of rays that passed through the blocks upwind to the source.

Figure 3.4 shows the main steps taken by the hybrid characteristics approach. First (left), on each processor, the column density contribution ΔN is computed along a long ray from source to the cell center. If the source is located in another block, then the long ray is cast from the face closest to the source and the contribution to the column density ΔN is computed from there. Next, as shown in Figure 3.4 (center), the column density contributions to the cell corners along the block edges is computed. This information is then shared between processors. When the total column density up to a single cell is calculated (Figure 3.4, right), interpolation is used to properly sum the partial column densities ΔN of rays that passed through the blocks upwind to the source. In this sense, the long characteristics method is used during the parallel computation of partial column densities, and the short characteristics method is used in the final calculation of total column density. Because this final step involves only interpolating at each block boundary rather than each cell boundary, it is an efficient procedure. Because all the contributions have already been computed in parallel, the algorithm is not forced to visit cells in a particular order. We stress that the process is broken down into stages or loops and only in the final loop does the total accumulated column density from source (star) to final cell get computed for rays that leave the source's block. When there are multiple sources, heating and ionization in each cell from each source needs to be calculated by looping over all the sources. This implies that simulations involving a large number of stars may be prohibitive.

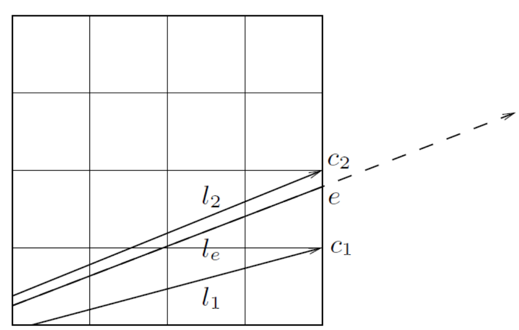

Figure 3.5: From Rijkhorst et al. (2006): A 2D illustration of the linear interpolation method used when calculating the total column density.

A final word on how the interpolation works: When accumulating column density contributions, a ray passing through a particular block takes its contribution from that block by interpolating between values that have already been computed along the block edge (see Figure 3.5). Weights for the cell corner c_1 and c_2 are assigned:

$$w_1 = \frac{|l_2 - l_e|}{l_1 + l_2} \tag{3.21}$$

$$w_2 = \frac{|l_1 - l_e|}{l_1 + l_2} \tag{3.22}$$

which has been normalized so that $w_1 + w_2 = 1$. Then,

$$\Delta N_e = w_1 \Delta N_1 + w_2 \Delta N_2 \tag{3.23}$$

And then finally, the total column density at r is computed

$$N(r) = \sum_b \Delta N_e(b) \qquad [b \in \mathrm{list}(r)] \tag{3.24}$$

3.4.0.2 Ionization, heating and cooling

The radiative feedback module developed by Rijkhorst et al. (2006) makes use of a suite of routines (the DORIC package) for computing ionization fractions and temperatures (Mellema & Lundqvist, 2002; Frank & Mellema, 1994). In the simplified case of treating only hydrogen gas, we find the fractions of HI and HII gas by the equations

$$x(\mathrm{HI}) = \frac{n(\mathrm{HI})}{n(\mathrm{H})} \tag{3.25}$$

$$x(\mathrm{HII}) = \frac{n(\mathrm{HII})}{n(\mathrm{H})} \tag{3.26}$$

where $n(\text{H}) = n(\text{HI}) + n(\text{HII})$ is the number density of hydrogen. HI and HII are respectively the neutral and ionized states of hydrogen. The number of photoionizations per second is computed from Osterbrock (1989):

$$A_p = \int_{\nu_0}^{\infty} \frac{4\pi J_\nu}{h\nu} a_0 d\nu \tag{3.27}$$

where J_ν is the local mean intensity of the radiation field, $a_0 = 6.3 \times 10^{-18}$ cm^2 is the cross-section for ionization in the frequency-independent "grey atmosphere" approximation, and ν_0 is the threshold frequency for ionization.

Meanwhile, the rate of collisional ionizations is estimated by

$$A_c = A_c(\text{HI}) n_e \sqrt{T} \exp(-I(\text{HI})/kT) \tag{3.28}$$

with $A_c(\text{HI}) = 5.84 \times 10^{-11}$ cm^3 K$^{1/2}$. $I(\text{HI})$ is the hydrogen ionization potential taken from Cox (1970).

Recombination is computed (Osterbrock, 1989):

$$\alpha_R = \alpha_R(10^4\text{K}) \left(\frac{T}{10^4}\right)^{-0.7} \tag{3.29}$$

using $\alpha_R(10^4\text{K}) = 2.59 \times 10^{-13}$ cm^{3}s^{-1}.

The total ionization rate $A = A_p + A_c$ and the recombination rate are used to determine the rate equation for hydrogen ionization:

$$\frac{dx(\text{HII})}{dt} = x(\text{HI})A - x(\text{HII}) n_e \alpha_R \tag{3.30}$$

The number density of electrons is given by

$$n_e = n(\mathrm{HII}) + n(\mathrm{C}) \tag{3.31}$$

where the number density of carbon $n(\mathrm{C})$ is included to prevent $n_e = 0$. It is assumed that carbon is always present and singly ionized by the interstellar UV field.

Heating due to photoionization is computed using

$$\Gamma_p = n(\mathrm{HII}) \int_{\nu_0}^{\infty} \frac{4\pi J_\nu}{h\nu} a_0 h(\nu - \nu_0) d\nu \tag{3.32}$$

In the version of this code that we use, Peters et al. (2010a) has included heating from photoionization as well as from the accretion onto stars.

The local mean intensity of the radiation field is found assuming blackbodies as sources with temperatures equal to the effective temperatures of the stellar surfaces. In the case of accretion luminosity, its "effective temperature" is found:

$$T_{\mathrm{acc}} = \left(\frac{L_{\mathrm{acc}}}{4\pi\sigma R_{\mathrm{acc}}^2} \right)^{1/4} \tag{3.33}$$

In Peters et al. (2010a), R_{acc} was found by interpolating the tracks computed by Hosokawa & Omukai (2009). The model we developed uses the self-consistent protostellar radius for R_{acc}. Given the source temperature T_s, then, we have mean intensity of radiation

$$4\pi J_\nu(\boldsymbol{r}) = \left(\frac{R_s}{|\boldsymbol{r}|} \right)^2 \frac{2\pi}{c^2} \frac{h\nu^3}{\exp(\frac{h\nu}{kT_s} - 1)} \exp(-\tau_s(\boldsymbol{r})). \tag{3.34}$$

In this equation, R_s is the radius of the source and τ_s is the optical at $\boldsymbol{r}$ to the source.

Heating of the gas is calculated using a call to the equation of state routine and the pressure of the gas p:

$$p = (n(\mathrm{H}) + n_e)kT. \tag{3.35}$$

Cooling rates are calculated from the cooling curves by Dalgarno & McCray (1972).

3.4.0.3 Radiative transfer in collapse simulations

Peters et al. (2010a) describe modifications to the Rijkhorst et al. (2006) code that were necessary in order for hybrid characteristics raytracing to be used in collapse simulations. The problem with the original code stemmed from the fact that information about the complete block structure of domain was being stored in one large table for each processor. This was done so that for each location (x, y, z) in the domain, the corresponding block identifier could be looked up in the table. This was necessary so that parallel raytracing could be done even as rays traversed potentially multiple blocks and multiple CPUs.

The problem with this approach is that for high-resolution simulation, the block identifier table becomes extremely memory-consuming. Simulations of gravitational collapse (i.e. any star formation simulations) become impossible.

Peters et al. (2010a) were able to get around this problem by exploiting the fact that FLASH already stores information about its block structure. Each block has information about its hierarchy—its parent, child, and neighboring blocks. The problem of relating position in the domain to the correct block identifier is solved by means of a tree-walk algorithm that is comparably fast when compared to looking up the correct value in a large table. These modifications brought collapse simulations with radiative feedback within reach.

3.4.1 Adding a protostellar model with raytracing

Once we had hybrid characteristics raytracing and our protostellar evolution code integrated into FLASH, it was necessary to connect the two codes together. The modifications to the code structure are illustrated in the schematic of Figure 3.6

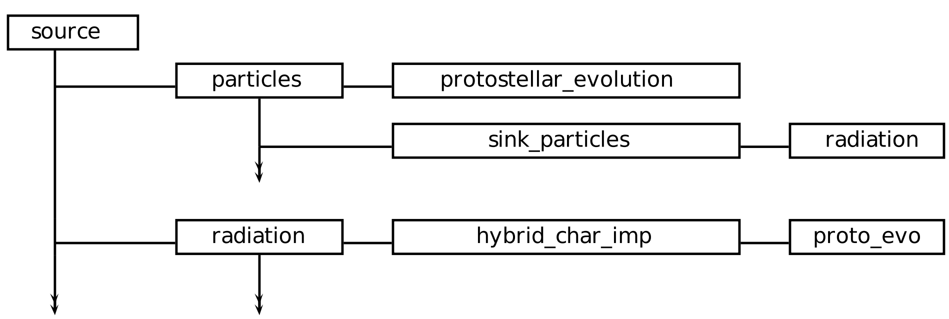

Figure 3.6: Schematic of the radiation and protostellar evolution code layout within the modular structure of FLASH v.2.5

The protostellar evolution code mostly resides in the eponymous subdirectory within the `particles` directory. Here is the code that is called when the particle properties such as radius, intrinsic luminosity, unburned deuterium, etc. are updated. It is also home to the lookup tables `modeldata_table` and `beta_table`.

Integrating our code also required modifying some sink particle data, so we have the `radiation` subdirectory within `sink_particles`. FLASH's modular structure ensures that if different versions of the same file exist in nested subdirectories, the most deeply nested version is the one that is used, provided that simulation setup mandates it. The files in this `radiation` subdirectory update the sink particle code to include the new parameters—intrinsic luminosity, radius, unburned deuterium, polytropic index, and evolution stage—and to update FLASH's main driver to include calls to update these values as the simulation proceeds.

The `hybrid_char_imp` folder represent's Thomas Peters' improvements to the hybrid characteristics raytracer. We go one level deeper in `proto_evo` to modify the raytracing routine so that it directly accesses the particle luminosities and radii. It then computes the stellar effective temperature, integrates a blackbody spectrum using it, and passes that information on to the photoionization routines.

In conclusion, the inclusion of our protostellar model represents a significant improvement over the previous modeling of young stars in cluster simulations. Without a self-consistent model such as the one described in this thesis, Peters et al. (2010a) used a "ZAMS-equivalent" model. New stars are initialized as zero-age main sequence stars, even though their core temperatures may not be sufficient to fuse hydrogen. In this approximation, the radius, luminosity, and effective temperature are all taken as those a ZAMS star of equal mass would have. Peters et al. (2010a) make use of a table containing the values for 60 ZAMS stars with masses spanning the range from $0.1M_{\odot}$ to $100M_{\odot}$. This may be fine for massive stars, which quickly evolve onto the main sequence, but in the case very young stars that haven't accreted much mass, their radii are initially much larger than those of equal-mass zero-age main sequence stars. Large radii result in lower effective temperatures. Knowing the radius and effective temperature accurately is crucial for gauging the feedback. Real protostars will produce less ionization and heating than their ZAMS-equivalent counterparts.

The other problem we avoid with a protostellar model is having discrete jumps in the radius or effective temperature. Since an accreting star in the original Peters et al. (2010a) simulations can be described by only one of 60 possible models in the ZAMS table, its radius will also assume one of 60 discretized values, as shown in Figure 3.7. Discontinuous jumps in the effective temperature may result in unpredicted behaviour when modeling HII regions (see Chapter 4).

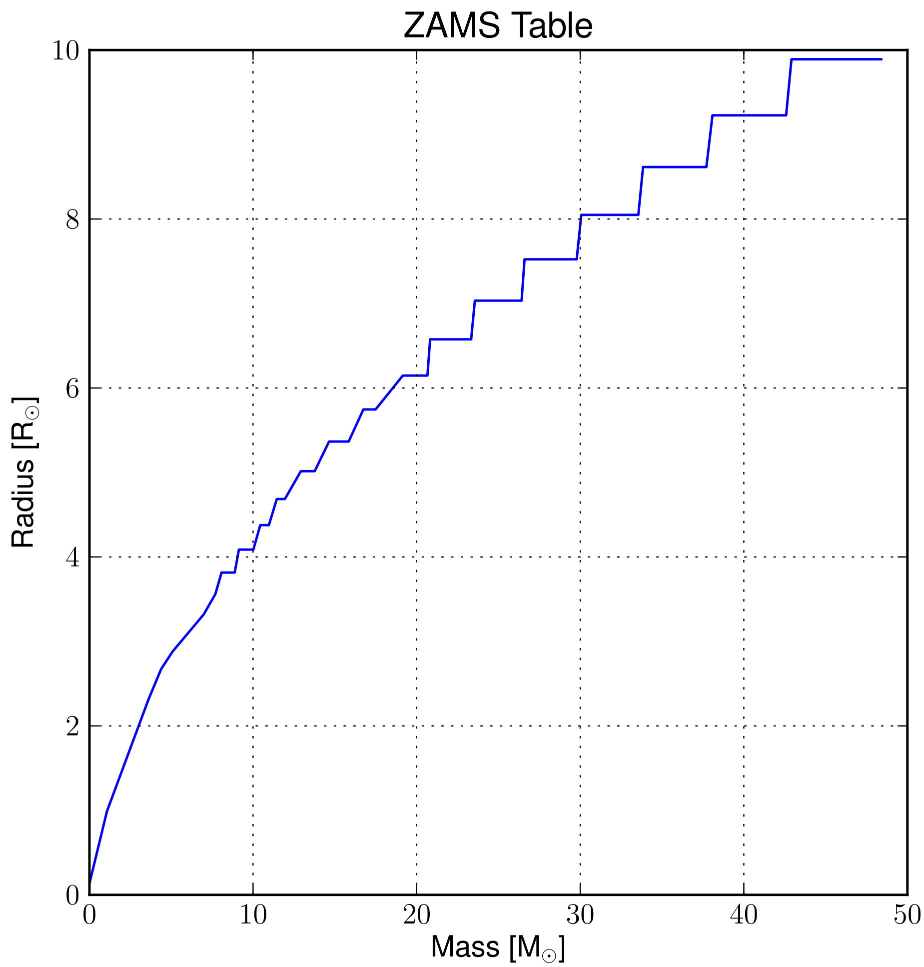

Figure 3.7: An accreting star in the original Peters et al. (2010a) simulations can be described by only one of 60 possible models in the ZAMS table, resulting in discretized values for radius and effective temperature.

Chapter 4

Simulating Protostellar Evolution and Radiative Feedback in the Cluster Environment

N.B.: This chapter will be submitted to the Monthly Notices of the Royal Astronomical Society and summarizes the new research described in this thesis.

4.1 Introduction

The conversion of molecular gas into fully-formed stars is exceptionally complex, involving many diverse processes. These different processes are linked to each other through feedback mechanisms that make isolating and understanding the contribution of each process a difficult task. Stars also rarely form in isolation, but instead are seen to be forming in clusters and subclusters within molecular clouds (Clarke et al., 2000; Testi et al., 2000). In the cluster environment, the formation of one star can affect all the others through the energy it radiates back into cloud. Numerical simulations of star formation have made it very clear that the effects of stellar radiation cannot be neglected. Simulations including some form of radiative transfer show a dramatic reduction in the production of brown dwarfs and other low-mass stars (Offner et al., 2009), due to an increase in gas temperatures shutting down fragmentation (Krumholz et al., 2007a). More of the available gas mass ends up being accreted by the fewer, larger stars formed, and the fragmentation that does occur takes place in optically thick self-shielding discs (Krumholz et al., 2007a; Peters et al., 2010a). The fact that radiation affects the mass spectrum in simulations of molecular cloud clumps has obvious implications for the shape of the initial mass function (Bate, 2009; Krumholz et al., 2010).

Massive stars also emit prodigious amounts of UV radiation (Hoare et al., 2007; Beuther et al., 2007) creating expanding HII regions. The hot (10^4 K) gas expands into the colder (10^2 K) surrounding low-pressure gas, creating another feedback mechanism and ionized region that may contribute to the destruction of molecular clouds (Keto, 2002, 2003, 2007; Matzner, 2002). HII regions can be observed by their radio continuum emission (Mezger & Henderson, 1967), or by their recombination lines (e.g. Wood & Churchwell (1989) use H76α line). More recently, observations have shown time variability in HII regions (Galván-Madrid et al., 2008). Franco-Hernández & Rodríguez (2004) have suggested that such observed time-variability may be due to the changes happening in the source of the ionizing radiation, though it may also be due to increased absorption in the rapidly-evolving core of the nebula. Peters et al. (2010b) present a technique for using synthetic radio maps to study the time-evolution of stars forming in a cluster environment and variability in the morphology and size of HII regions. Analysis of these simulations by Galván-Madrid et al. (2011) confirmed variability in the flux and size measurements of HII regions, which in a few cases might be observable on timescales of ~ 10 years. They also noted that positive changes were more likely to occur than negative changes, i.e. that most of the flux variations were increases rather than decreases.

To further explore the impact of radiative feedback and the possible variability in HII regions, simulations must be equipped with good protostellar models. These have been investigated by Palla & Stahler (1991), Palla & Stahler (1992), Nakano et al. (2000), McKee & Tan (2003), Offner et al. (2009) and Hosokawa & Omukai (2009), among others. It is clear from these models, that the evolution of a protostar depends heavily on the mass accretion rate. Among other things, they show that the radius of the protostar may grow or contract depending on the stellar evolutionary stage. This means that if the effective temperature can change significantly over a short period of time, changes in the observed flux or size of HII regions may betray evolutionary changes taking place in the stars themselves, whose ionizing radiation is driving the region. To this end, we simulate an expanding HII region driven by a single, accreting star in an initially homogeneous and isotropic medium and equip the star with a protostellar evolution model based on the one described in Offner et al. (2009). We see that the state of the protostar can definitely affect the size of the HII region.

The implementation of a protostellar model may also affect the global evolution of a cluster. By accurately computing the luminosity of very young stars, which are often modeled simply as zero-age main sequence stars, gas heating and ionization within the cluster should be reduced and this could result in different stellar population dynamics. To gauge the impact of protostellar modeling on star clusters, we run simulations both with either a self-consistent protostellar model in place or with a ZAMS description of stars.

The key effect of this accurate protostellar modeling was the presence of more lower-mass stars ($< 10M_{\odot}$) in cluster simulations involving the protostellar model, which could been a consequence of less early-stage heating and ionization. Other effects were delayed ionization of the cluster gas by 3% of a freefall time, delayed heating of the cluster gas by 1% of a freefall time, and a collapse of the HII region around a single protostar during its transition to a radiative interior structure.

Our numerical approach is described in Section 4.2. In Sections 4.3 and 4.4 we list our results for the evolution of a single accreting massive star in a uniform medium and the early evolution of star clusters with massive stars, respectively. Our assessment of the impact of protostellar modeling we discuss in Section 4.5 and summarize our findings in Section 4.6 with a view to future simulations.

4.2 Numerical methods

We perform numerical simulations using the FLASH hydrodynamics code (Fryxell et al., 2000) in its version 2.5. It is an adaptive-mesh refinement code that solves the gas-dynamic equations on an Eulerian grid and includes self-gravity, cooling by dust, and radiative transfer. It has been modified to include Lagrangian sink particles (Banerjee et al., 2009; Federrath et al., 2010) to represent (proto)stars, and a raytracing scheme to handle ionizing and non-ionizing radiation feedback from stars originally developed by Rijkhorst et al. (2006), then extended and optimized by Peters et al. (2010a). We subsequently added an additional module to handle the protostellar evolution of our sink particles, which is based on a subgrid physics model described in detail by Offner et al. (2009) and outlined in Chapter 3. The protostellar evolution model evolves the stellar radius and intrinsic luminosity of our sink particles and describes their nuclear burning state. The protostellar model connects directly to the radiation module so that stellar surface temperatures and stellar radii are handled self-consistently.

4.2.1 Radiation

Radiative transfer in our simulations is handled by a "hybrid-characteristics" raytracing scheme developed by Rijkhorst et al. (2006) to handle photoionization and heating due to point sources of radiation. Ionization, heating, and cooling processes are handled using the DORIC routines (Frank & Mellema, 1994; Mellema & Lundqvist, 2002). Rijkhorst et al. (2006) demonstrated the raytracing method's efficacy at casting well-defined shadows. The hybrid characteristics method is one that optimizes for both efficient raytracing and parallelizability. Peters et al. (2010a) then adapted the code to handle simulations of multiple collapsing regions and clustered star formation. Peters et al. (2010a) tested the code against handling a D-type ionization front, comparing it to the approximate solution found by Spitzer (1978), while the code's ability to handle R-type ionization fronts has already been tested by Iliev et al. (2006).

4.2.2 Protostellar model

The radiative feedback model is coupled directly to the sink particles. Rays are cast outwards from each sink particle and the column density along each ray computed using the hybrid-characteristics scheme described in Rijkhorst et al. (2006). At each cell in the computational domain, the photoionization rate and heating rate are calculated. These are set by the specific mean intensity along the ray,

$$J_\nu(r) = \left(\frac{r_{\rm star}}{r}\right)^2 \frac{1}{2c^2} \frac{h\nu^3}{\exp(h\nu/k_{\rm B}T_{\rm star}) - 1} \exp\left[-\tau_{\rm ion}(r)\right], \tag{4.1}$$

which depend on a knowledge of the radius of the star $r_{\rm star}$. Previously, a lookup table of ZAMS-equivalent stars (Paxton, 2004) had been used.

For the accretion radius $r_{\rm acc}$ and effective temperature $T_{\rm acc}$ of the accretion luminosity, Peters et al. (2010a) used a prestellar model that interpolated between a set of evolutionary tracks computed by Hosokawa & Omukai (2009). Accreting material has its potential energy deposited as radiation at the surface of the star, so ideally $r_{\rm acc} = r_{\rm star}$, but each is handled separately. The models of Hosokawa & Omukai (2009) also suggest that an evolving protostar will have a radius larger than zero-age main sequence star of equal mass. Consequentially, the surfaces of protostars will be cooler, resulting in fewer UV photons being emitted.

In the earliest stages of star formation, the total luminosity of a protostar will be dominated by the accretion luminosity. For a star accreting at a rate of $10^{-3} M_\odot$ yr^{-1}, only after the star grows to be about 8 $M_\odot$ does the instrinsic luminosity of the star overtake the accretion luminosity, according to our simulations. The accretion luminosity is given by

$$L_{\rm acc} = \frac{GM\dot{M}}{r_{\rm acc}} \tag{4.2}$$

and the prestellar model of Peters et al. (2010a) used the accretion rate $\dot{M}$ as the independent variable when interpolating between the evolutionary tracks of Hosokawa & Omukai (2009) to obtain the accretion radius. A rapidly fluctuating accretion rate would result in a rapidly fluctuating estimate of the accretion radius inconsistent with the model for the stellar radius.

We have improved upon the prestellar model by adding a self-consistent subgrid physics model for the stellar radius and instrinsic luminosity of the star based on the model described in Offner et al. (2009). Stars are modeled as polytropes and every sink particle in our simulation is assigned several additional properties: a stellar radius $r_{\rm star}$, an intrinsic luminosity $L_{\rm int}$, a polytropic index n, an unburned deuterium mass m_d, and a nuclear burning evolutionary stage. At every timestep in our simulation, we evolve this handful of variables according to the equations given in Offner et al. (2009). The model is based on a one-zone protostellar evolution model introduced by Nakano et al. (1995) and expanded on by Nakano et al. (2000) and Tan & McKee (2004).

When a sink particle's mass exceeds $0.1 M_\odot$, we activate our protostellar evolution code and initialize the radius and polytropic index respectively as

$$r = 2.5\ R_\odot \left(\frac{\Delta m / \Delta t}{10^{-5}\ M_\odot\ \mathrm{yr}^{-1}} \right)^{0.2} \tag{4.3}$$

$$n = 5 - 3 \left[1.475 + 0.07\ \log_{10} \left(\frac{\Delta m / \Delta t}{M_\odot\ \mathrm{yr}^{-1}} \right) \right]^{-1} \tag{4.4}$$

For cool stars, the Hayashi limit sets the luminosity, but above this a main sequence luminosity is assumed. Thus, $L_{\mathrm{int}} = \max(L_H, L_{\mathrm{ms}})$, with $L_H = 4\pi R^2 \sigma T_H^4$ and $T_H = 3000$ K. ZAMS values are computed using the fitting formulas by Tout et al. (1996).

The radius of the protostar is evolved using a discretized version of an equation found in Nakano et al. (2000):

$$\begin{aligned} \Delta r = {} & 2\,\frac{\Delta m}{m} \left(1 - \frac{1 - f_k}{a_g} + \frac{1}{2} \frac{d \log \beta}{d \log m} \right) r \\ & - 2\,\frac{\Delta t}{a_g \beta} \left(\frac{r}{G m^2} \right) (L_{\mathrm{int}} + L_I - L_D)\, r, \end{aligned} \tag{4.5}$$

where L_I is the energy per unit time required to ionize incoming material, L_D is the energy produced burning deuterium, β is the ratio of mean gas pressure to total pressure (gas + radiation) in the star, $a_g = 3/(5-n)$ is the coefficient describing the gravitational binding energy, and f_k is the fraction of the kinetic energy that is radiated away by the infalling material before it reaches the stellar surface. The details of a sink particle's evolution are described in Appendix B of Offner et al. (2009). Apart from initializing our model at a higher starting mass (explained in Section 3.3), the only other significant difference was that we do not distinguish between accretion onto the stellar surface versus accretion onto the stellar disk in describing the accretion luminosity. Our accretion luminosity is taken to be purely $L_{\rm acc} = GM\dot{M}/R$. We also rely on tables of polytropic stellar parameters that we computed ourselves. In all other respects, our protostellar model follows the one described in Offner et al. (2009).

Protostars evolve through multiple distinct nuclear stages in this code during which the radius is at times expanding (such as during the early accretion phase) and at times contracting (such as during the end stage as the protostar approaches the main sequence to be a mature star). Once our stars reach the main sequence, we assign them a radius and luminosity based on the fitting formulas of Tout et al. (1996). We neglect any special treatment of metallicity-related effects and consider only stars of solar metallicity.

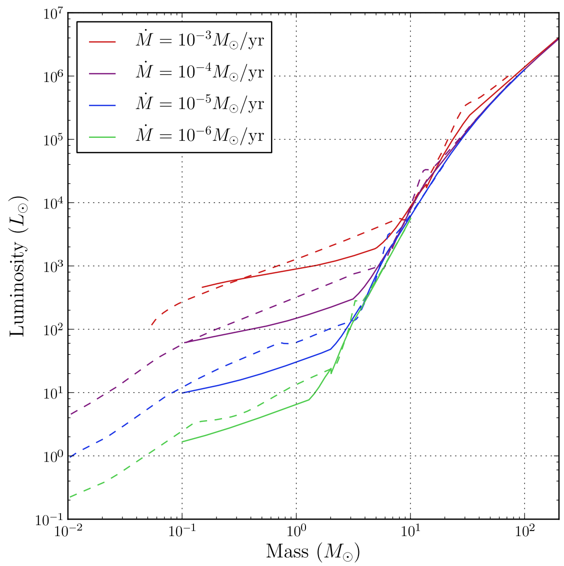

(a) Luminosity evolution for protostars accreting mass at various rates. The solid lines show the intrinsic (stellar) luminosity following our protostellar evolution code, whereas the dashed lines show the luminosity derived from detailed protostellar modeling by Hosokawa & Omukai (2009).

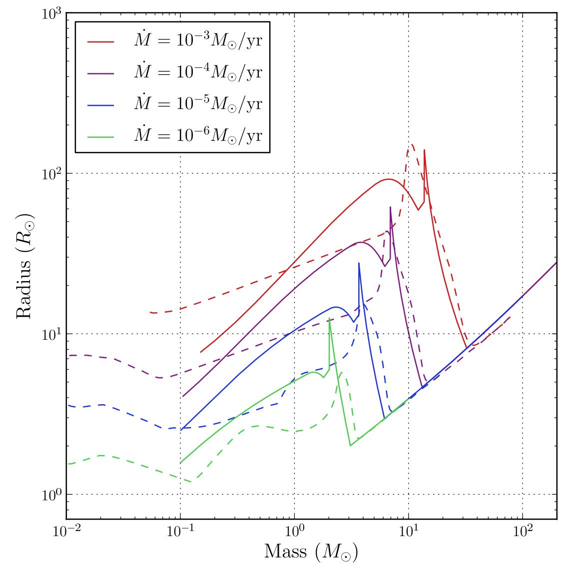

(b) Mass-radius relation for accreting protostars. The solid lines show the stellar radius following our protostellar evolution code, whereas the dashed lines show the luminosity derived from detailed protostellar modeling by Hosokawa & Omukai (2009).

Figure 4.1: The mass-luminosity and mass-radius relations of the protostellar model employed.

In Figures 4.1(a) and 4.1(b) we compare the results from our protostellar evolution code, which is based on the model described in Offner et al. (2009), to more detailed, full-3D numerical simulations of protostellar accretion completed by Hosokawa & Omukai (2009). These are expected to be more accurate than our one-zone modeling. However, we emphasize that a one-zone model is more complex than merely fitting to a predefined track. Track-fitting would be perfectly fine if material were accreting onto a star at a steady rate. Instead, accretion rates in real clusters and in our simulations vary signficantly with time. If we were fitting to a track based on instantaneous accretion rate, a rapidly-fluctuating rate would correspond to a stellar radius fluctuating in size with equal rapidity—an unphysical result. Instead, the radius must be evolved in size according to some self-consistent model that takes into account environmental factors such as the accretion rate. This is what our model is designed to do.

We compare the behaviour of our code at different accretion rates ranging between a slow $10^{-6} M_{\odot}/\mathrm{yr}$ to a rapid $10^{-3} M_{\odot}/\mathrm{yr}$. These represent the typical range of accretion rates we see in our simulations and expect of stars forming in clusters within molecular clouds. The stability of the code was tested over a range of accretion rates and timestep sizes. Although our tracks do not agree perfectly with the Hosokawa & Omukai (2009) simulations, the agreement is to within the same order of magnitude as their results and represents a self-consistent model for the radius and luminosity of an evolving protostar—a significant improvement over previous ZAMS-based estimates. In future,

Table 4.1: Table of fiducial values for protostellar evolution at various accretion rates

$\dot{M} = 10^{-3} M_{\odot}/\mathrm{yr}$

	Stage 1 No burning	Stage 2 Core D burning at fixed T_c	Stage 3 Core D burning at variable T_c	Stage 4 Shell D burning	Stage 5 Main sequence
$M_*/M_{\odot}$	0.15	12.10	13.65	13.70	32.30
$R_*/R_{\odot}$	7.69	58.94	66.39	139.92	8.16
$L_*/L_{\odot}$	2.86	10081	14514	14673	141000

$\dot{M} = 10^{-4} M_{\odot}/\mathrm{yr}$

	Stage 1 No burning	Stage 2 Core D burning at fixed T_c	Stage 3 Core D burning at variable T_c	Stage 4 Shell D burning	Stage 5 Main sequence
$M_*/M_{\odot}$	0.10	6.16	6.88	6.89	13.12
$R_*/R_{\odot}$	4.08	26.27	29.33	61.64	4.64
$L_*/L_{\odot}$	1.14	1107	1618	1622	12894

$\dot{M} = 10^{-5} M_{\odot}/\mathrm{yr}$

	Stage 1 No burning	Stage 2 Core D burning at fixed T_c	Stage 3 Core D burning at variable T_c	Stage 4 Shell D burning	Stage 5 Main sequence
$M_*/M_{\odot}$	0.10	3.28	3.65	3.65	6.13
$R_*/R_{\odot}$	2.51	11.81	13.14	27.59	2.96
$L_*/L_{\odot}$	0.45	113.02	168.69	168.77	1084.14

$\dot{M} = 10^{-6} M_{\odot}/\mathrm{yr}$

	Stage 1 No burning	Stage 2 Core D burning at fixed T_c	Stage 3 Core D burning at variable T_c	Stage 4 Shell D burning	Stage 5 Main sequence
$M_*/M_{\odot}$	0.10	1.79	2.01	2.01	3.08
$R_*/R_{\odot}$	1.58	5.33	5.98	12.55	2.01
$L_*/L_{\odot}$	0.18	10.05	16.19	16.19	88.38

Table 4.2: Description of the stellar evolutionary stages in the protostellar module

	Stage	Features
0	Pre-Collapse	Mass $m \lesssim 0.1\,M_\odot$ Cannot dissociate H_2 and cause second collapse to stellar densities.
1	No Burning	Object has collapsed to stellar densities. T_c still too cold to burn D. $T_c \lesssim 1.5 \times 10^6$ K Radiation comes purely from gravitational contraction. Star is imperfectly convective.
2	Core D burning at fixed T_c	Temperature reaches required $T_c \sim 10^6$ K to burn deuterium. D burning acts as a thermostat keeping temperature constant. Star is fully convective.
3	Core D burning at variable T_c	D is exhausted. Core temperature now rising again. Star remains fully convective. Accreted D dragged down to core and burned. Rising core temperature reduces opacity. Convection in the stellar core eventually shuts down.
4	Shell D burning	Star core changes to a radiative structure. D burns in a shell around the core. Radius swells.
5	Main Sequence	Star has contracted enough for T_c to reach $\sim 10^7$ K Hydrogen ignites and star stabilizes onto the main sequence.

we hope to calibrate our models to match their predictions for radius and luminosity more closely.

In Table 4.1 we list some fiducial values for the mass, radius, and luminosity of a protostar in our model at different stages in its pre-main-sequence lifetime and for different accretion rates. The luminosities listed in Table 4.1 are the intrinsic stellar luminosities. The luminosity shown in Figure 4.1(a) is the total lumonsity ($L_{\rm tot} = L_{\rm int} + L_{\rm acc}$), which we use to compare our results with the stellar structure calculations of Hosokawa & Omukai (2009).

The various stages of our protostellar code, following Offner et al. (2009), are summarized in the Table 4.2.

4.2.3 Initial conditions

The strength of the radiative feedback code we employ lies in its ability to produce realistic HII regions. It was believed, however, that since zero-age main sequence stars of equal mass are used as estimates for protostellar properties such as surface temperature, the ionizing flux would be overestimated (Peters et al., 2010a). To study the effects of using a self-consistent protostellar model as described above, we ran several simulations with and without the protostellar model in place.

4.2.3.1 Single accreting star simulations

A cluster environment is highly tumultuous even when initial turbulent gas dynamics and magnetic fields are ignored. The HII regions formed in such an environment are highly amorphous and time-variable. We first wanted to isolate the effects of the protostellar code to gauge its impact on HII region formation. To this end, we selected a box of side length 0.2 pc filled with uniform, isothermal molecular gas at 10K and density $\rho = 1 \times 10^{-17}$ g cm^{-3}. Self-gravity is switched off for this test.

At the center of this simulation volume is placed a single sink particle of the same kind as before. It is set to accrete mass at a fixed rate of $\dot{M} = 10^{-3} M_{\odot}/\mathrm{yr}$. The accretion rate in our cluster simulations is highly variable. By fixing the accretion rate we are able isolate the effects of the protostellar model on HII region formation.

Table 4.3: Runtime parameters of the clustered star formation simulations

Run	Mass	Density profile	Temp	Rotation	Stellar Model	Feedback
1	$1000M_\odot$	$r^{-3/2}$	30 K	$\beta = 0.05$	Protostellar	Radiative; raytracing method
2	$1000M_\odot$	$r^{-3/2}$	30 K	$\beta = 0.05$	ZAMS	Radiative; raytracing method

We run simulations like this both with and without the protostellar evolution model in place. When the protostellar evolution code is not running, we use the previous ZAMS-equivalent model as in the cluster setup. We track the growth of the HII region with time for each of the two setups.

4.2.3.2 Cluster models

We chose to repeat the cluster simulations described in Peters et al. (2010a) with similar initial conditions. Because we used the same FLASH code, sink particles, and radiative feedback code, we can isolate the effect of including a protostellar evolution model. We begin with a $1000M_\odot$ self-gravitating cloud of molecular hydrogen at an initial temperature of 30 K. The cloud is in solid body rotation with a ratio of rotational to gravitational energy of $\beta = 0.05$. Our simulation box is 3.89 pc on a side. The density profile features a flat central region extending out to a radius of 0.5 pc, then falling off according to an $r^{-3/2}$ power law. The central density is $\rho_c = 1.27 \times 10^{-20}$ g cm^{-3}. The density drops off until reaching an ambient cutoff density of $\rho_{\rm ext} \approx 9.76 \times 10^{-23}$ g cm^{-3}.

We note that clumps of this size and mass are expected to be turbulent (Blitz, 1993; Evans, 1999; Williams et al., 2000). However, in order to build up physical understanding of the complex process of cluster formation, we follow Peters et al. (2010a) in this study so that we can isolate the important radiative feedback effects. Turbulence will be added in subsequent papers.

We ran two simulations: one using a ZAMS-based model for stellar effective temperature and stellar radius, with the accretion radius calculated as a separate quantity by interpolating to fixed tracks as described above; and a second simulation with the self-consistent protostellar model as in Offner et al. (2009) that evolves stellar radii and luminosities along with the simulation.

As the simulation progresses, the original mass profile of the clump quickly disappears and is replaced with a rotating central disk. Stars, represented by sink particles, are allowed to form when the local conditions are satisfied as in Federrath et al. (2010).

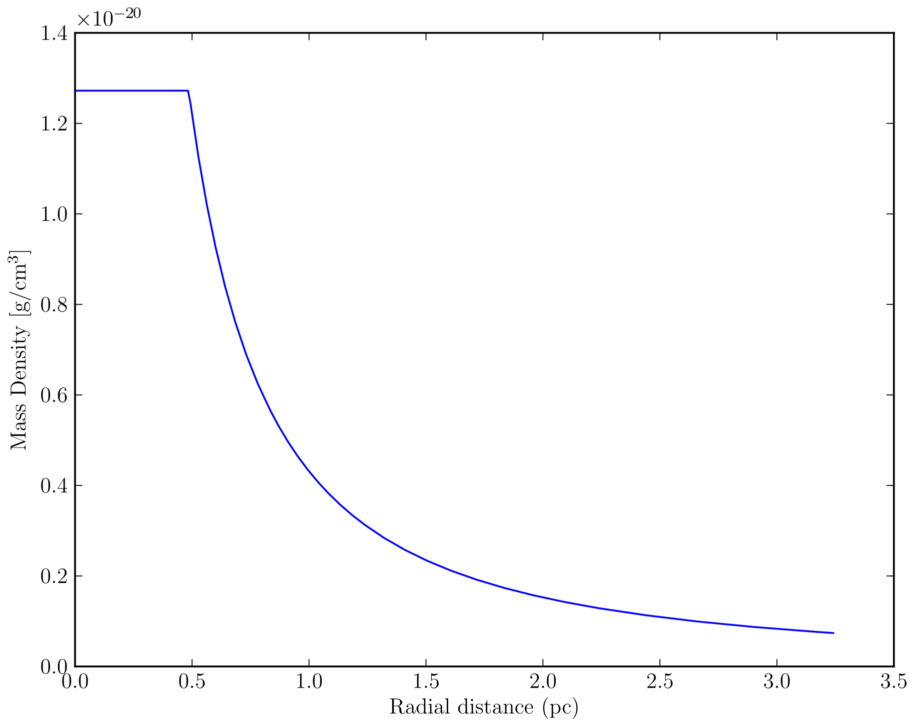

Figure 4.2: Radial mass density profile of the molecular gas in the "cluster" setup showing a flat central region extending to a radius of 0.5pc, followed by a dropoff with an $r^{-3/2}$ power law profile.

4.3 Accretion onto a single star and the formation of HII regions

In an effort to understand whether the use of a protostellar model in a star formation simulation would have any detectable effects on the growth or variability of HII regions, we simplified our simulation setup to a single star. With its position fixed at the center of our 0.1 pc box, we ran the simulation for approximately one freefall time, or about 22,000 years. This was enough time for the star to accrete about $20M_{\odot}$ in mass. Following our protostellar model, the star has almost reached the main sequence at this stage. At the end of the simulation, the star is in a state of contraction.

Figure 4.3 shows the results of the simulation including the protostellar code. In it, the accretion rate is held fixed at $10^{-3} M_{\odot}/\mathrm{yr}$. The gas is non-self-gravitating, but responds gravitationally to the presence of the star. Radiation pressure has been neglected and no magnetic fields are present. The figure consists of a series of panels showing the various particle properties with panels in the left column reflecting these star properties as a function of stellar mass. The panels in the right column are the same properties but with respect to time counted in units of freefall time.

The grey vertical bars in our plots show important transitions between stellar states. The stages in our protostellar code follow those in Offner et al. (2009). The first vertical bar indicates the ignition of deuterium inside the star (Stage 2 in Table 4.2). This can only begin when the core temperature exceeds approximately 1.5×10^6K. Any radiation prior to this stage comes from gravitational contraction. The stellar luminosity is that of a Hayashi track star with a surface effective temperature of 3000K.

The second grey vertical bar indicates another important transition: when the core changes to a radiative structure and deuterium burning continues in an outer shell. The model prescribes a radius increase by a factor of 2.1 at this stage to reflect the change in stellar structure and the shell deuterium burning. This corresponds to Stage 4 in Table 4.2.

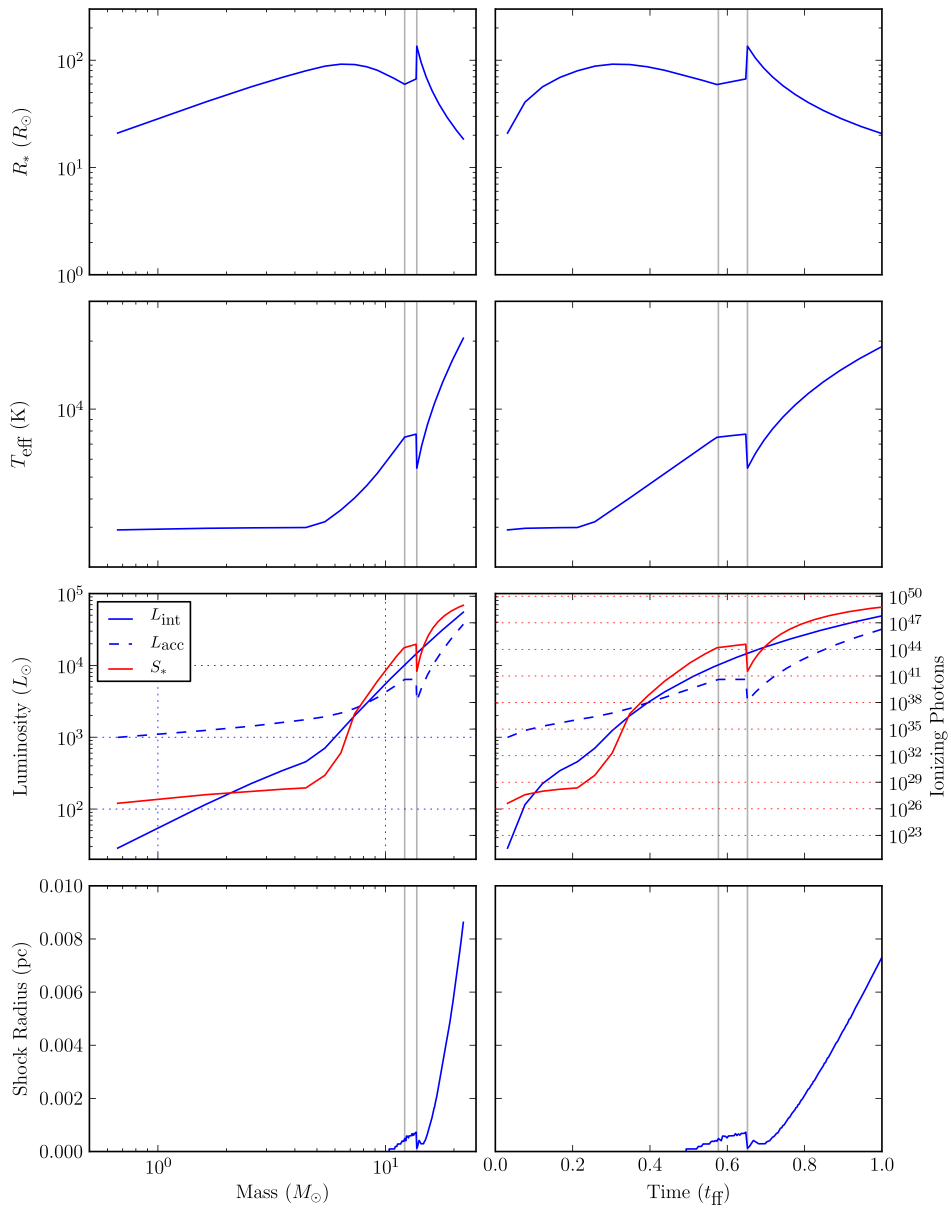

Figure 4.3: Results from a simulation of a single star in an initially uniform medium, accreting at a rate of $10^{-3} M_\odot$/yr, following a protostellar evolution model. The solid grey vertical lines depict evolutionary transitions: the first indicates the onset of deuterium fusion in the core (Stage 2), the second indicates the transition to a radiative structure in the core and the onset of deuterium fusion in shell causing a swelling of the radius (Stage 4). When the radius swells, the effective temperature and ionizing flux dip. This causes the HII region to collapse, as seen in the bottom panels showing shock radius. Time is given in units of freefall time, with $t_{\rm ff} \approx 21,000$ years. Stages correspond to those listed in Table 4.2.

The sudden change in radius of the star results in a sudden drop of several thousand Kelvin in the effective temperature. It also results in a dip in the accretion luminosity by about 2000 $L_\odot$.

In Figure 4.3 we also see how the accretion luminosity initially exceeds the star's intrinsic luminosity by more than an order of magnitude. Obviously, this is mostly due to the high accretion rate. For an accretion rate of $\dot{M} \approx 2 \times 10^{-5} M_\odot/\mathrm{yr}$, the initial accretion and intrinsic luminosities would be approximately equal.

Overplotted in the third row of Fig. (4.3) is S_*, the rate of production of ionizing photons. The scale axis is on the right of the figure. This rate was computed by numerically integrating a blackbody function at each temperature over an interval bounded below by the ionization energy for a hydrogen atom, then multiplying this flux by the surface area of the star at its current radius.

The shape of this ionizing luminosity curve is especially interesting when we compare it to the fourth row of panels. Here we show the radius of the HII region. Once the star in our simulation has accreted about $10 M_\odot$ of material, its surface temperature (5000K) has become high enough for the ionizing flux ($\sim 10^{41}$ photons/sec) to begin producing an HII region. There is evidently slow, unsteady growth of the HII region until the transition to shell deuterium burning (second grey vertical line) and the swelling of the stellar radius. This sudden drop in stellar surface temperature (from $\sim$ 7700K to $\sim$ 5500K) drops the ionizing flux sufficiently (from 4×10^{44} s^{-1} to 3×10^{41} s^{-1}) for the HII region to virtually disappear. Prior to collapse the HII region had grown to about

300 AU diameter. Over the course of one timestep (93 years), its size drops to 54 AU. The recombination timescale at the temperatures (10^4 K) and number densities ($n \sim 10^4$ cm^{-1}) present inside our hypercompact HII region is on the order of years. It's a short-lived transition, however, and the HII region quickly begins to grow again. In about 1.8 kyr, the HII region has returned to its pre-collapse size. There is some fluctuation in the region size immediately following the collapse and then, after about 0.7 freefall times (14.7 kyr), the growth is steady and linear.

We computed the size of the HII region by evaluating the ionization fraction along a line starting at the center of the simulation box, where the particle is located, out along one of the axes to the edge of the simulation box. We take the radius of the shock to be where the ionization fraction switches from virtually fully ionized ($x \approx 1$) to neutral ($x \approx 0$). Rather than taking the nearest grid cell as our radial coordinate, we interpolate to find the equivalent radial coordinate where the ionization fraction is $x = 0.5$, i.e. the center of the shock front.

Variability in the size of HII regions had been suggested in Peters et al. (2010a). The ultracompact regions observed in their simulations were highly variable in both time and shape and replicated observed morphologies (Wood & Churchwell, 1989; Kurtz et al., 1994). Large changes on the order of 20-30% in size over the course of ~10 years have also been described in Franco-Hernández & Rodríguez (2004). Rodríguez et al. (2007) also describe systematic changes in the continuum emission from one source. Observations of newly-formed massive stars also show variability in their radio emission (Galván-Madrid et al., 2008) inconsistent with the standard picture of a steadily expanding HII region (Spitzer, 1978).

Given the tumultuous environments in which massive stars form, variability in the HII regions might be expected. Nevertheless, the textbook picture was of a spherical ionized region expanding into a quiescent medium at the sound speed of the ionized gas. The ionizing source was an already-formed massive star that had finished accreting new material. But realistic conditions involve massive stars forming in clusters (Zinnecker & Yorke, 2007) within molecular clouds. These have a chaotic velocity structure and show a network of filaments (Myers, 2009), with filaments being the primary birthplaces of prestellar cores (Arzoumanian et al., 2011). The cloud may be threaded with magnetic fields and the gas around a core is likely rotating. Accretion onto a protostar appears highly variable in simulations (Peters et al., 2010a) and should be expected, as accreting protostars pass through fragmented gas or enter/exit filaments. These changing conditions are likely to affect the ionizing flux coming from the surfaces of these accreting stars. Temporal and spatial variability in the HII regions they are producing might thus be expected.

Here, however, we see something new: Accretion onto the protostar is held fixed. The environmental conditions are about as quiescent as possible: 10K non-self-gravitating gas without any initial velocity field or initial density structure. The standard picture of HII region formation assumes an adult star, but in our simulation the protostar has yet to reach the main sequence. It is still passing through distinct stages in its evolution, its radius at various times growing and other times shrinking. When we more closely track the ionizing luminosity, and see it suddenly drop three orders of magnitude with the transition in stellar structure to shell deuterium burning, with a concomitant collapse of the HII region, we see that HII regions can vary quite apart from changing environmental conditions. Variability in HII regions can signal changes occurring during the evolution of a protostar. A rapid decrease in the size of an HII region in otherwise quiescent conditions could tell us more about the process of massive star formation by testifying to nuclear processes in the protostar, even as the protostar's intrinsic luminosity has not shared in the fluctuation. Note that Fig. 4.3 does reveal a dip in the accretion luminosity corresponding to the jump in stellar radius, but the accretion luminosity is at this stage almost an order of magnitude weaker than the intrinsic luminosity.

Figure 4.4 tells a different story. When we ran our simulation of a single star accreting at a fixed rate, fitting stellar radius and luminosity to a ZAMS model, we saw some unexpected behaviour. The panels in the top row for Figure 4.4 show the radius of the star. In the Peters et al. (2010a) simulations, the ZAMS-based model that was employed had two separate descriptions of the protostellar radius. The actual radius of the star was found by matching the star to an entry in a table of 60 ZAMS values ranging from $0.1M_{\odot}$ to $100M_{\odot}$, with more finely spaced entries at the lower-mass end. The accretion radius was accounted for separately by using the accretion rate to interpolate between the protostellar tracks computed by Hosokawa & Omukai (2009). The concern with this approach is that there is no self-consistent description of the stellar radius, as seen by the poor agreement of the two radii in the first row panels. Also, when the accretion rate in a simulation fluctuates rapidly, the

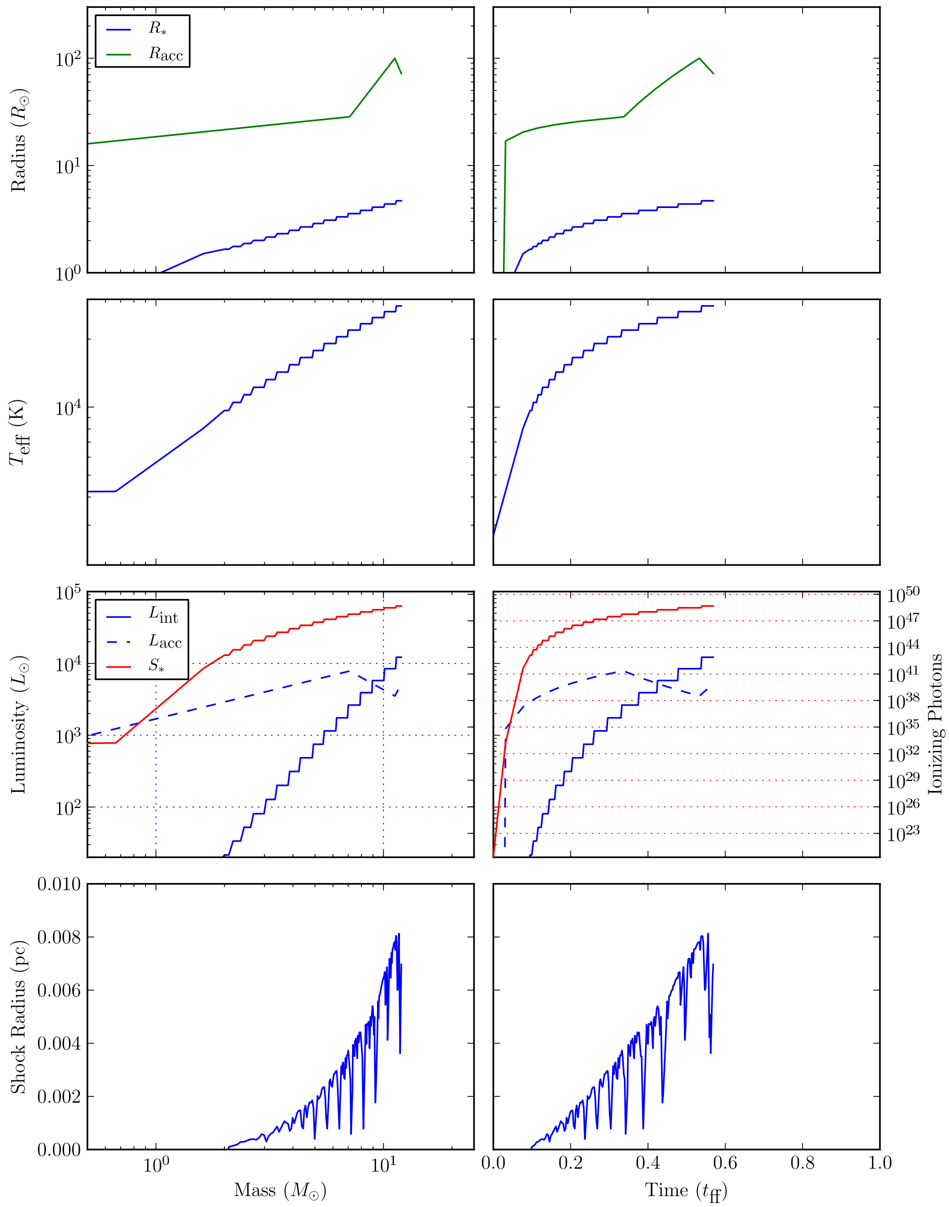

Figure 4.4: Results from a simulation of a single star, accreting at a rate of $10^{-3}M_\odot$/yr, without the self-consistent protostellar model enabled. The model used is a fit to a ZAMS table with 60 discrete entries for stars ranging in mass from $0.1M_\odot$ to 100. No interpolation between table entries has been used. This model follows the type used in the cluster simulations of Peters et al. (2010a). The ionized region expands (on average), but with a great deal of fluctuation as regions internal to the shock front recombine and then reionize a short time afterward. These fluctuations are unphysical and reflect a problem with the way the ZAMS model was implemented in Peters et al. (2010a). The freefall time is $t_{ff} \approx 21,000$ years.

accretion radius fluctuates with it on the same timescale because it is just an instantaneous fit to another model. There is no self-consistent evolution of the radius as the protostar accretes mass. In the Peters et al. (2010a) simulations, the accretion radius was used to calculate a contribution to the nonionizing heating. While a rapidly fluctuating accretion radius is unphysical, its impact on the cluster simulations would not have been severe because most of the heating and ionization was still based on stellar radius and luminosity, which were being fit to a ZAMS table.

The second row of panels show effective temperature of the star, also culled from a table of ZAMS values. Again, because of the finer spacing of table values at the lower-mass end, the discrete jumps are visible only once a significant mass has been accreted. It is the effective temperature that is used to compute the ionizing flux $S*$, which is the number of photons produced by the star, modeled as a blackbody, that are above the threshold frequency for the ionization of hydrogen. In the same panels of row 3 in Figure 4.4 we show the intrinsic and accretion luminosities, with the left axes corresponding to luminosity and right axes corresponding to photon count.

The final row of panels shows the growth of the HII shock bubble around the star. The shock radius was computed in just the same way as before: probing the ionization fraction of the gas in our box along at points along a line connecting the center of the box with one edge and finding the radius at which the ionized fraction drops from $x \approx 1.0$ (fully ionized) to $x \approx 0$ (neutral). This transition has a sharp boundary and so we find the radius at which $x = 0.5$.

We notice a great deal more fluctuation in the shock radius, though it still grows steadily. Major drops in shock radius seem to correspond directly to changes in effective temperature and hence also ionizing flux, with the drop immediately following the discontinuous jump in ionizing flux. Despite this behaviour, the average radius as well as the shock front viewed in terms of gas density, is spherical and expanding steadily. This implies that the jumps in ionizing flux must be causing some kind of readjust within hot, rarefied gas inside the expanding sphere.

Closer examination reveals that waves traversing the interior of the shock are reflected off the shock boundary, carrying a small amount of material back into the cavity, which momentarily increases the column density toward the source. In these regions of higher column density, the gas recombines before begin reionized by the UV flux from the central source. These density waves interior to the cavity are not prominent in our protostellar simulation. It may be that the discontinuous jumps in luminosity or ionizing flux in the ZAMS model are launching these density waves. We are investigating whether removing the discontinuities also removes the density waves.

In Figure 4.5 we compare the structure of an HII region in the protostellar versus ZAMS model evolution. The irregular shape of the ZAMS model is the consequence of the action of density waves which are prominent in ZAMS models.

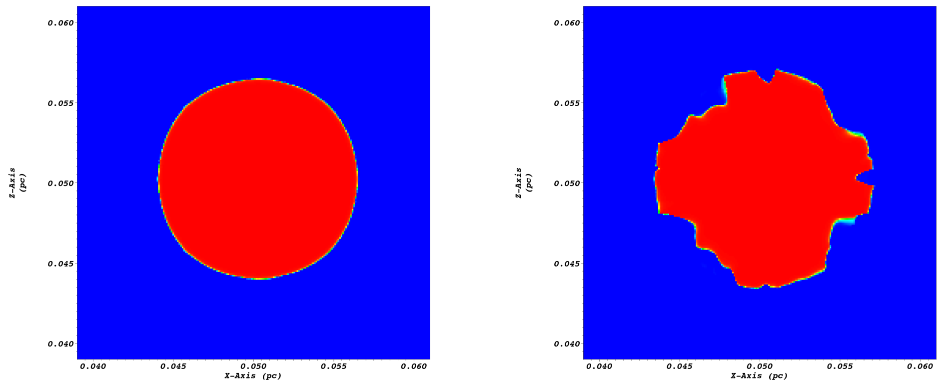

Figure 4.5: Shown in red is the fully ionized region surrounding a single star that is accreting at a constant rate of $10^{-3} M_{\odot}/\mathrm{yr}$. Blue indicates neutral gas. The star at the center of the red region in the right panel follows a ZAMS model, with its luminosity and effective temperature matched to one of 60 ZAMS values for stars ranging in mass between $0.1 M_{\odot}$ and $100 M_{\odot}$. Jumps in the ionizing flux cause the ionized gas to readjust before returning to a spherical shape. Grid effects appear exaggerated by the density waves introduced by the ZAMS model. The structure of the expanding shock is still spherical when viewed terms of the gas density profile. We chose a frame from our simulation when the fluctuations were particularly pronounced. In the left panel is seen the HII region around a star following our protostellar model. We chose a frame from the simulation where the HII region would be of comparable size to the one in the right panel. The ionized region remains spherical throughout the simulation.

There is another significant difference between the fluctuations observed in the ZAMS model, and the rapid collapse and rebuilding of the shock front in the protostellar model case (Figure 4.3). When using the self-consistent protostellar model, there was also a rapid change in effective temperature and hence ionizing flux. This occured during the transition to shell deuterium burning, where the radius of the protostar swells by a factor of ~ 2. The ionizing flux drops by several orders of magnitude and ionized region collapses. It is not a matter of the gas simply recombining due to the lack of ionizing photons. The sudden lack of pressure support causes the entire shock front to collapse and the gas to collapse inward. The entire HII region almost disappears briefly before being rebuilt.

4.4 Star formation and feedback in the cluster environment

We wanted to repeat simulations similar to Peters et al. (2010a), where a $1000M_\odot$ clump was allowed to collapse to a disk and begin forming massive stars in a central cluster. We wanted to see what difference protostellar modeling made to the overall evolution of the cluster. The most important consequence of the improved hybrid characteristics raytracing code employed by Peters et al. (2010a) was that it allowed for the realistic simulation of HII regions, with ionization, heating, and shadowing effects built in. One of the most important consequences of the protostellar model was that it tempered the ionization and heating in the early stages of star formation.

To study this effect, we simulated the cluster setup again, this time with our sink particles following the protostellar evolution model. We looked at two key effects: mean ionization in our simulation box, and mean gas temperature. Figure 4.6 shows these two measurements as functions of time in our simulation. Time is measured in units of global freefall time, or $t_{\rm ff} \approx 590,000$ years. In the "without protostellar model" case, sink particles follow a ZAMS model from the star, which means that they are hotter and more compact than true pre-main-sequence stars. This causes them to release more ionizing photons, compared to the protostellar case. The onset of ionization in the ZAMS case leads the protostellar case by about 0.03 freefall times, or about

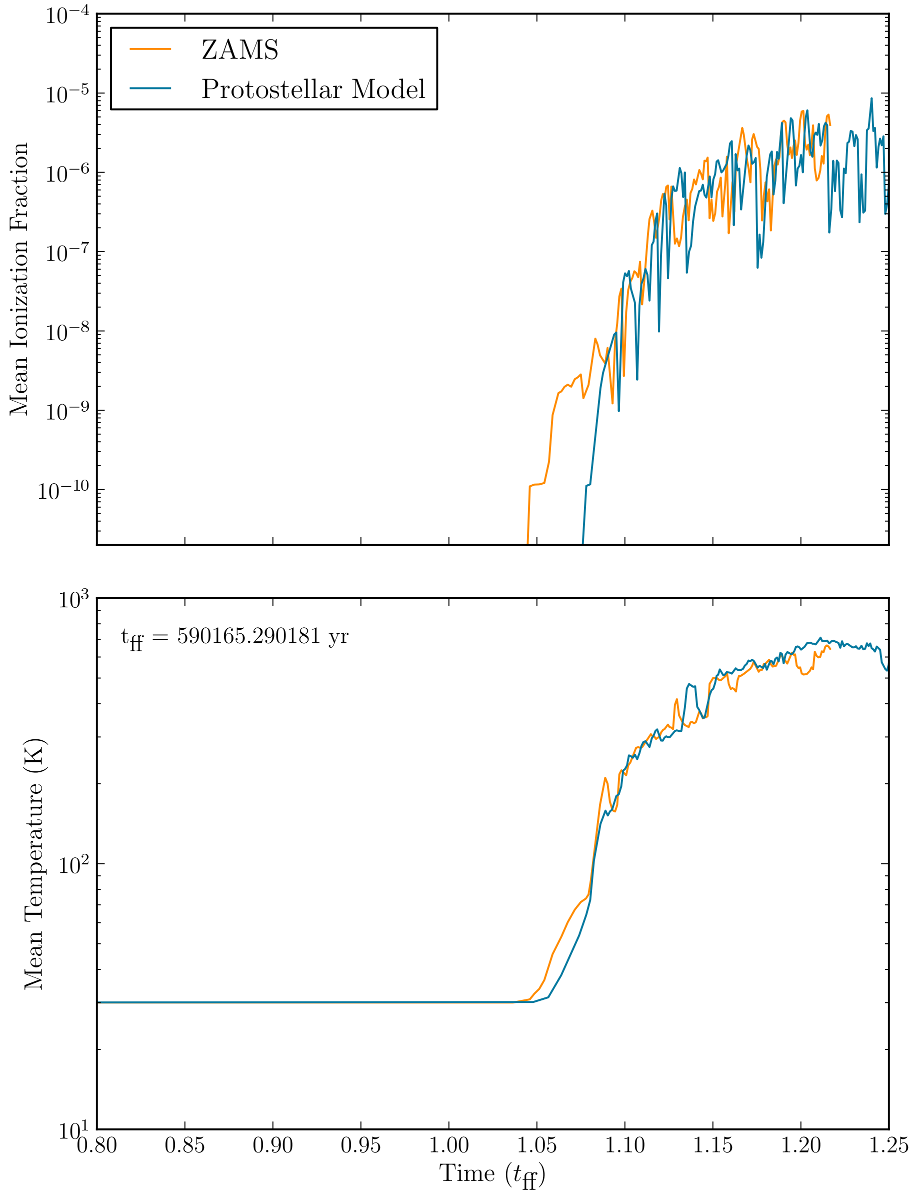

Figure 4.6: A comparison of the mean ionization fraction and mean temperature in cluster simulations with and without the protostellar evolution module engaged. In each case, the mean is calculated by finding the volume-weighted average. Values are only meaningful in a relative sense, as the simulation volume is large (side length ~ 3.8pc) and the most active region is the inner cubic parsec.

17.7 kyr. The onset of star formation in our simulations occurs at around 1 freefall time. After 1.1 freefall times, the largest star in either simulation is at $20M_\odot$ and dominates the UV output of the cluster, resulting in comparable mean ionization for both cases.

When we consider mean temperature instead of mean ionization, the leading effect by the ZAMS model is still there, only less pronounced. Major heating of the gas in the ZAMS case leads the protostellar case by close to 0.01 freefall times, or about 5.9 kyr. The first star to form in a cluster tends to grow to be among the largest stars in the cluster and dominate the heating and ionization. This suggests that accurate protostellar modeling is most important in the early stages of a cluster simulation, and for low-mass stars. Offner et al. (2009) showed that radiation even from low-mass stars has a significant effect on the gas heating and formation of brown dwarfs.

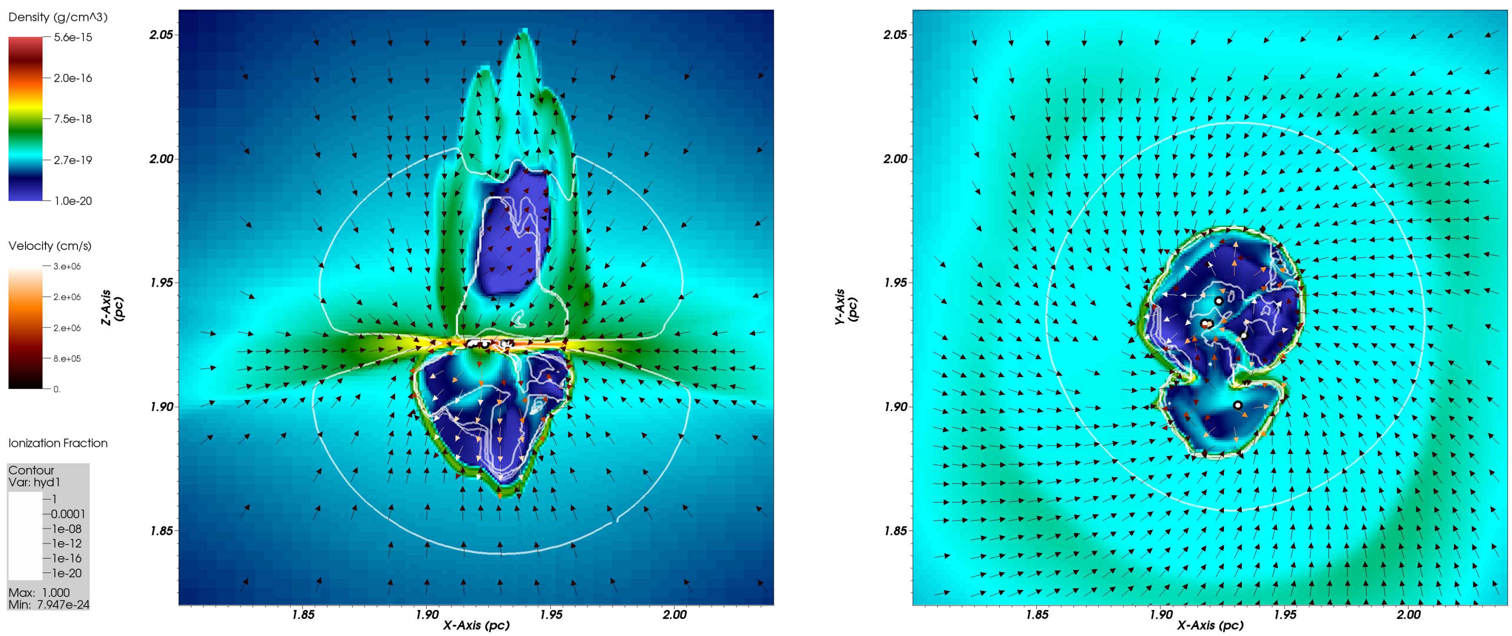

Figure 4.7: Results from the cluster simulation with the protostellar code showing the mass density. Shown here is the state of the simulation after 1.15 freefall times or about 0.68 Myr. The image on the left shows vertical slice through the center of the simulation box. The image on the right is of a horizontal slice 0.388 pc below the midplane, highlighting the cavity. Contours are of the ionization fraction, where 0 is completely neutral and 1 represents completely ionized. Successive contours show increases in ionization by four orders of magnitude at a time. Arrows indicate the direction and speed of the gas motion.

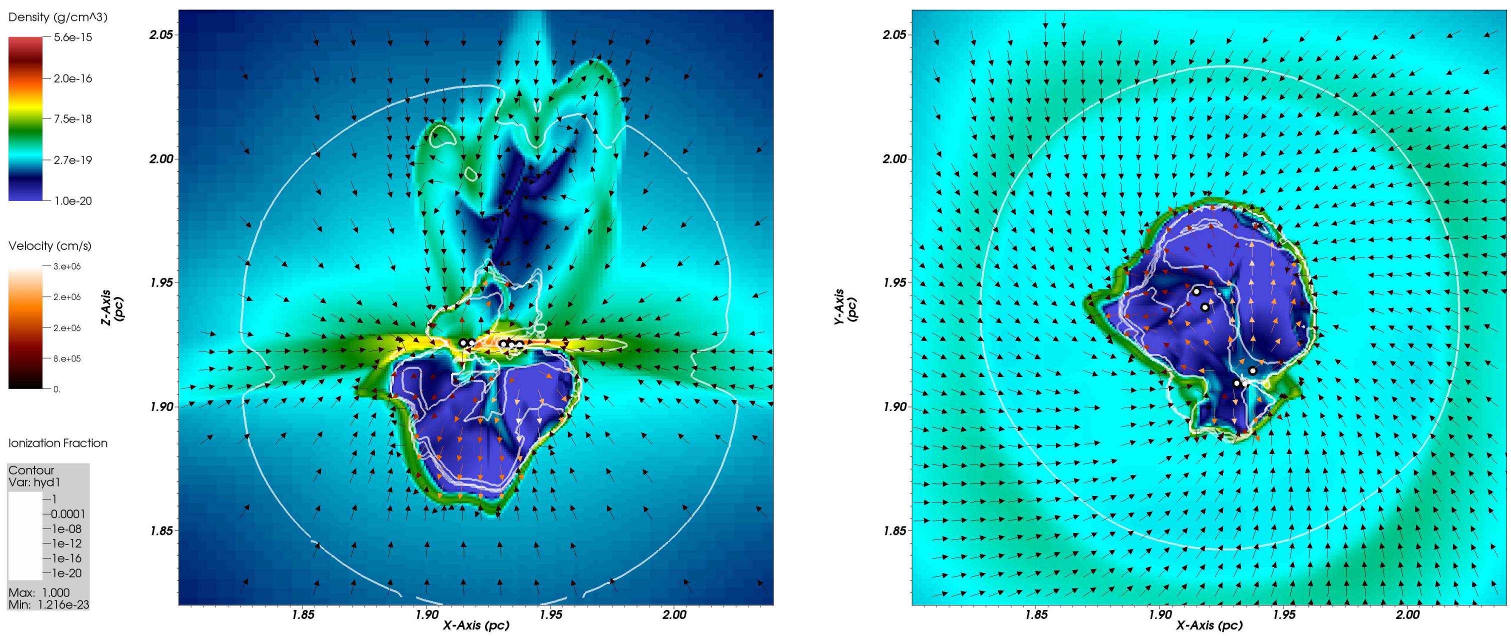

Figure 4.8: Results from the cluster simulation with a ZAMS model showing the mass density. Shown here is the state of the simulation after 1.15 freefall times or about 0.68 Myr. The image on the left shows vertical slice through the center of the simulation box. The image on the right is of a horizontal slice 0.388 pc below the midplane. Contours are of the ionization fraction, where 0 is completely neutral and 1 represents completely ionized. Successive contours show increases in ionization by four orders of magnitude at a time. Arrows indicate the direction and speed of the gas motion.

To get a visual sense of the gas dynamics and configuration of the cluster, we visualized the gas density by taking slices through our simulation box. Zoomed-in views of the cluster are shown in Figures 4.7 and 4.8. The simulation box is actually about 3.8 pc across. Here we show the central region—about 1/4 pc on a side. In each of these figures, the left image shows a vertical slice through the center of our simulation box, while the right image shows a horizontal slice 0.388 pc below the midplane, just below the disk, highlighting the cavity created by the radiation. Gas densities ranging from 10^{-20} to 5.6×10^{-15} g/cm^3 are shown in color. Overplotted on each of these figures are isocontours of ionization fraction. Successive contours indicate increases of four orders of magnitude in the local ionization fraction of the gas, ranging from $x \approx 0$ (neutral) to $x \approx 1$ (fully ionized). We also show the velocity field, with color indicating speed. The fastest-moving gas travels at close to 3×10^6 cm/s. We also see the gas largely moving into the cluster through the disk, as we'd expect. The hollowed-out HII regions, where the gas is largely ionized, expands upwards and outwards as a kind of fountain before falling back onto the disk.

Sink particles indicating the locations of stars are marked with black-rimmed white points. The side view shows the stars to be confined to the disk while the top-down shows the stars packed in a tight cluster. The separation between stars nowhere exceeds 0.1 pc.

These snapshots of the simulation were taken at around 1.15 freefall times in each case. At this stage, about 0.68 Myr have elapsed since the beginning of the simulation, with the onset of star formation having occurred around

0.6 Myr. At this stage, the protostellar case (Figure 4.7) and the ZAMS case (Figure 4.8) look similar in many ways: the stars are in a densely-packed cluster, and each cluster has produced an expanding HII region. However, in the ZAMS case, it appears that the reach of the ionizing radiation has gone further as indicated by the first, almost circular contour. It also appears that the HII region has been driven further upwards and outwards in the ZAMS case—perhaps because the cluster was initially hotter and more ionized than in the case where radiation was tempered by the protostellar model. It is difficult to say that this is true definitively because these HII regions do appear as fountains and their shapes are very transient and variable.

Peters et al. (2010a), in their cluster simulations, saw flickering of the HII regions on short timescales—that is, significant changes in the size and flux of HII regions. Animations of gas temperature and ionization revealed regions above and below the cluster that changed rapidly with time in cluster simulations both with and without the protostellar model in place. We thus confirmed that the flickering was not due to their choice of prestellar model. Synthetic observations produced by Galván-Madrid et al. (2011) of the original Peters et al. (2010a) results showed these this flickering visible in radio-continuum emission and in agreement with available observations.

4.4.1 Accretion Histories

One of the first things we sought to investigate with our protostellar code was the accretion histories of our sink particles. Peters et al. (2010a) showed that the gas surrounding the center of the cluster would fragment and result

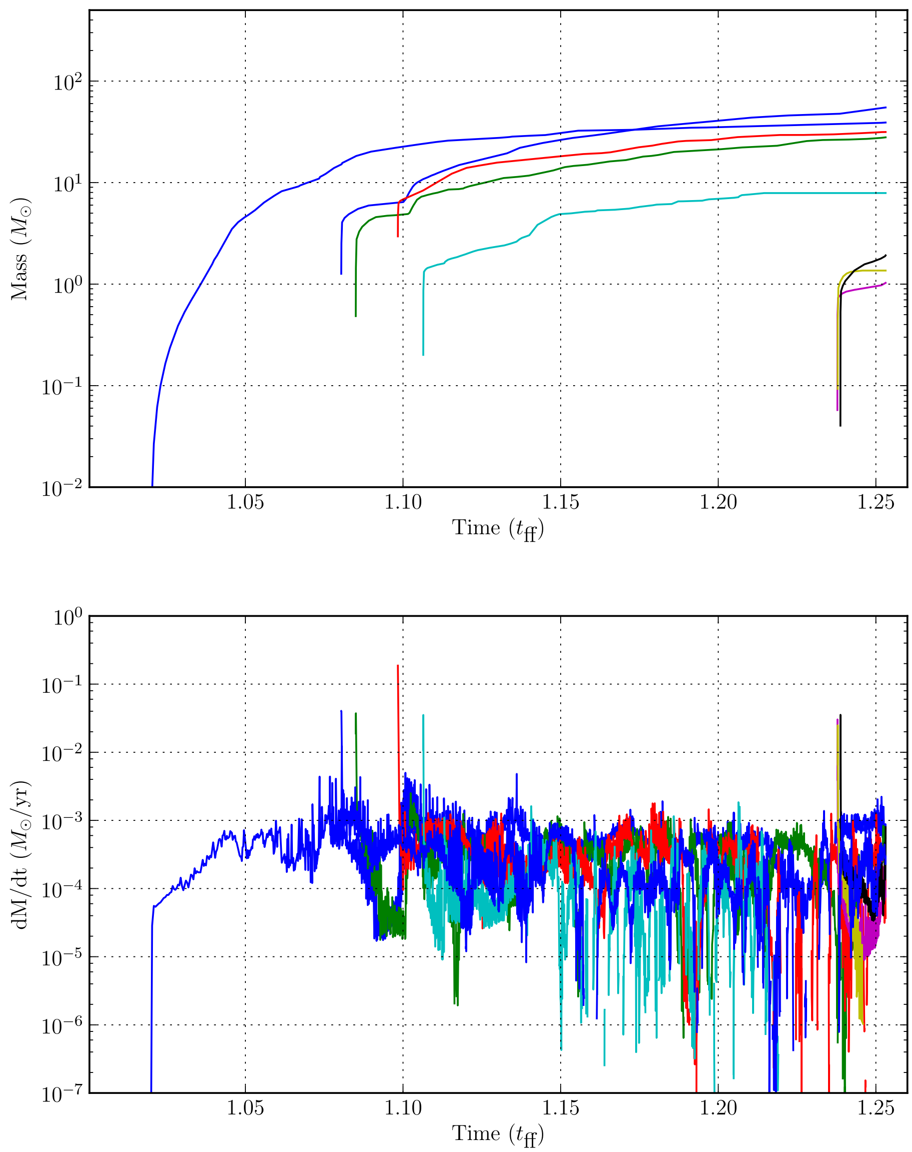

Figure 4.9: Accretion histories of stars formed in cluster setup including protostellar evolution. The upper panel shows the mass of each particle as a function of time. The lower panel shows the accretion rate in units of $M_\odot$ yr^{-1} as a function of time. The dynamical time is about 0.59 Myr.

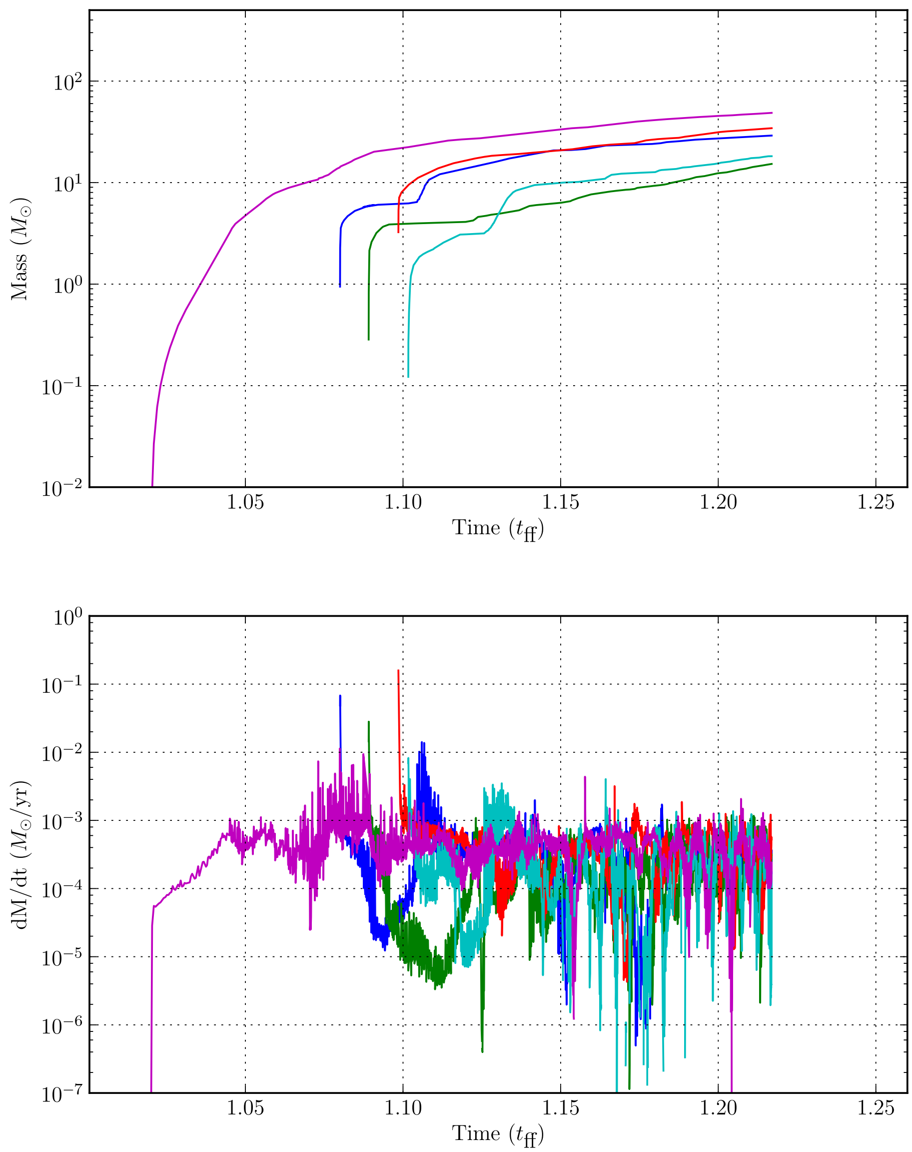

Figure 4.10: Accretion histories of stars formed in cluster setup with sink particles following a ZAMS model. The upper panel shows the mass of each particle as a function of time. The lower panel shows the accretion rate in units of $M_\odot$ yr^{-1} as a function fo time. The dynamical time is about 0.59 Myr.

in a highly variable accretion rate. We see this in Figures 4.9 and 4.10, where we show in the two panels the accretion histories of every sink particle formed in our simulation along with their accretion rates.

In the lower panel we see the accretion rate of each star, and for most of the stars in our simulation, the accretion rate remains between 10^{-4} and $10^{-3} M_{\odot}/\mathrm{yr}$, although with significant fluctuation between the extremes of $0.1 M_{\odot}/\mathrm{yr}$ (briefly) and $10^{-7} M_{\odot}/\mathrm{yr}$.

The upper panel in Figure 4.9 shows the growing masses of each of the stars in our simulation. Star formation does not really commence until after the first dynamical time (freefall time)—about 0.59 Myr for our simulation setup. There seems to be a burst of star formation after $t \approx 1.10 t_{\mathrm{ff}}$, and then another later burst of formation around $t \approx 1.24 t_{\mathrm{ff}}$. Interestingly, the most massive star is not the first star in our simulation, but it is overtaken in mass by the second star, which reaches a final mass of about $54.9 M_{\odot}$. The others reach final masses of approximately 39.1, 31.5, 27.9, 7.9, 1.9, 1.3, and 1.0 $M_{\odot}$. The average mass of these 8 stars is 20.7 $M_{\odot}$.

In the ZAMS case, shown in Figure 4.10, the final masses of the stars are 48.6, 34.4, 29.0, 18.2, and 15.3 $M_{\odot}$. The average mass of these 5 stars is 29.1 $M_{\odot}$. It is difficult to draw firm conclusions about the impact of a protostellar model on the population dynamics of a cluster. We would need to complete longer simulations under more realistic initial conditions (including turbulence). The "protostellar" run experienced a second wave of star formation and had a lower average mass per star. However, if we do not include the second wave of star formation, the average mass per star is approximately

$32.3 M_{\odot}$, slightly higher than in the "ZAMS" run. We were able to run the protostellar simulation a little longer than the ZAMS simulation; the second wave of star formation only appeared very late in the protostellar simulation. The ZAMS run may have formed more stars if run for longer. We ran each setup for approximately two weeks on 64 processors, or approximately 21,500 CPU-hours. The protostellar simulation actually progressed further than the ZAMS simulation, likely due to the fact that the radiation field is weaker for pre-main-sequence stars. In either case, memory or computational constraints limited the length of the runs.

4.4.2 Mass-radius relation

The mass-radius relation for a star is a means of comparing different protostellar models. It is also a way of seeing the evolution of the stars in our simulation. As stars accrete mass or undergo nuclear-structural changes in their interiors, the radius reacts either by expanding or contracting. We see the evolution of the stars in our simulation represented in Figure 4.11. In this figure we compare the radii of stars from our different cluster simulations. In the cluster simulations of Peters et al. (2010a), the stellar radius was computed by checking a lookup table of ZAMS-values. The table contained the masses, luminosities, and effective temperatures of zero-age main-sequence stars. From this, the radius is easily computed:

$$R_* = \left(\frac{L_{\mathrm{int}}}{4\pi\sigma T_{\mathrm{eff}}^4} \right)^{1/2} \tag{4.6}$$

Because stars are assigned to a matching table entry, the mass-radius relation for stars in the ZAMS will appear jagged unless some interpolation within the table is applied.

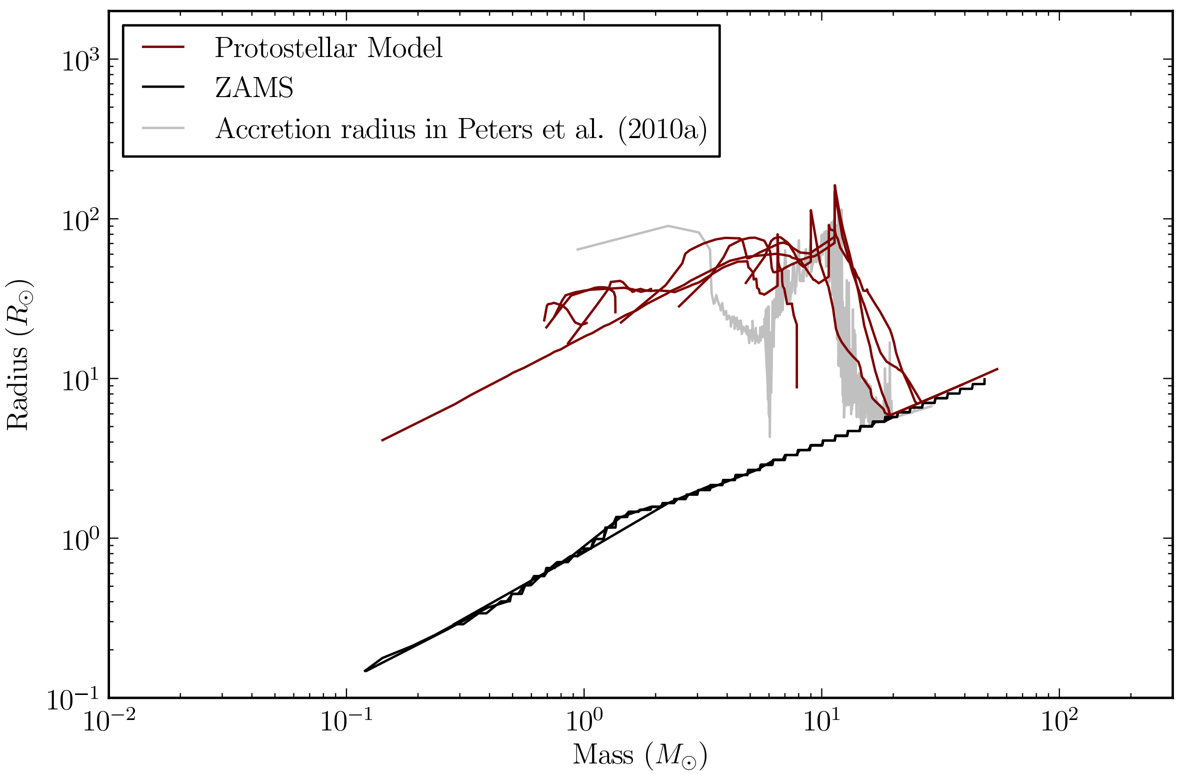

Figure 4.11: The mass-radius relation for the stars in both cluster simulations. The black lines mark the stellar radius tracks of the sink particles in the ZAMS simulation. The radius is solved for by consulted a table of luminosities and temperatures for ZAMS stars of different masses. The grey line indicates the separately-calculated accretion radius. Red lines mark the tracks of sink particles following the protostellar model. This radius is used as both the stellar radius and the accretion radius.

The stellar radius and effective temperature are used to compute the flux of ionizing photons by the raytracing code. To compute gas heating, the raytracing code also includes the effects of accretion luminosity. An accretion radius is calculated separately in the ZAMS runs by interpolating to the precomputed tracks of Hosokawa & Omukai (2009). The problem with this approach is that it is not self-consistent. With a rapidly-fluctuating accretion rate, an interpolation between separate tracks from Hosokawa & Omukai (2009) results in a rapidly-fluctuating accretion radius. We show the accretion radius for a single star in the ZAMS run by the grey line in Figure 4.11.

The red lines in this figure are the stars following a protostellar evolution model that we described earlier in this paper. These stars have their radius continuously evolved according to their burning state and the accretion of new material. The radius, therefore, does not fluctuate with unrealistic rapidity. Because the model is a self-consistent description of the radius, we use the same quantity to describe the stellar radius and the accretion radius, rather than computing each by different means. Protostars have radii an order of magnitude larger than a zero-age main-sequence star of equal mass. Hence, their effective temperatures and flux of ionizing photons are going to be much less (for a $1 M_\odot$ star, 3000K vs. 5000K in effective temperature, 10^{29} s^{-1} vs 10^{39} s^{-1} in ionizing photons). Simulations without protostellar modeling may be excessively heating or ionizing the gas during the early phases of star formation.

The evolution of the stars in each simulation is also told by the mass-luminosity relation, shown in Figure 4.12. Black and grey lines belong to the

ZAMS simulation, dark and pale reds to the protostellar simulation. Accretion luminosity, calculated as $L_{\rm acc} = GM\dot{M}/R_{\rm acc}$, is especially sensitive to the accretion rate $\dot{M}$ and the accretion radius $R_{\rm acc}$. Stars in the ZAMS simulation show accretion luminosities that are up to an order of magnitude larger than the stars in the protostellar simulation on account of the difference in stellar radius. Only for stars larger than about $20 M_\odot$ do the differences between the two models disappear. The black jagged line indicates a main sequence luminosities from a precomputed table, which tends to underestimate stellar luminosities for protostars less than about $2 M_\odot$. Protostellar luminosities are indicated by dark red lines and protostellar accretion luminosities by pale red lines. Much of the rapid fluctuation in the accretion luminosities of both simulations stems from the high variable mass accretion rate (see Figures 4.9 and 4.10).

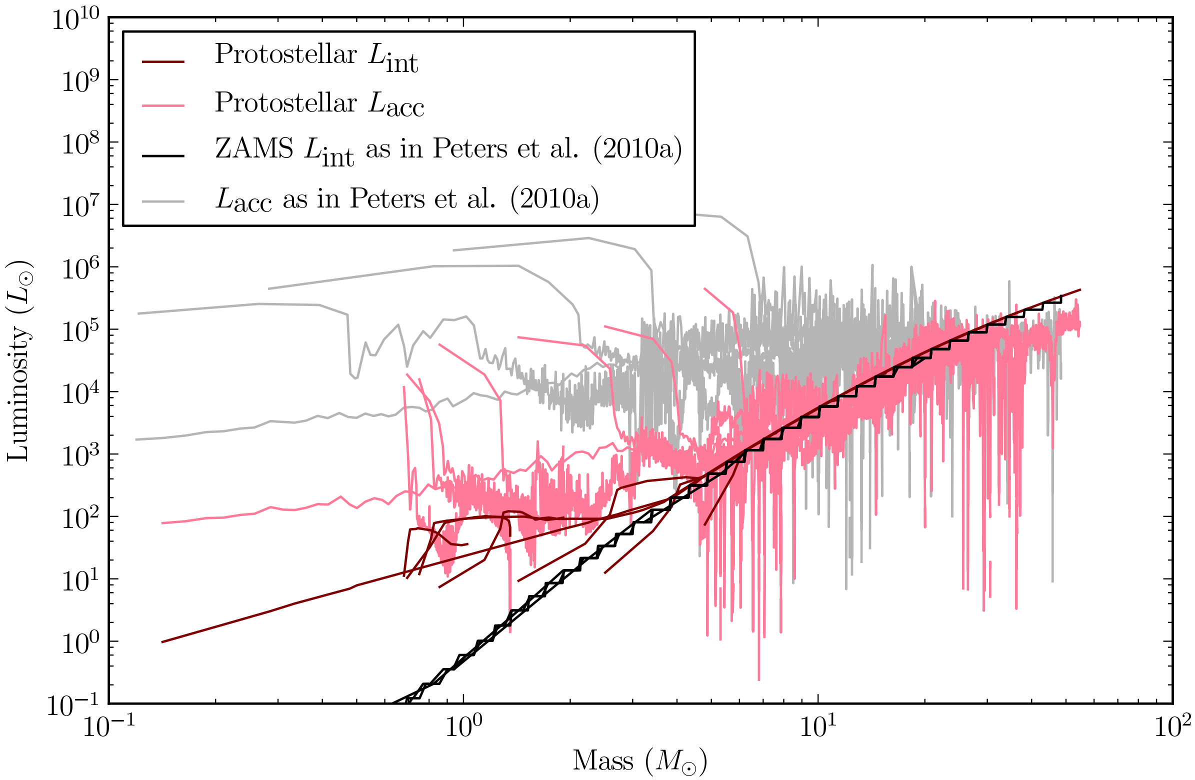

Figure 4.12: The mass-luminosity relation for the stars in both cluster simulations. The black lines mark the stellar luminosity tracks of the sink particles in the ZAMS simulation. A matching luminosity is culled from a table of ZAMS values. Grey lines indicates the accretion luminosities of these stars. Dark red lines mark the tracks of sink particles following the protostellar model. Pale red lines are the accretion luminosities of sink particles in the protostellar simulation.

4.4.3 Cluster mass spectrum

We wanted to see if the different heating and ionization present when implementing a protostellar model would also alter the global gas mass distribution. In Figure 4.13 we show the evolution of the distribution of mass by density in our cluster simulations, with the protostellar run shown on the left and the ZAMS-based run on the right. We show the mass distribution at four stages in the simulation: at $t = 1.05$, 1.10, 1.15, and 1.20 $t_{\rm ff}$, where one freefall time is approximately 0.59 Myr. The figure shows the distribution of all the mass in our simulation box—or, about 1000 $M_\odot$. The earliest time represents the onset of star formation in our simulation and $t = 1.2t_{\rm ff}$ represents the time at which the first stars are reaching the main sequence in our protostellar simulation.

When we compare the two runs, the effect of the protostellar model on the mass density spectrum appears minimal. Most of the high density gas is in the disk (see Figure 4.7), closest to the star cluster. The initial, spherically-symmetric density profile is one of a flat top in the center and an $r^{-3/2}$ profile farther out (see Figure 4.2).

4.4.4 Ionization and Temperature

Protostars have large radii about an order of magnitude larger than equivalent-mass main-sequence stars. They may be just as luminous, and they certainly have high accretion luminosities, but it is the effective temperatures of their surfaces that determine how great the flux of ionizing photons will be, if the star emits any at all. The single greatest difference we saw when simulating

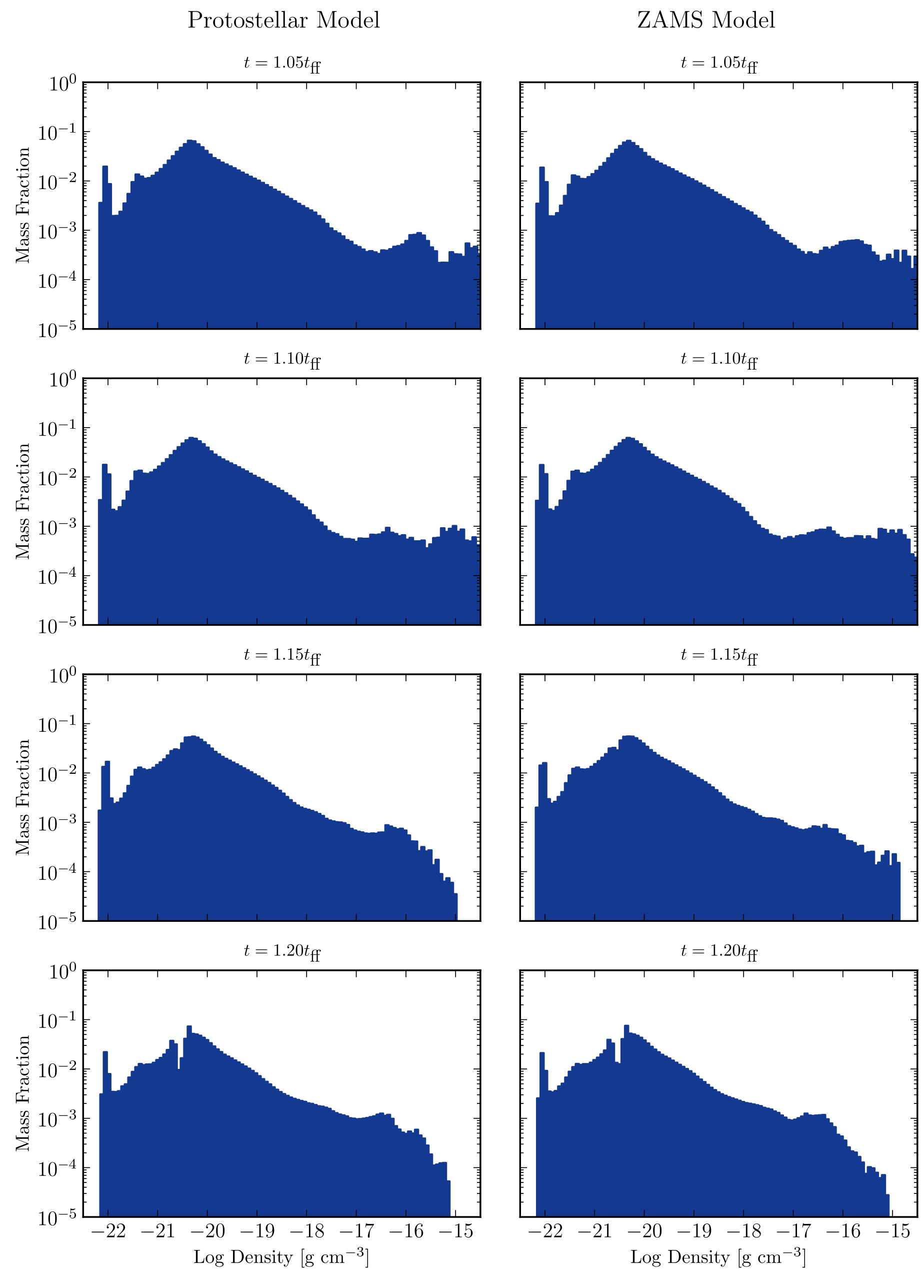

Figure 4.13: Evolution of the mass density spectrum in each cluster setup, with the protostellar run on the left and ZAMS-based run on the right. The mass-weighted gas density spectrum at four distinct times is shown: 1.05, 1.10, 1.15, and 1.20 $t_{\rm ff}$. One freefall time is approximately 0.59 Myr

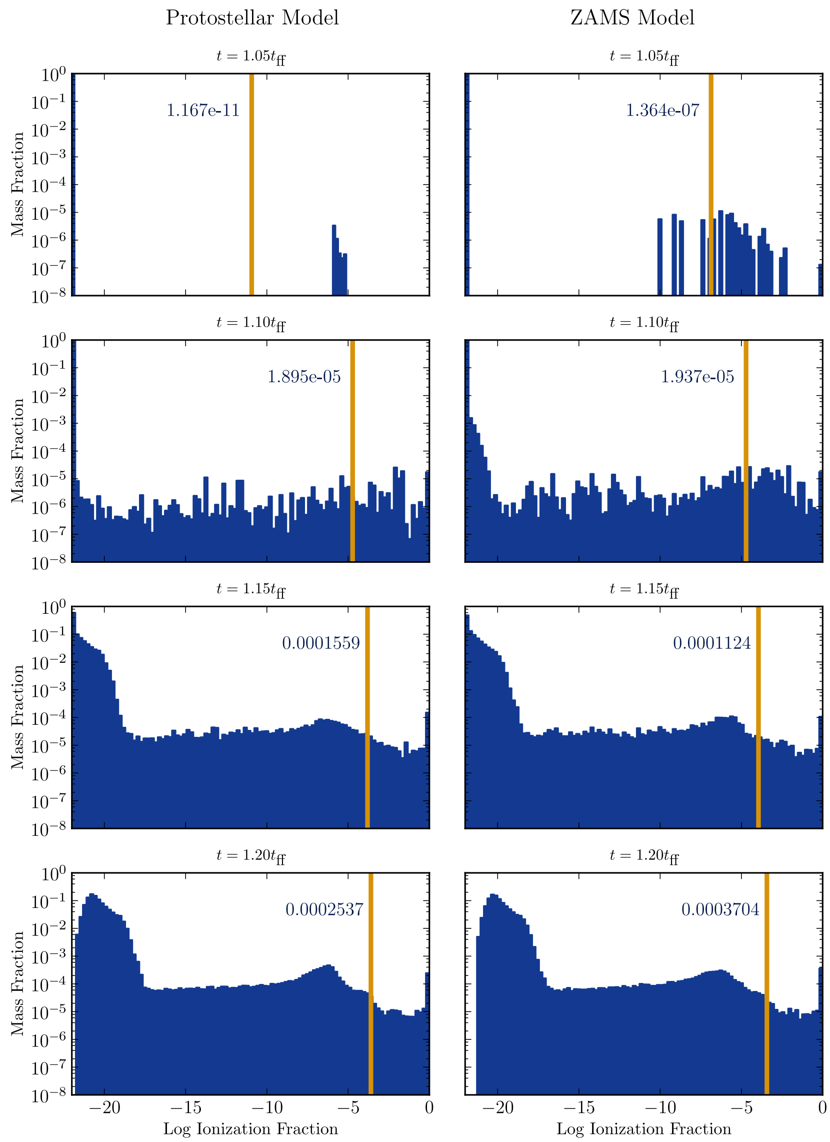

Figure 4.14: The evolving mass-weighted ionization fraction spectrum. Compared are cluster simulations with stars running on the protostellar evolution model (left) and on a ZAMS model (right). A distribution of the total mass in the simulation box (about 1000 $M_\odot$) is shown for $t = 1.05, 1.10, 1.15, 1.20\, t_{\rm ff}$. One freefall time is approximately 0.59 Myr. The yellow line indicates the mass-weighted average, the value of which is printed in blue to the left of the line.

the evolution of a star cluster with self-consistent protostellar modeling was that when the first stars began to form after about a dynamical time, the average gas temperature and average ionization of the gas was considerably less in the simuation involving our protostellar model (Figure 4.6).

Figure 4.14 shows the mass-weighted spectrum of the ionization fraction in both cases, with the protostellar model on the left and the ZAMS model on the right. Values for ionization fraction range from very close to 0 (completely neutral) to approximately 1 (completely ionized). The figure shows the spectrum for all the gas involved in the simulation—approximately 1000 $M_\odot$ in total. The thick yellow line indicates the mass-weighted average value for the ionization fraction with the value printed beside the line. Individual snapshots in time are as previously: $t = 1.05, 1.10, 1.15, 1.20\, t_{\mathrm{ff}}$.

It was important to show how the averages changed over time in Figure 4.6 because of how the mean tended to fluctuate yet the two models had similar values for all but the earliest phases of star formation. The early phase is shown in the first row, at $t = 1.05 t_{\mathrm{ff}}$. Here there is a significant difference in the mean ionization fractions of the two models. The low-mass ZAMS stars are hotter and have smaller radii. There is greater early ionization seen in this case.

At later stages, the distributions appear more similar as the conspicuous effects of the model disappear. The second row of panels shows the ZAMS stars, initially brighter and hotter, begin ionizing more hydrogen around a Log ionization fraction of -20.

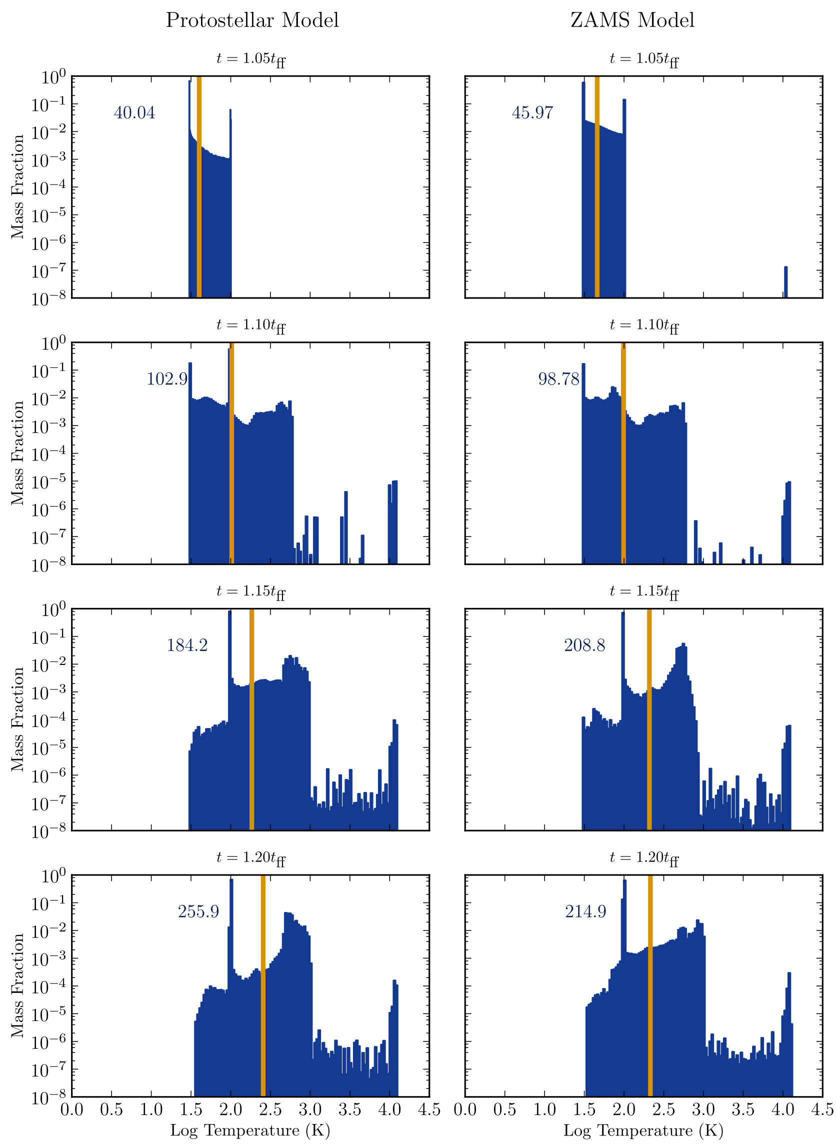

Figure 4.15: The evolving mass-weighted temperature spectrum. Compared are cluster simulations with stars running on the protostellar evolution model (left) and on a ZAMS model (right). A distribution of the total mass in the simulation box (about 1000 $M_\odot$) is shown for $t = 1.05, 1.10, 1.15, 1.20\,t_{\rm ff}$. One freefall time is approximately 0.59 Myr. The yellow line indicates the mass-weighted average, the value of which is printed in blue to the left of the line.

The temperature tells a similar story. Figure 4.15 shows the mass-weighed temperature spectrum of the gas in the simulation volume at the same stages in time. The spike seen at 10^2 K is the cooler gas surrounding the cluster. The gas at 10^4 K is the hot, ionized gas inside the HII region formed by the star cluster. We see some initial heating by the first stars in the ZAMS run, then a shifting in both simulations of greater gas mass towards higher temperature.

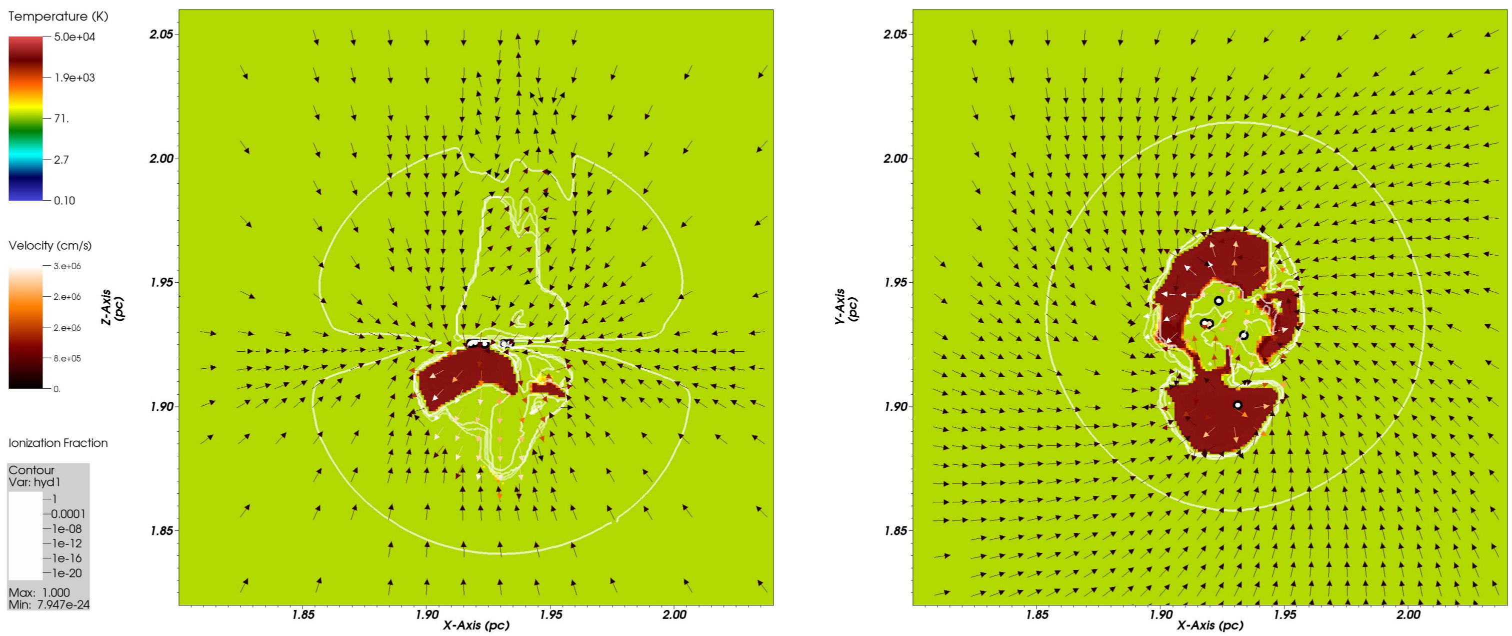

Figure 4.16: Results from the cluster simulation with the protostellar code showing the gas temperature. Shown here is the state of the simulation after 1.15 freefall times or about 0.68 Myr. The image on the left shows vertical slice through the center of the simulation box. The image on the right is of a horizontal slice at the midplane. Contours are of the ionization fraction, where 0 is completely neutral and 1 represents completely ionized. Successive contours show increases in ionization by four orders of magnitude at a time. Arrows indicate the direction and speed of the gas motion. Much of the gas is at uniform temperature ($\sim$ 100 K). Although the radiation field drops off with distance, so does the gas density and is thus less efficient at cooling.

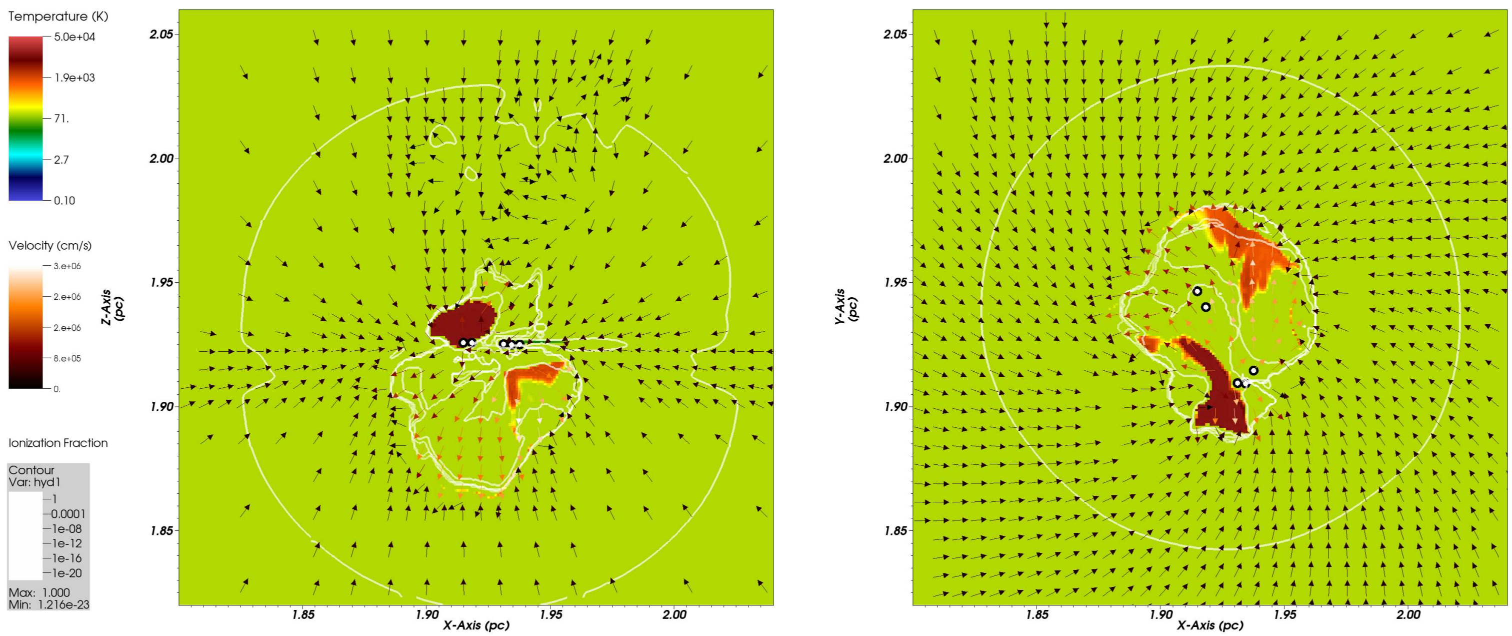

Figure 4.17: Results from the cluster simulation with a ZAMS model showing the gas temperature. Shown here is the state of the simulation after 1.15 freefall times or about 0.68 Myr. The image on the left shows vertical slice through the center of the simulation box. The image on the right is of a horizontal slice at the midplane. Contours are of the ionization fraction, where 0 is completely neutral and 1 represents completely ionized. Successive contours show increases in ionization by four orders of magnitude at a time. Arrows indicate the direction and speed of the gas motion. Much of the gas is at uniform temperature ($\sim$ 100 K). Although the radiation field drops off with distance, so does the gas density and is thus less efficient at cooling.

The temperature structure of the gas surrounding the cluster is shown in Figures 4.16 and 4.17. These figures reveal some interesting features. The gas surrounding the cluster is approximately 100 K. This results from the competing processes of heating and cooling. At increasing distances from the cluster, falling particle densities mean less efficient cooling. But the radiation field is falling off as r^{-2} as well. The competing processes result in a large region of even-temperature gas surrounding the cluster. Far away from the cluster, a cooler disk and a hot corona is also seen for the same reasons.

In these figures, we also see pockets of very hot 10^4 K gas that seems to follow the regions of ionized gas. When we study the evolution of these regions in time, we see that these pockets of high-temperature gas are very transient: forming, expanding, breaking apart, and cooling very rapidly. They are due to photoionization and photoionization heating caused by the massive stars in the cluster. Peters et al. (2010a) attributed this flickering to the chaotic gas motions in the cluster. Gas moving inwards through the disk is gravitationally unstable and fragments of gas at different densities will absorb the ionizing flux from stars allowing the gas in the newly-shadowed region to cool, resulting in the appearance of flickering.

Figure 4.18 shows what is meant by "flickering". We see in our simulations of clustered star formation pockets of gas rapidly ionizing and then neutralizing. The frames in this figure show a vertical slice through the simulation box and regions marked in bright red show the fully ionized hydrogen ($x = 1$), while other colors indicate gas of which only a small fraction is ionized ($x \ll 1$). Between frames the simulation advances about 1200 years.

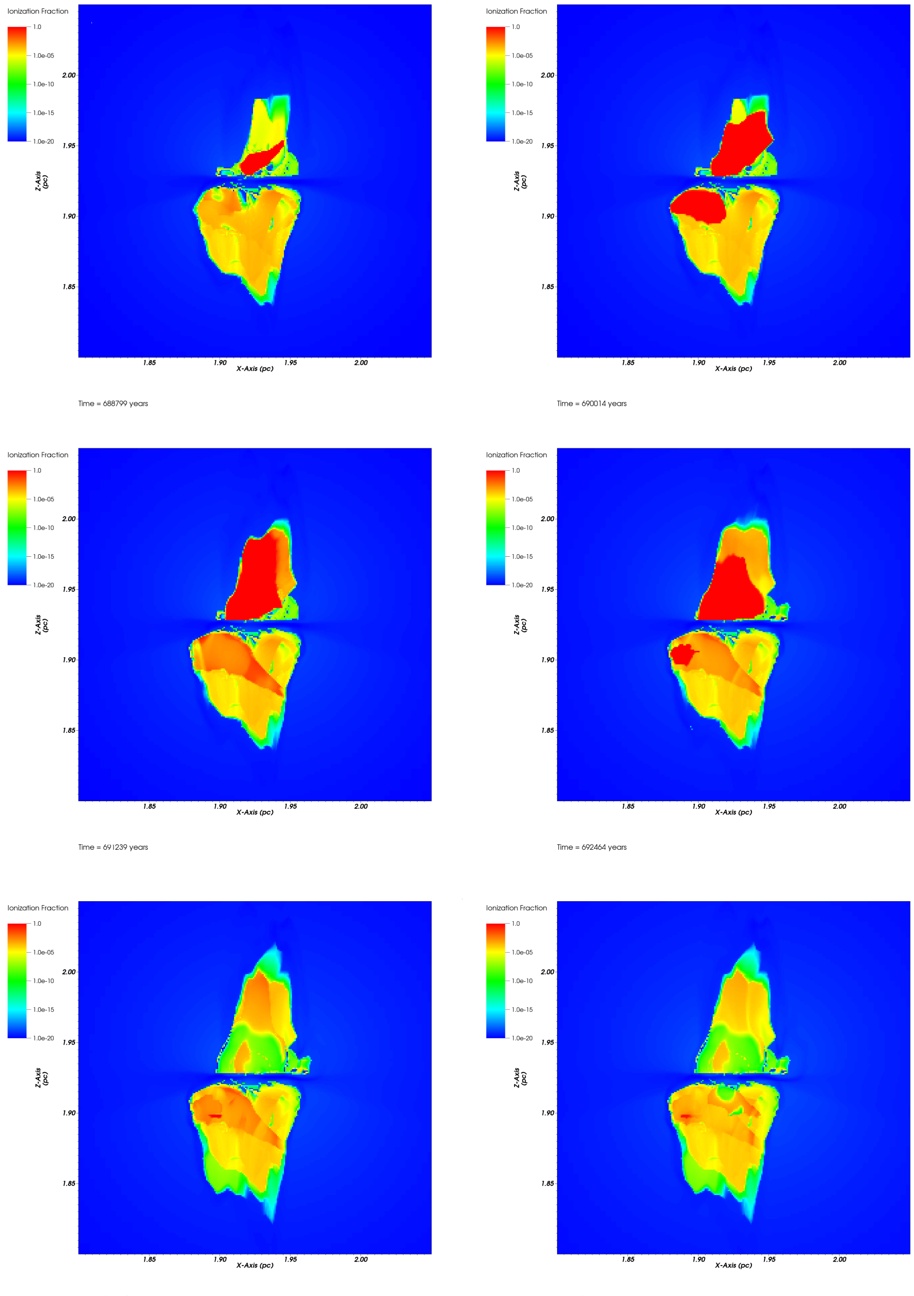

Figure 4.18: Results from the cluster simulation with a protostellar model showing the ionization fraction. Shown is a vertical slice through the center of the simulation box. Gas marked in bright red indicates fully ionized gas ($x = 1.0$). Since the colouring followes a logarithmic scale in ionization fraction, all other colors indicate gas that is only very slightly ionized. The order of the panels is from left-to-right, row-by-row. The time between frames is about 1200 years. These frames show rapid ionization and recombination in different regions.

4.5 Discussion

Our model simulations include a number of limitations that should be noted. They neglect the effects of radiation pressure. On large scales, radiation pressure from stellar clusters could drive galactic winds (Murray et al., 2011). However, within our $1000 M_{\odot}$ cluster, radiation pressure below the Eddington limit should not be dynamically significant (Yorke & Sonnhalter, 2002; Krumholz et al., 2007a).

The raytracing radiative feedback method we employ has the advantage of handling direct ionizing and nonionizing radiation well, allowing us to trace gas heating and ionization. We must, however, for reasons of computational tractability neglect all treatment of ray scattering. Apart from prescriptions for dust cooling, we also neglect reemission of radiation by dust. Dust does not reintroduce new rays into our computational grid. These approximations should be fair since stars represent the dominant sources of radiation in cluster. Reemission of radiation by dust has the effect of reddening the radiation spectrum, which we do not account for.

In our simulations, we treated gas that was initially cold and in solid body rotation, but without any turbulence. Molecular clouds are observed to have supersonic turbulence, and a more realistic set of initial conditions would include turbulence. However, this might have obscured the effects of our protostellar model that we were seeking to measure. We are currently preparing to run simulations that include realistic turbulent initial conditions as well magnetic fields, which were also left out of this simulation.

The protostellar model we've added to our simulations improves on previous work by adjusting the ionizing luminosity so that it matches the stellar surface effective temperatures for accreting protostars, which initially have radii larger than equal-mass stars on the main sequence. We note, however, that a full-spectrum treatment of the radiation still faces technical and computational limits that make the problem extremely challenging. As a compromise, we break the radiation into its ionizing and nonionizing components.

The single accreting protostar simulations showed that when the star undergoes its transition to shell deuterium burning, with its associated swelling of the stellar radius, the surrounding HII region collapses as the flux of ionizing photons is briefly, but greatly, diminished. This is a significant result. It implies that if the sudden collapse of an ultracompact HII region around a young stellar object could be observed, then it could mean directly observing a transition in the star itself. Changes in HII regions may indicate changes in the stars themselves. It was hard to see same phenomenon in the cluster simulations, however. There was flickering, and there were rapid changes in the size and shape of the bubbles surrounding the cluster, but discriminating between stellar evolutionary changes and the tumultuous motion of gas fragments around the cluster as the causes of these phenomena was very difficult. It may require greatly increased spatial or temporal resolution, which would make the problem computationally intractable.

If such an object could be observed in nature, it would likely reside in or near a cluster. It would be a massive star of perhaps $10 M_{\odot}$ or more and would be surrounded by an extremely small HII region ($\lesssim 0.001$ pc). We calculated effective temperatures of about 8000 K precollapse and about 5000–6000 K at collapse. Our predicted luminosity would be around $10^4 L_\odot$, but the accretion luminosity would obviously depend on the accretion rate. Judging by the stellar structure calculations of Hosokawa & Omukai (2009), the swelling of the stellar radius should happen over the course of several kyr. If the lifespan of a typical HII region is $\sim 10^5$ yr, then we would expect a few HII regions out of every hundred to be in this collapse stage. A caveat, however: protostars in our simulation have their radii increased instantaneously by a factor of 2.1 during the transition to radiative interior structure with shell deuterium burning. More realistically, the swelling of the radius is fast ($\sim 10^3$ years), but not instantaneous.

4.6 Conclusions

Our results show that the early stages in the lifetime of a pre-main-sequence star can have an important effect on the clusters in which they are born. Before they even begin to burn deuterium, young protostars have a radii an order of magnitude larger than main sequence stars of equal mass. They heat the gas around them mainly by their accretion luminosities. ZAMS models overestimate the heating and ionization during this stage.

The effective temperature of a protostar accreting at a steady rate of $10^{-3} M_\odot$ yr^{-1} will be 3000K for about the first 0.2 dynamical times, then increases linearly with time over another 0.4 dynamical times to about 7000K, at which point the protostar has grown to just over $10 M_\odot$. In the ZAMS approximation, the protostar quickly heats to over 10^4K within 0.2 freefall times, and its temperature continues to rise as more mass is accreted, despite it being technically too young to have reached the main sequence.

As many protostellar models show, when protostars transition to a radiative structure in their cores, their radius swells suddenly by a factor of about 2 or greater. The swelling happens quickly—over the course of potentially just a few thousand years. During this time the effective temperature of the stellar surface drops rapidly, and consequently the flux of ionizing photons can drop by 3 orders of magnitude. Since this flux was sustaining an expanding HII region, the region collapses over the same timeframe as the medium neutralizes and cools. In our simulation of a star accreting at $10^{-3} M_{\odot}/\text{yr}$, the young HII region collapses from ~ 300 AU to ~ 50 AU. Simulations using ZAMS models do not see this effect.

The collapsed HII region is very poorly resolved in our simulations: only ~ 4 grid cells across. Further simulations at higher spatial and temporal resolution are required to study the way the gas reacts to the rapid changes that occur when the star transitions to a radiative interior structure. Observationally, a collapsed HII region might be identified by weak radio continuum emission surrounding a source that should be massive enough and luminous enough to drive a hypercompact HII region. We estimate the frequency of these collapsed HII regions around isolated pre-main-sequence stars to be at most a few percent.

In stellar cluster simulations with the protostellar model, heating and ionization is delayed for the same reasons as before, but as the cluster ultimately comes to be dominated by its most massive stars at later times, the protostellar model has a lesser effect. In our simulations of a $1000 M_{\odot}$ cloud of molecular hydrogen at 30 K, major ionization of the gas in the protostellar modeling case lagged the ZAMS case by about 3% of a freefall time, or about 17.7 kyr. Major heating of the gas in the protostellar case lagged the ZAMS case by about 1% of a freefall time, or about 5.9 kyr.

Star formation begins after the simulation has progressed about a freefall time, and major differences in terms of heating or ionization between the two model cases have vanished by about 1.1 freefall times. This is because in either case, at least one massive star ($> 10 M_{\odot}$) has formed and its radiation has come to dominate over the effects of low-mass protostars.

The cluster simulation including the protostellar model formed 4 stars with masses less than $10 M_{\odot}$, while in the ZAMS simulation all stars grew to be over $10 M_{\odot}$.

With flickering of the ionized regions visible in our new cluster simulations including protostellar evolution, we confirm and strengthen the results of Peters et al. (2010a) and Galván-Madrid et al. (2011), showing that the flickering is not an artifact of the selected prestellar model. Rather, the flickering results from chaotic gas motions around a cluster of massive stars. Future work will include analyses of synthetic observations of the radio-continuum emission from clusters of pre-main-sequence stars.

No flickering was seen in the single accreting star simulation, which confirms that it is an effect of the chaotic gas motions in the cluster environment.

Future simulations will have initial conditions including turbulence to model molecular clouds as realistically as possible. The stars will no longer be forming within a global disk, but rather along sheets and filaments in diverse parts of the cloud. With star formation thus spread out more in space and time, we expect the influence of individual young stellar objects on their environments to be more significant than when all stars form in a central cluster. It will be important to have the radiative feedback accurately modeled in these cases.

4.6.1 Acknowledgements

We thank Mark Krumholz for clarifying some of the more technical aspects of the protostellar evolution method, and also Takashi Hosokawa for sharing data from Hosokawa & Omukai (2009) with us.

Chapter 5

Conclusion

The addition of hybrid characteristics raytracing and one-zone modeling of pre-main-sequence stars to the FLASH framework represents an important achievement in simulating the formation of stars in the cluster environment. There are many diverse physics that need to be considered in such conditions. When faced with technical or computational limitations, knowing which physics must be included and which can be safely ignored is essential. To understand the complex nature of star formation, we must be able to gauge the importance of each process.

The history of computational star formation has been the unfolding of each piece of this puzzle in keeping with better and better observations. The Herschel Space Telescope is giving us new insights into molecular clouds, revealing their structure and identifying filaments as the key sites for star formation. When completed, ALMA will provide unprecedented resolution at submillimeter and millimeter wavelengths. This will allow for the imaging of the gravitational collapse of gas onto the accretion disks of young stars, as well as trace the magnetic field structure around stars. With an angular resolution of 0.1 arcsec, protoplanetary disks of young Sun-like stars will have their gas kinematics imaged clearly at distances up to 140 pc. ALMA will resolve 15 AU scales at Taurus molecular cloud distances, providing the exciting possibility of seeing collapsed HII regions in other, larger GMCs.

A protostellar model has enabled us to track the pre-main-sequence lifetimes of stars and gauge their radiative feedback. We found the ionizing luminosity to be much less than stars modeled as main-sequence equivalents. A $2M_\odot$ main sequence star releases as many ionizing photons ($\sim 10^{42}$ s^{-1}) as a $10M_\odot$ protostar that has been accreting mass at a steady rate of $10^{-3}M_\odot$/yr. Young protostars have radii that are an order of magnitude larger than a main sequence star of equal mass. This larger radius results in lower effective temperatures (3000 K versus 10^4 K)and hence far fewer ionizing photons ($\sim 10^{29}$ s^{-1} versus 10^{43} s^{-1} for a $2M_\odot$ protostar). Only after they become massive stars ($> 10M_\odot$) or reach the main sequence, do the differences between the models disappear.

During the formation of a radiative barrier and an outer shell of burning deuterium in the star, the radius increases by a factor of ~ 2 in size. The effect of this transition on the ionizing flux is so great that an ultracompact HII region forming around the star may promptly collapse as a result of the dramatically reduced flux of UV photons. In our study of a single star accreting at $10^{-3}M_\odot$/yr, the forming HII region collapsed from $300M_\odot$ to $50M_\odot$. Higher resolution studies of this collapse and HII region reformation are planned as the collapsed region is covered by only ~ 4 grid cells. Our results show that changes to the HII region around an isolated star can signal important structural transitions in the star itself.

Our results also showed that protostellar modeling has the greatest effect on star clusters during the earliest phases of star formation, when the only stars are low-mass pre-main-sequence stars. Major heating and ionization of the gas was delayed in the protostellar simulation by 1% and 3% of a freefall time, respectively. Once the protostars grow to be massive $10 - 20 M_{\odot}$ stars, the differences between a protostellar model and ZAMS model disappear, except that our cluster simulations showed the formation of more lower-mass stars ($< 10 M_{\odot}$) in the protostellar simulation. We saw 4 such stars (half the stars in the simulation) in the protostellar simulation, and none in the ZAMS simulation, where all five stars had masses greater than $10 M_{\odot}$.

Numerically, the use of the model had some other clear advantages. Through the efficient use of precomputed tables of values, the protostellar evolution model adds very little computational overhead to the FLASH code. In fact, it actually sped up our simulations by making the stars much less radiant during most of their early lifetimes, lightening the load on the codes required to compute heating, cooling, ionization, and raytracing. The cluster simulations ran an estimated 5% faster as a result.

Future simulations of star formation in turbulent clouds will show more clearly the global effects of radiative feedback when coupled to an accurate protostellar model. The use of one-zone models may also be helpful in finding descriptions of the integrated luminosity over time for entire star clusters—a necessary tool if the impact of radiative feedback on galactic or GMC scales is to be assessed.

We have shown prestellar modeling to be an important feature of accurate star formation simulations: they key effect was causing more low-mass stars to form, thereby shifting the initial mass function. It also delayed the onset of major heating and ionization by 5.9 kyr and 17.7 kyr respectively, and demonstrated that HII regions can collapse due to stellar structural transitions, while also adding to the efficiency of our simualations. It also opens up new research problems for future study: by considering the integrated luminosity from entire clusters, we can study the radiative feedback of clusters within GMCs and galaxies; we can study the impact of low-mass stars within turbulent, filamentary clouds; and we can prepare synthetic radio maps of isolated or clustered star formation and to compare with future ALMA observations.

Bibliography

Agertz, O., Moore, B., Stadel, J., Potter, D., Miniati, F., Read, J., Mayer, L., Gawryszczak, A., Kravtsov, A., Nordlund, Å., Pearce, F., Quilis, V., Rudd, D., Springel, V., Stone, J., Tasker, E., Teyssier, R., Wadsley, J., & Walder, R. 2007, MNRAS, 380, 963

Anderson, L. D., Zavagno, A., Rodón, J. A., Russeil, D., Abergel, A., Ade, P., André, P., Arab, H., Baluteau, J.-P., Bernard, J.-P., Blagrave, K., Bontemps, S., Boulanger, F., Cohen, M., Compiègne, M., Cox, P., Dartois, E., Davis, G., Emery, R., Fulton, T., Gry, C., Habart, E., Huang, M., Joblin, C., Jones, S. C., Kirk, J. M., Lagache, G., Lim, T., Madden, S., Makiwa, G., Martin, P., Miville-Deschênes, M.-A., Molinari, S., Moseley, H., Motte, F., Naylor, D. A., Okumura, K., Pinheiro Gonçalves, D., Polehampton, E., Saraceno, P., Sauvage, M., Sidher, S., Spencer, L., Swinyard, B., Ward-Thompson, D., & White, G. J. 2010, A&A, 518, L99+

Arzoumanian, D., André, P., Didelon, P., Könyves, V., Schneider, N., Men'shchikov, A., Sousbie, T., Zavagno, A., Bontemps, S., di Francesco, J., Griffin, M., Hennemann, M., Hill, T., Kirk, J., Martin, P., Minier, V., Molinari, S., Motte, F., Peretto, N., Pezzuto, S., Spinoglio, L., Ward-Thompson, D., White, G., & Wilson, C. D. 2011, A&A, 529, L6+

Bally, J. & Scoville, N. Z. 1980, ApJ, 239, 121

Banerjee, R. & Pudritz, R. E. 2006, ApJ, 641, 949

—. 2007, ApJ, 660, 479

Banerjee, R., Pudritz, R. E., & Holmes, L. 2004, MNRAS, 355, 248

Banerjee, R., Vázquez-Semadeni, E., Hennebelle, P., & Klessen, R. S. 2009, MNRAS, 398, 1082

Baraffe, I., Chabrier, G., Allard, F., & Hauschildt, P. H. 1998, A&A, 337, 403

Bate, M. R. 2009, MNRAS, 392, 1363

Bate, M. R., Bonnell, I. A., & Price, N. M. 1995, MNRAS, 277, 362

Berger, M. J. & Colella, P. 1989, Journal of Computational Physics, 82, 64

Beuther, H., Churchwell, E. B., McKee, C. F., & Tan, J. C. 2007, Protostars and Planets V, 165

Blitz, L. 1993, in Protostars and Planets III, ed. E. H. Levy & J. I. Lunine, 125–161

Calder, A. C., Fryxell, B., Plewa, T., Rosner, R., Dursi, L. J., Weirs, V. G., Dupont, T., Robey, H. F., Kane, J. O., Remington, B. A., Drake, R. P., Dimonte, G., Zingale, M., Timmes, F. X., Olson, K., Ricker, P., MacNeice, P., & Tufo, H. M. 2002, ApJS, 143, 201

Chabrier, G. 2003, PASP, 115, 763

Chandrasekhar, S. 1939, An introduction to the study of stellar structure, ed. Chandrasekhar, S.

Clarke, C. J., Bonnell, I. A., & Hillenbrand, L. A. 2000, Protostars and Planets IV, 151

Commerçon, B., Hennebelle, P., Audit, E., Chabrier, G., & Teyssier, R. 2010, A&A, 510, L3+

Cox, D. P. 1970, PhD thesis, University of California, San Diego.

Dalgarno, A. & McCray, R. A. 1972, ARA&A, 10, 375

D'Antona, F. & Mazzitelli, I. 1997, Mem. Soc. Astron. Italiana, 68, 807

D'Antona, F. & Mazzitelli, I. 1998, in Astronomical Society of the Pacific Conference Series, Vol. 134, Brown Dwarfs and Extrasolar Planets, ed. R. Rebolo, E. L. Martin, & M. R. Zapatero Osorio, 442–+

Deharveng, L., Schuller, F., Anderson, L. D., Zavagno, A., Wyrowski, F., Menten, K. M., Bronfman, L., Testi, L., Walmsley, C. M., & Wienen, M. 2010, A&A, 523, A6+

Dimonte, G., Youngs, D. L., Dimits, A., Weber, S., Marinak, M., Wunsch, S., Garasi, C., Robinson, A., Andrews, M. J., Ramaprabhu, P., Calder, A. C., Fryxell, B., Biello, J., Dursi, L., MacNeice, P., Olson, K., Ricker, P., Rosner, R., Timmes, F., Tufo, H., Young, Y.-N., & Zingale, M. 2004, Physics of Fluids, 16, 1668

Dubey, A., Fisher, R., Graziani, C., Jordan, IV, G. C., Lamb, D. Q., Reid, L. B., Rich, P., Sheeler, D., Townsley, D., & Weide, K. 2008, in Astronomical Society of the Pacific Conference Series, Vol. 385, Numerical Modeling of Space Plasma Flows, ed. N. V. Pogorelov, E. Audit, & G. P. Zank, 145–+

Duffin, D. F. & Pudritz, R. E. 2008, MNRAS, 391, 1659

Eggleton, P. P. 1971, MNRAS, 151, 351

—. 1972, MNRAS, 156, 361

—. 1973, MNRAS, 163, 279

Eggleton, P. P., Tout, C. A., & Fitchett, M. J. 1989, ApJ, 347, 998

Evans, II, N. J. 1999, ARA&A, 37, 311

Federrath, C., Banerjee, R., Clark, P. C., & Klessen, R. S. 2010, ApJ, 713, 269

Federrath, C., Banerjee, R., Seifried, D., Clark, P. C., & Klessen, R. S. 2011, in IAU Symposium, Vol. 270, IAU Symposium, ed. J. Alves, B. G. Elmegreen, J. M. Girart, & V. Trimble, 425–428

Fiege, J. D. & Pudritz, R. E. 2000, MNRAS, 311, 85

Franco-Hernández, R. & Rodríguez, L. F. 2004, ApJ, 604, L105

Frank, A. & Mellema, G. 1994, A&A, 289, 937

Fryxell, B., Olson, K., Ricker, P., Timmes, F. X., Zingale, M., Lamb, D. Q., MacNeice, P., Rosner, R., Truran, J. W., & Tufo, H. 2000, ApJS, 131, 273

Galván-Madrid, R., Peters, T., Keto, E. R., Mac Low, M.-M., Banerjee, R., & Klessen, R. S. 2011, MNRAS, 1081

Galván-Madrid, R., Rodríguez, L. F., Ho, P. T. P., & Keto, E. 2008, ApJ, 674, L33

Gaspari, M., Brighenti, F., D'Ercole, A., & Melioli, C. 2011, MNRAS, 415, 1549

Girichidis, P., Federrath, C., Banerjee, R., & Klessen, R. S. 2011, MNRAS, 413, 2741

Goldsmith, P. F., Heyer, M., Narayanan, G., Snell, R., Li, D., & Brunt, C. 2008, ApJ, 680, 428

Harper-Clark, E. & Murray, N. 2011, in Bulletin of the American Astronomical Society, Vol. 43, American Astronomical Society Meeting Abstracts #217, 216.03–+

Hayashi, C. 1961, PASJ, 13, 450

—. 1966, ARA&A, 4, 171

Heiles, C., Goodman, A. A., McKee, C. F., & Zweibel, E. G. 1993, in Protostars and Planets III, ed. E. H. Levy & J. I. Lunine, 279–326

Heitmann, K., Ricker, P. M., Warren, M. S., & Habib, S. 2005, ApJS, 160, 28

Hill, T., Motte, F., Didelon, P., Bontemps, S., Minier, V., Hennemann, M., Schneider, N., Andre, P., Men'shchikov, A., Anderson, L. D., Arzoumanian, D., Bernard, J.-P., di Francesco, J., Elia, D., Giannini, T., Griffin, M. J., Kirk, J., Konyves, V., Marston, A. P., Martin, P., Molinari, S., Nguyen Luong, Q., Peretto, N., Pezzuto, S., Roussel, H., Sauvage, M., Sousbie, T., Testi, L., Ward-Thompson, D., White, G. J., Wilson, C. D., & Zavagno, A. 2011, ArXiv e-prints: 1108.0941

Hillenbrand, L. A., Bauermeister, A., & White, R. J. 2008, in Astronomical Society of the Pacific Conference Series, Vol. 384, 14th Cambridge Workshop on Cool Stars, Stellar Systems, and the Sun, ed. G. van Belle, 200–+

Hoare, M. G., Kurtz, S. E., Lizano, S., Keto, E., & Hofner, P. 2007, Protostars and Planets V, 181

Horedt, G. P. 1986a, A&A, 160, 148

—. 1986b, Ap&SS, 126, 357

Hosokawa, T. & Omukai, K. 2009, ApJ, 691, 823

Iliev, I. T., Ciardi, B., Alvarez, M. A., Maselli, A., Ferrara, A., Gnedin, N. Y., Mellema, G., Nakamoto, T., Norman, M. L., Razoumov, A. O., Rijkhorst, E.-J., Ritzerveld, J., Shapiro, P. R., Susa, H., Umemura, M., & Whalen, D. J. 2006, MNRAS, 371, 1057

Keto, E. 2002, ApJ, 580, 980

—. 2003, ApJ, 599, 1196

—. 2007, ApJ, 666, 976

Kevlahan, N. & Pudritz, R. E. 2009, ApJ, 702, 39

Kitsionas, S., Federrath, C., Klessen, R. S., Schmidt, W., Price, D. J., Dursi, L. J., Gritschneder, M., Walch, S., Piontek, R., Kim, J., Jappsen, A.-K., Ciecielag, P., & Mac Low, M.-M. 2009, A&A, 508, 541

Kroupa, P. 2001, MNRAS, 322, 231

—. 2002, Science, 295, 82

Krumholz, M. R., Cunningham, A. J., Klein, R. I., & McKee, C. F. 2010, ApJ, 713, 1120

Krumholz, M. R., Klein, R. I., & McKee, C. F. 2007a, ApJ, 656, 959

Krumholz, M. R., Klein, R. I., McKee, C. F., & Bolstad, J. 2007b, ApJ, 667, 626

Krumholz, M. R., McKee, C. F., & Klein, R. I. 2004, ApJ, 611, 399

Kuiper, R., Klahr, H., Dullemond, C., Kley, W., & Henning, T. 2010, A&A, 511, A81+

Kurtz, S., Churchwell, E., & Wood, D. O. S. 1994, ApJS, 91, 659

Larson, R. B. 1969, MNRAS, 145, 271

Levermore, C. D. & Pomraning, G. C. 1981, ApJ, 248, 321

Lim, A. J. & Mellema, G. 2003, A&A, 405, 189

Mac Low, M.-M. & Klessen, R. S. 2004, Reviews of Modern Physics, 76, 125

Matthews, B. C., Fiege, J. D., & Moriarty-Schieven, G. 2002, ApJ, 569, 304

Matzner, C. D. 2002, ApJ, 566, 302

McKee, C. F. & Ostriker, E. C. 2007, ARA&A, 45, 565

McKee, C. F. & Tan, J. C. 2003, ApJ, 585, 850

McKee, C. F., Zweibel, E. G., Goodman, A. A., & Heiles, C. 1993, in Protostars and Planets III, ed. E. H. Levy & J. I. Lunine, 327–+

Mellema, G. & Lundqvist, P. 2002, A&A, 394, 901

Mezger, P. G. & Henderson, A. P. 1967, ApJ, 147, 471

Murray, N., Ménard, B., & Thompson, T. A. 2011, ApJ, 735, 66

Myers, P. C. 2009, ApJ, 700, 1609

Myers, P. C. & Goodman, A. A. 1988, ApJ, 326, L27

Nakano, T., Hasegawa, T., Morino, J.-I., & Yamashita, T. 2000, ApJ, 534, 976

Nakano, T., Hasegawa, T., & Norman, C. 1995, Ap&SS, 224, 523

Offner, S. S. R., Klein, R. I., McKee, C. F., & Krumholz, M. R. 2009, ApJ, 703, 131

Olson, K. M., MacNeice, P., Fryxell, B., Ricker, P., Timmes, F. X., & Zingale, M. 1999, in Bulletin of the American Astronomical Society, Vol. 31, American Astronomical Society Meeting Abstracts, 1430–+

Osterbrock, D. E. 1989, Astrophysics of gaseous nebulae and active galactic nuclei, ed. Osterbrock, D. E.

Padoan, P. & Nordlund, Å. 2002, ApJ, 576, 870

Palla, F. & Stahler, S. W. 1991, ApJ, 375, 288

—. 1992, ApJ, 392, 667

—. 1993, ApJ, 418, 414

Parigi, G. 1992, PhD thesis, University of Florence

Paxton, B. 2004, PASP, 116, 699

Peters, T., Banerjee, R., Klessen, R. S., Mac Low, M.-M., Galván-Madrid, R., & Keto, E. R. 2010a, ApJ, 711, 1017

Peters, T., Mac Low, M.-M., Banerjee, R., Klessen, R. S., & Dullemond, C. P. 2010b, ApJ, 719, 831

Pols, O. R., Tout, C. A., Eggleton, P. P., & Han, Z. 1995, MNRAS, 274, 964

Price, D. J. & Bate, M. R. 2009, MNRAS, 398, 33

Pudritz, R. 2004, in CfA Colloquium Lecture Series Talk

Pudritz, R. E., Ouyed, R., Fendt, C., & Brandenburg, A. 2007, Protostars and Planets V, 277

Richling, S. & Yorke, H. W. 2000, ApJ, 539, 258

Ricker, P. M., Calder, A. C., Dursi, L. J., Fryxell, B., Lamb, D. Q., MacNeice, P., Olson, K., Rosner, R., Timmes, F. X., Truran, J. W., Tufo, H. M., & Zingale, M. 2001, in American Institute of Physics Conference Series, Vol. 583, American Institute of Physics Conference Series, 316–318

Rijkhorst, E.-J., Plewa, T., Dubey, A., & Mellema, G. 2006, A&A, 452, 907

Rodríguez, L. F., Gómez, Y., & Tafoya, D. 2007, ApJ, 663, 1083

Shapiro, P. R., Iliev, I. T., & Raga, A. C. 2004, MNRAS, 348, 753

Spitzer, L. 1978, Physical processes in the interstellar medium, ed. Spitzer, L.

Tan, J. C. & McKee, C. F. 2004, ApJ, 603, 383

Tasker, E. J., Brunino, R., Mitchell, N. L., Michielsen, D., Hopton, S., Pearce, F. R., Bryan, G. L., & Theuns, T. 2008, MNRAS, 390, 1267

Testi, L., Sargent, A. I., Olmi, L., & Onello, J. S. 2000, ApJ, 540, L53

Tout, C. A., Pols, O. R., Eggleton, P. P., & Han, Z. 1996, MNRAS, 281, 257

Truelove, J. K., Klein, R. I., McKee, C. F., Holliman, II, J. H., Howell, L. H., & Greenough, J. A. 1997, ApJ, 489, L179+

Turner, N. J. & Stone, J. M. 2001, ApJS, 135, 95

Vázquez-Semadeni, E., Ryu, D., Passot, T., González, R. F., & Gazol, A. 2006, ApJ, 643, 245

Whalen, D. & Norman, M. L. 2008, ApJ, 673, 664

Whitehouse, S. C. & Bate, M. R. 2004, MNRAS, 353, 1078

Whitehouse, S. C., Bate, M. R., & Monaghan, J. J. 2005, MNRAS, 364, 1367

Williams, J. P., Blitz, L., & McKee, C. F. 2000, Protostars and Planets IV, 97

Wood, D. O. S. & Churchwell, E. 1989, ApJS, 69, 831

Yorke, H. W. & Sonnhalter, C. 2002, ApJ, 569, 846

Zanni, C., Ferrari, A., Rosner, R., Bodo, G., & Massaglia, S. 2007, A&A, 469, 811

Zinnecker, H. & Yorke, H. W. 2007, ARA&A, 45, 481